

**NASA CONTRACTOR  
REPORT**

**NASA CR-1958**



**NASA CR-1958**

0061316



**LOAN COPY: RETURN TO  
AFWL (DOUL)  
KIRTLAND AFB, N. M.**

**EXPERIMENTAL PLASMA STUDIES**

*by Michael G. Dunn*

*Prepared by*  
CORNELL AERONAUTICAL LABORATORY, INC.  
Buffalo, N.Y.  
*for Langley Research Center*

**NATIONAL AERONAUTICS AND SPACE ADMINISTRATION • WASHINGTON, D. C. • MARCH 1972**



0061316

1. Report No. NASA CR-1958	2. Government Accession No.	3. Recipient's Catalog No.	
4. Title and Subtitle EXPERIMENTAL PLASMA STUDIES		5. Report Date March 1972	6. Performing Organization Code
		8. Performing Organization Report No. Final Rept. NAS1-9627	
7. Author(s) Michael G. Dunn		10. Work Unit No.	11. Contract or Grant No. NAS1-9627
9. Performing Organization Name and Address Cornell Aeronautical Company Buffalo, New York		13. Type of Report and Period Covered Contractor Report	
		14. Sponsoring Agency Code	
12. Sponsoring Agency Name and Address National Aeronautics and Space Administration Washington, D.C. 20546		15. Supplementary Notes	
16. Abstract The rate coefficients for the reactions $C^+ + e^- + e^- \xrightarrow{k_{r1}} C + e^-$ and $CO^+ + e^- \xrightarrow{k_{r2}} C + O$ been measured over the electron temperature range of approximately 1500°K to 7000°K. The measurements were performed in CO that had expanded from equilibrium reservoir conditions of 7060°K at 17.3 atm pressure and from 6260°K at 10.0 atm pressure.  Two RAM flight probes were used to measure electron density and electron temperature in the expanding flow of a shock tunnel. Experiments were performed in the inviscid flow with both probes and in the nozzle-wall boundary layer with the constant bias-voltage probe. For free-molecular flow conditions the electron densities deduced using the data interpretation theory suggested by Smetana agree well with other independent measurements. When the wires were operated in a moderately transition-flow regime, the free-molecular flow theory underpredicted the electron densities by 20 to 40 percent. The distributions of electron density and electron temperature were independently measured using voltage-swept thin-wire probes. The agreement between the electron-density distributions obtained with these two probing techniques was found to be good.  Thin-wire Langmuir probes were also used to measure the electron-density and electron-temperature distributions in the boundary layer of a sharp flat plate located on the nozzle centerline. The test gas for these experiments was argon plus 0.12 percent nitrogen. The flow conditions were such that free-molecular flow theories could be used to infer ion densities. Electron temperatures measured in these boundary layers were found to be substantially greater than the calculated heavy-particle translational temperature at the boundary-layer edge and remained relatively constant through the boundary layer and along the plate.  Admittance measurements were performed with the RAM C and RAM C-C S-band antennas in the presence of an ionized boundary layer. The test gas was changed from argon plus 0.12 percent nitrogen to carbon monoxide in order to achieve greater electron-density levels. However, the CO boundary layer was not probed with thin-wire probes so the electron-temperature and electron-density distributions are not well known at the present time. Voltage reflection coefficients and phase rotations were obtained for a range of $n_e/n_{e,cr}$ from approximately 0.2 to 3.0. The influence of boundary-layer thickness on the reflection coefficient was found to be significant.			
17. Key Words (Suggested by Author(s)) Antennas in Plasma, Martian Reentry Measurement of Rate Coefficients, Langmuir Probe Calibrations		18. Distribution Statement  Unclassified - Unlimited	
19. Security Classif. (of this report) Unclassified	20. Security Classif. (of this page) Unclassified	21. No. of Pages 98	22. Price* \$3.00

\*For sale by the National Technical Information Service, Springfield, Virginia 22151

1. Electrostatic probes  
 2. Plasma devices  
 3. Reaction kinetics  
 20 Mar 72



## TABLE OF CONTENTS

<u>Section</u>		<u>Page</u>
1	INTRODUCTION . . . . .	1
2	MEASUREMENT OF $C^+ + e^- + e^-$ THREE-BODY RECOMBINATION AND $CO^+ + e^-$ DISSOCIATIVE RECOMBINATION IN EXPANDING CARBON MONOXIDE FLOWS . . . . .	2
	2.1 Experimental Apparatus and Technique . . . . .	4
	2.2 Method of Determining Rate Coefficient . . . . .	4
	2.3 Procedure for Calculating Electron-Density Distribution and Chemical Model Utilized . . . . .	5
	2.4 Langmuir-Probe and Microwave- Interferometer Measurements . . . . .	6
	2.5 Determination of Rate Coefficient . . . . .	7
	2.5.1 $C^+ + e^- + e^- \rightarrow C + e^-$ Reaction in Expansion from 7060°K at 17.3 atm Pressure . . . . .	7
	2.5.2 $CO^+ + e^- \rightarrow C + O$ Reaction in Expansion from 6260°K at 10.0 atm Pressure . . . . .	8
	2.6 Conclusions . . . . .	10
3	LABORATORY MEASUREMENTS OF ELECTRON DENSITY AND ELECTRON TEMPERATURE WITH RAM FLIGHT PROBES . . . . .	10
	3.1 Experimental Apparatus and Technique . . . . .	11
	3.2 Discussion of Constant Bias-Voltage Probe Results in Inviscid Flow . . . . .	12
	3.3 Discussion of Constant Bias-Voltage Probe Results in Boundary-Layer Flow . . . . .	15
	3.4 Discussion of RAM C-C Swept-Voltage Probe Data in Inviscid Flow . . . . .	16
	3.5 Concluding Remarks . . . . .	16
4	ANTENNA ADMITTANCE MEASUREMENTS IN THE PRESENCE OF IONIZED BOUNDARY LAYERS . . . . .	17
	4.1 Electron-Density Distributions in Boundary Layer over Flat-Plate Model . . . . .	18

<u>Section</u>	<u>Page</u>
4.2 Admittance Measurements with RAM Antennas . . . . .	20
4.2.1 RAM C S-Band Antenna Measurements . . .	21
4.2.2 RAM C-C S-Band Antenna Measurements . .	22
4.3 Conclusions . . . . .	23
REFERENCES . . . . .	24

# EXPERIMENTAL PLASMA STUDIES

By Michael G. Dunn  
Cornell Aeronautical Laboratory, Inc.  
Buffalo, New York

## 1. INTRODUCTION

This document is the final report for Contract NAS 1-9627 which was initiated in November 1969. Several areas of experimental research were pursued as part of this study. All of the experiments were conducted in the expanding-flow environment of a reflected-shock tunnel. The first area of interest was the measurement of the reaction rate coefficient for the reactions  $C^+ + e^- + e^- \rightarrow C + e^-$  and  $CO^+ + e^- \rightarrow C + O$ . The results of these experiments are applicable over an electron temperature range of approximately 1500 to 7000°K which is consistent with that currently expected in the stagnation region during entry of a vehicle into the atmospheres of Mars or Venus.

The second area of research was concerned with the operation, under controlled laboratory conditions, of the wedge-shaped electrostatic probes that were used onboard the RAM flight vehicles. The probes used in these studies were the RAM C-1 constant bias-voltage probe and the RAM C-C voltage-swept thin-wire probes. These probes were used in inviscid and boundary-layer flows for conditions such that independent measurements of the electron density (and electron temperature in the case of the RAM C-C probe) could be obtained using microwave interferometers and/or voltage-swept thin-wire probes.

The third area of interest was concerned with the measurement of electron-density distributions and antenna-admittance properties in ionized boundary layers over a flat plate. Measurements were performed with two S-band and one X-band antennas using four-probe reflectometers. Thin-wire Langmuir probes operating in the free-molecular flow regime were used to measure the electron-density distribution in the boundary layer over the antennas and microwave interferometers were used to measure the electron density of the free stream at 1 inch and 11 inches upstream of the plate leading edge.

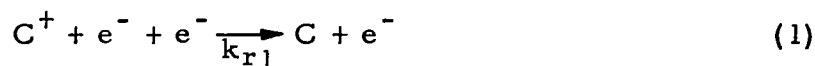
In the remainder of this report, the results obtained in each of the areas noted above will be discussed separately. The results of the reaction rate coefficient studies are described in Section 2. In Section 3 the electrostatic-probe measurements performed with the RAM C and RAM C-C probes are discussed. The technical discussion is concluded in Section 4 with a description of the antenna admittance measurements obtained in the presence of ionized boundary layers.

The author would like to thank Mr. Richard Blum of CAL for constructing and operating the microwave reflectometers during the course of the antenna admittance measurements.

## 2. MEASUREMENT OF $C^+ + e^- + e^-$ THREE-BODY RECOMBINATION AND $CO^+ + e^-$ DISSOCIATIVE RECOMBINATION IN EXPANDING CARBON MONOXIDE FLOWS

The next step in space exploration beyond the moon project is most likely the exploration of the planets Mars and Venus. One of the basic objectives of the first missions will probably be the determination of the composition of the atmosphere, not only near the surface, but throughout the entry trajectory. The success of these missions is partially dependent upon the ability to calculate the gas composition in the plasma surrounding the entry body. At the present time, reaction rate coefficients for several of the reactions of possible importance in the C-O-N system are not well known. This lack of data motivated the studies described here. At the present time attention is confined to reactions involving ions and/or electrons because of the potential communication blackout problem.

Previous measurements reported<sup>1-3\*</sup> from this laboratory have presented rate coefficient data for the dissociative recombination of  $NO^+$ ,  $N_2^+$ , and  $O_2^+$  which are also of importance in the C-O-N system. The purpose of this report is to present rate-coefficient data, obtained in the same manner, for the electron depletion reactions



and



Knowledge of the electron temperature is essential for determining  $k_r$  for both of these reactions. The electron temperature was therefore measured and used in the data correlation.

Many authors<sup>4-15</sup> have published theoretical predictions of the rate coefficient for the class of reactions given by  $M^+ + e^- + e^- \rightarrow M + e^-$  where M is an atomic ion. The result of Makin and Keck<sup>4</sup> is used here for comparison purposes because of its simplicity and good agreement with available experimental data. The authors use a classical phase-space concept in which a point in phase space is used to represent the impact point of the three colliding particles and a distribution of these points is assumed to correspond to a gas in thermodynamic equilibrium. The authors propose a "trial" surface which separates the free and bound states of the electron-

---

\* Superscripts refer to references given at end of text.

ion pair at a selected energy which is less than the dissociation limit. By minimizing the rate at which representative points cross the "trial" surface, a least upper bound to the recombination rate can be calculated.

Bates, Kingston and McWhirter,<sup>5</sup> in 1962, studied collisional-radiative recombination between electrons and atomic ions in dense plasmas. The authors propose a statistical theory which permits the calculation of the rate coefficient if one knows the relevant spontaneous transition probabilities. The theory has been applied to the calculation of the reaction rate coefficients for a hydrogen-ion plasma. Application to other ions would probably be difficult to justify in light of uncertainties associated with current transition probability information.

Recently, D'Angelo<sup>6</sup> suggested that the classical three-body recombination theory of Thomson<sup>7</sup> can be successfully applied to the calculation of electron-electron-ion collisional-radiative recombination. His results are in good agreement with the results of both Bates, Kingston and McWhirter<sup>5</sup> and Hinnov and Hirschberg.<sup>8</sup>

Hinnov and Hirschberg<sup>8</sup> present a theoretical treatment of the calculation of the electron-electron-ion collisional-radiative rate coefficient and, in the same paper, substantiate the theory with experimental data which they have obtained for the three-body recombination of  $\text{He}^+$  and  $\text{H}^+$ . Their theoretical approach involves recombination into the higher energy states,  $n > 5$ , and thus some knowledge of collisional transition probabilities is required. However, by application of a number of simplifying assumptions, they are able to approximate the rate coefficient without a detailed knowledge of the collisional transition probabilities. In addition, the experimental results of Motley and Kuckes,<sup>9</sup> for the recombination of  $\text{He}^+$ , are compared by Hinnov and Hirschberg to their own theory and data over the temperature range 1300°K to 3000°K. Their theoretical results are also in good agreement with the previously discussed works of Refs. 4 and 5. The experimentally determined rate coefficients were deduced on the basis of microwave (electron-density decay) and spectrum line-intensity (electron temperature) measurements obtained in the afterglow of magnetically confined plasmas of helium and hydrogen.

The only measurement for the three-body recombination relevant to the C-O-N system is that obtained by Park<sup>16</sup> at an electron temperature of 10,000°K for the reaction  $\text{N}^+ + e^- + e^- \rightarrow \text{N} + e^-$ . His experiments were performed in the expanding-flow region of an electric-arc plasma wind tunnel. He used the hydrogen-beta line-broadening technique to determine the electron density. The electron temperature was obtained from the ratio of spectral lines of nitrogen, 5617 Å and 4935 Å. Park<sup>17</sup> also discusses a theoretical technique for calculating the recombination rate coefficients for the deionization of atomic ions. He compares the results of his calculations for  $\text{N}^+$  to those of Hinnov and Hirschberg ( $\text{He}^+$ ) and illustrates good agreement.

Experimental data for the reaction  $\text{CO}^+ + \text{e}^- \rightarrow \text{C} + \text{O}$  have been reported by Mentzoni and Donohoe for electron temperatures of approximately  $273^\circ\text{K}$ <sup>18</sup> and  $775^\circ\text{K}$ .<sup>19</sup> The authors used microwave diagnostics to study the electron decay in the afterglow following a pulsed d.c. discharge in carbon monoxide.

In the present experiments, both the electron temperature and number density were measured. This electron temperature was used in computing the variation of number density along the nozzle. The recombination rate coefficient was then adjusted until the calculated number density agreed with the microwave-interferometer data.

## 2.1 Experimental Apparatus and Technique

A pressure-driven shock tube was used to produce a reservoir of high-temperature carbon monoxide which was subsequently expanded in a conical nozzle as shown in Fig. 1. The test gas used in these experiments was supplied by Lif-O-Gen, Inc. A chemical analysis of the gas indicated the following:  $25 \pm 5$  ppm of nitrogen, argon less than 2 ppm, carbon dioxide less than 10 ppm, helium less than 4 ppm, hydrogen less than 4 ppm, methane less than 2 ppm, oxygen less than 2 ppm, and water less than 1 ppm.

The electron number densities were measured at 11.5, 21.5, 31.5 and 41.5 inches from the nozzle throat using microwave interferometers operating at frequencies of either 35 or 17 GHz. One inch downstream of each microwave-interferometer measuring station, thin-wire Langmuir probes were used on the nozzle centerline to measure the electron temperature and electron density. The microwave interferometers and the experimental procedure are discussed in more detail in Ref. 1.

The probes used in these experiments were constructed by surrounding 0.004-inch-diameter tungsten wires with a quartz envelope, leaving a nominal 0.400-inch length of bare wire exposed. Immediately prior to each run, the tungsten oxide is removed by placing the probe in a dilute solution of sodium hydroxide and passing approximately  $400 \mu$  amps of current through the circuit for approximately 10 minutes.

## 2.2 Method of Determining Rate Coefficient

Two reflected-shock reservoir conditions were used to obtain the reaction rate coefficients for the deionization reactions given by Eqs. (1) and (2). At the first condition the test gas was expanded from an equilibrium condition of  $7060^\circ\text{K}$  and 17.3 atm pressure and the dominant chemical reaction taking place in the expansion was  $\text{C}^+ + \text{e}^- + \text{e}^- \rightarrow \text{C} + \text{e}^-$ . All of the other reactions given in Table 1 were included in the nonequilibrium nozzle-flow calculations performed for this reservoir condition, but perturbation of their rate coefficients did not have a significant influence on the predicted electron-density distribution. At the second condition,  $6260^\circ\text{K}$  and 10.0 atm pressure, the reactions involving neutral species only were still

unimportant, but several reactions involving charged species were important. By accepting a set of rate coefficients for the charge-transfer reactions it was possible to deduce the rate coefficient for the dissociative recombination reaction  $\text{CO}^+ + \text{e}^- \rightarrow \text{C} + \text{O}$ . In the remainder of the paper, the method of data analysis is described and experimental results are presented for each of the previously mentioned conditions.

### 2.3 Procedure for Calculating Electron-Density Distribution and Chemical Model Utilized

The nonequilibrium nozzle-flow calculations noted above were performed with the nozzle-flow computer program described in Ref. 20. This program computes the solution for the gasdynamic properties and chemical composition in the expansion of an arbitrary gas mixture from an equilibrium reservoir state through a given nozzle geometry. The vibrational and electronic degrees of freedom of the species are assumed to maintain thermodynamic equilibrium but the chemical reactions are allowed to proceed at finite rates. A more detailed description of the modifications made to the standard version of this program in order to perform the calculations discussed here is given in Ref. 2. In this study the following species were included:  $\text{CO}$ ,  $\text{O}_2$ ,  $\text{CO}_2$ ,  $\text{C}$ ,  $\text{O}$ ,  $\text{CO}^+$ ,  $\text{O}_2^+$ ,  $\text{C}^+$ ,  $\text{O}^+$  and  $\text{e}^-$ . The chemical-kinetics model used in the earlier calculations was significantly larger than the one shown in Table 1, which was obtained by eliminating from the initial model the unimportant reactions.

Reaction rate coefficients for reactions 1-6 were estimated to be represented by the expressions given in Table 1. For the expanding flow situation of interest here, more accurate knowledge of these rate coefficients is not necessary because the neutral species concentrations in the expansion were essentially frozen at the nozzle throat (near equilibrium) values and thus the neutral reactions had little influence on the ion concentrations in the expansion. Much more important for these studies was the rate coefficients for the ion-molecule and ion-atom reactions 7-10. Throughout the expansion these reactions were all proceeding in the direction opposite to that written in Table 1. The only available experimental data for these reactions were those obtained by Fehsenfeld, Schmeltekopf and Ferguson<sup>21</sup> at 300°K for the reaction  $\text{CO}_2 + \text{C}^+ \rightarrow \text{CO} + \text{CO}^+$ . To the author's knowledge, rate coefficients have not been measured for the remaining three reactions. These rates were therefore estimated at 300°K and extrapolated to higher temperatures as described by the equations given in Table 1. Compared to reactions 7-10, reaction 11 was considerably less important.

In all of the nozzle-flow calculations performed in this study, the prescribed nozzle cross-sectional area was that of the inviscid core. The boundary-layer displacement thickness was computed using the method of Burke and Bird.<sup>22</sup> For the conditions of these experiments the boundary-layer correction is small.

## 2.4 Langmuir-Probe and Microwave-Interferometer Measurements

A typical swept-voltage probe characteristic obtained on the nozzle centerline for a reservoir condition of 7060°K and 17.3 atm is shown in Figs. 2(a) and (b). These oscilloscope records were recorded simultaneously using two oscilloscopes with the vertical sensitivities adjusted to emphasize the electron-retarding region, from which the electron temperature was deduced, and the ion-current region, from which the electron density was obtained. The voltage applied to the probe was recorded on the lower channel of each oscilloscope. In these experiments the probe voltage was swept from -5 to +2 volts relative to ground potential. Figure 2(c) shows the phase-shift of the incident energy and the voltage sweep relative to the test time obtained from a microwave interferometer located one inch upstream of the Langmuir probe. The attenuation of the incident microwave energy was also recorded but was found to be less than 2 db for this location in the expansion.

The electron density was obtained from the Langmuir-probe data using the free-molecular flow theory of Laframboise.<sup>23</sup> In these calculations, the dominant ion was assumed to be  $C^+$  consistent with the calculated species concentrations presented in Figs. 3(a) and (b) for the two reservoir conditions. However, in contrast to previous<sup>1-3</sup> results obtained at this laboratory using several different test gases (air, nitrogen, oxygen and argon), the electron densities obtained in these experiments from the Langmuir-probe data were consistently less than the corresponding values obtained from the microwave interferometers by a factor of 1.4 to 2.0 at the downstream stations.

The cause of this apparent inconsistency between the two diagnostic techniques does not appear to be related to collisional effects which have been shown by Talbot and Chou<sup>24</sup> to produce such a result. The relative magnitudes of the mean free paths  $\lambda_{i-n}$ ,  $\lambda_{m-n}$ ,  $\lambda_{e-n}$ ,  $\lambda_{i-i}$ , and  $\lambda_{e-e}$  were calculated using the expressions summarized by Sonin<sup>25</sup> and are presented in Fig. 4 for one of the experimental conditions. With the exception of  $\lambda_{i-i}$ , which is somewhat smaller at this experimental condition, these values are not significantly different from those obtained for the previous nitrogen work of Dunn and Lordi<sup>26</sup> in which the probe and microwave-interferometer results were found to be in good agreement at the downstream stations. Initially it was felt that the smaller value of the ion-ion mean free path was contributing to the disagreement. The second experimental condition was then completed and a quantitatively similar inconsistency between the probe and microwave-interferometer results was still present. However, for this experimental condition, all of the mean free paths were comparable to those for the previous nitrogen work.

The calculated ion-species distributions suggest that the correct ion has been used in the probe data reduction and the calculated mean free paths suggest that the probe results should be free of collisional effects. It is realized that if the collected ion were  $CO^+$  instead of  $C^+$ , then the probe and interferometer results would be in relatively good agreement. However, in order for this to be the case, the mobility of the  $CO^+$  ion would

necessarily be much larger (see Figs. 3(a) and (b) for relative concentrations) than that of  $C^+$  and in light of existing information this is an unlikely result.

The anomaly described above is disturbing because the only check one has on proper probe operation is by comparison of the electron-density results with an accepted measurement standard, in our case the microwave interferometer. However, because the probe-deduced electron densities are not essential to the rate-coefficient determination, the problem was not pursued further. The electron temperatures obtained from the probe results are, however, used for the rate-coefficient studies. The measured electron temperatures have been accepted as correct on the basis of past experience<sup>1-3,26</sup> with Langmuir-probe operation. Later in the text, the influence of the electron temperature on the rate coefficient results will be illustrated.

## 2.5 Determination of Rate Coefficient

It was previously mentioned that the rate coefficient for the deionization of  $C^+$  by the reaction  $C^+ + e^- + e^- \rightarrow C + e^-$  and the deionization of  $CO^+$  by the reaction  $CO^+ + e^- \rightarrow C + O$  have been measured at two separate reservoir conditions. In this section the measurements obtained at each of the experimental conditions are discussed separately.

2.5.1  $C^+ + e^- + e^- \rightarrow C + e^-$  reaction in expansion from 7060°K at 17.3 atm pressure. - The electron-temperature measurements performed at this experimental condition are compared in Fig. 5 to the calculated heavy-particle translational temperature. Measurements were made at axial distances from the nozzle throat of 12.5, 22.5, 32.5 and 42.5 inches ( $A/A^* = 70, 230, 470$  and  $780$ ). The electron temperature appears to decrease slightly with increasing expansion ratios. At the first three measuring stations, the electron temperatures are seen to scatter approximately  $\pm 10\%$  about an average value. At the last measuring station the scatter is somewhat greater. The dashed line faired through the measurements represents the electron temperature used in the rate-coefficient determination.

The electron-density measurements performed in the expansion are shown on Fig. 6. The measurements are seen to scatter by approximately  $\pm 15\%$  about an average value. Much of this scatter can be correlated with the run-to-run variation in the shock-tube incident-shock velocity.

It was previously noted that for these experiments the neutral-chemistry reactions were relatively unimportant. All of the charged-chemistry reactions given in Table 1 were included in the calculations but the only one of importance was reaction 13. In correlating the experimental data we have adopted the  $T_e^{-4.5}$  temperature dependence of Makin and Keck<sup>4</sup> for this reaction and the  $T_e^{-1.5}$  temperature dependence<sup>1-3</sup> for reaction 12. We do not feel that our results are sufficiently sensitive to temperature dependence to merit any change from these predicted temperature variations.

In order to demonstrate the dominance of reaction 13, the rate coefficient for each of the reactions 12, 7, 9 and 10 was individually decreased or increased by a factor of 10 and the nonequilibrium-flow calculation repeated. For none of these rate coefficient perturbations did the predicted electron density change by more than 15%. It can therefore be concluded that the rate coefficients for these reactions given in Table 1 can be considerably in error without affecting the rate coefficient obtained from these experiments for the reaction  $C^+ + e^- + e^- \rightarrow C + e^-$ . By contrast, the influence of the rate coefficient for reaction 13 on the predicted electron-density distribution is shown on Fig. 6. Line A on this figure represents the predicted result using the theoretical rate coefficient of Ref. 4 and is seen to slightly overpredict the measured results. By increasing their predicted rate coefficient by a factor of 3.5 (line D) or less (lines B and C) all of the experimental data can be correlated. A rate coefficient of  $(2.2 \pm 0.7) \times 10^{40} T_e^{-4.5}$  correlates the experimental data reasonably well.

Line E on Fig. 6 illustrates that the electron temperature has an important influence on the predicted electron-density distribution for this reservoir condition. This result was obtained using the same rate coefficients as used for line D but the heavy-particle translational temperature was used instead of the electron temperature in the rate coefficient expression. The effect of the temperature history is seen to be a reduction in the predicted electron density at  $A/A^* = 1000$  of about 1.6. At smaller area ratios, the importance of the temperature history can be seen to be reduced.

Figure 7 presents a comparison between the data of this paper and previous reaction rate coefficient data and predictions for the class of reactions given by  $M^+ + e^- + e^- \rightarrow M + e^-$ . To the author's knowledge, there are no other data for the  $C^+ + e^- + e^- \rightarrow C + e^-$  reaction with which the present results could be compared. As can be seen from Fig. 7 the prediction of Makin and Keck,<sup>4</sup> which is independent of the ion undergoing recombination, appears to be a good approximation to the available experimental data.

2.5.2  $CO^+ + e^- \rightarrow C + O$  reaction in expansion from 6260°K at 10.0 atm pressure. - Microwave-interferometer and Langmuir-probe measurements were also performed at the same axial locations as previously described for a reservoir condition of 6260°K at 10.0 atm pressure. The boundary-layer growth for this condition was somewhat different than calculated for the previous condition which accounts for why the results are plotted at different area ratios for the same axial location.

The measured electron-temperature distribution in the expansion is presented in Fig. 8 along with the calculated heavy-particle translational temperature. The electron temperature is shown to decrease slightly in the region from 12.5 to 22.5 inches but to remain relatively uniform beyond 22.5 inches from the throat. The scatter in these measurements is somewhat larger than previously experienced but consistent with that obtained at 42.5 inches for the previous experimental condition (see Fig. 5). The dashed line faired through the data was used in determining the reaction rate coefficient.

The measured electron densities are presented in Fig. 9 as a function of inviscid area ratio. The scatter in these measurements is consistent with that experienced at the previous experimental condition. However, the results obtained at the last station appear to be high by about 15% based upon extrapolation of the three upstream results. The reason for this is not known but it is possibly due to an inaccuracy in the boundary-layer correction at this downstream location.

Again the neutral-species reactions were unimportant in the expansion. However, for this reservoir condition, reactions 7, 8, 9, 10 and 12 were dominant (all proceeding in the opposite direction to that written in Table 1) and of approximately equal importance. The three-body reactions 13 and 14 were relatively unimportant even though the dominant ion in the expansion was  $C^+$  (see Fig. 3(b)). The calculations have demonstrated that the reactions controlling the  $C^+$  concentration level are the reactions 7-10 and 12.

The fact that the ion-molecule and ion-atom charge-transfer reactions have a significant influence on the predicted electron-density distributions is unfortunate for the purposes of this study in light of the previously noted uncertainty in the associated reaction rate coefficients. At the present time it seems reasonable to accept the rate coefficients given in Table 1 for these reactions and proceed with the data reduction. It is, however, important to realize that the results may have to be modified if data for these reactions were to become available.

Lines A, B, and C on Fig. 9 illustrate the influence of the  $CO^+ + e^-$  rate coefficient on the calculated electron-density distribution, accepting the rates given in Table 1 for reactions 7-11. The temperature dependence of this reaction was assumed to be  $T_e^{-1.5}$  on the basis of previous work by Hansen,<sup>27</sup> O'Malley,<sup>28</sup> and Cunningham and Hobson.<sup>29</sup> The calculations were performed using the measured electron-temperature distribution. With the exception of the most downstream data, the electron-density measurements are well correlated by a rate coefficient given by  $k_{R2} = (1.5 \pm 0.3) \times 10^{22} T_e^{-1.5}$ . The influence of using the electron temperature instead of the heavy-particle translational temperature in performing the calculations is insignificant as can be seen by comparing lines C and D.

Comparison of line E with line C shows the influence of the ion-atom rate coefficient on the predicted electron-density distribution. For this particular calculation, the rate of reaction 9' was decreased by a factor of 5 resulting in a decrease in the electron density of approximately a factor of 1.8. A corresponding decrease in the rates of reactions 8 and 10 produces a similar result. However, a decrease of a factor of 5 in the rate coefficient for reaction 7 results in an increase in predicted electron density by a factor of approximately 1.8. These calculations illustrate that the results presented here for the  $CO^+ + e^-$  rate coefficient are sensitive to the rate coefficients of reactions 7-10.

The reaction rate-coefficient expression obtained here for the deionization of  $CO^+$  at high temperatures is consistent with previous

measurements<sup>1-3</sup> for the  $\text{NO}^+$  ( $k_r = (6.7 \pm 2.3) \times 10^{21} T_e^{-1.5}$ ),  $\text{N}_2^+$  ( $k_r = (1.5 \pm 0.5) \times 10^{22} T_e^{-1.5}$ ), and  $\text{O}_2^+$  ( $k_r = (8 \pm 2) \times 10^{21} T_e^{-1.5}$ ), two-body dissociative recombination reactions. Though this comparison is only qualitative, it does suggest that the rate coefficients for the charge-transfer reactions are not drastically in error.

Figure 10 presents a comparison between the  $\text{CO}^+ + e^-$  rate coefficient data of this paper and the previous low-temperature data of Mentzoni and Donohoe.<sup>18,19</sup> The measurements were not obtained at comparable electron temperatures so direct comparison is not possible. However, the present data can be extrapolated to lower temperatures by applying the technique used by Hansen<sup>27</sup> in his  $\text{NO}^+ + e^-$  study and by ourselves in our  $\text{N}_2^+ + e^-$  and  $\text{O}_2^+ + e^-$  studies.<sup>2,3</sup> The procedure used here was to match a  $T_e^{-0.5}$  temperature dependence to our data at the characteristic vibrational temperature of  $\text{CO}^+$  ( $\theta_v = 3140^\circ\text{K}$ ). This extrapolation is seen to agree reasonably well with the low-temperature data of Mentzoni and Donohoe.

## 2.6 Conclusions

The  $\text{C}^+ + e^- + e^-$  three-body recombination rate coefficient and the  $\text{CO}^+ + e^-$  two-body dissociative recombination rate coefficient have been measured in carbon monoxide plasmas that have expanded from equilibrium reservoir conditions of  $7060^\circ\text{K}$  at 17.3 atm pressure and  $6260^\circ\text{K}$  at 10.0 atm pressure respectively. The resulting reaction rate coefficient for the recombination of  $\text{C}^+$  is given by  $k_{r1} = (2.2 \pm 0.7) \times 10^{40} T_e^{-4.5} \text{ cm}^6/\text{mole}^2 \text{ sec}$  for an electron temperature range of approximately  $1500^\circ\text{K}$  to  $7000^\circ\text{K}$ . The reaction rate coefficient for the recombination of  $\text{CO}^+$  is given by  $k_{r2} = (1.5 \pm 0.3) \times 10^{22} T_e^{-1.5} \text{ cm}^3/\text{mole sec}$  for an electron temperature range of approximately  $1200^\circ\text{K}$  to  $6200^\circ\text{K}$ . The reader is cautioned that in order to obtain the  $\text{CO}^+$  deionization rate coefficient it was necessary to estimate the rate coefficients for several of the charge-transfer reactions. However, the results obtained are consistent with the dissociative recombination rate coefficients obtained for  $\text{NO}^+$ ,  $\text{N}_2^+$  and  $\text{O}_2^+$ .

## 3. LABORATORY MEASUREMENTS OF ELECTRON DENSITY AND ELECTRON TEMPERATURE WITH RAM FLIGHT PROBES

The National Aeronautics and Space Administration has for several years conducted in-flight radio attenuation measurements (RAM) in order to improve understanding of the causes and methods of predicting<sup>30,31</sup> or preventing<sup>32,33</sup> the radio-signal degradation during earth entry of a space vehicle. In the last few years, electrostatic probes projecting from the spacecraft into the boundary layer and inviscid flow have been flown in an attempt to measure in-flight electron-density distributions.<sup>34</sup> On-board diagnostic antennas,<sup>35,36</sup> reflectometers,<sup>37</sup> and VHF antennas<sup>38</sup> have also been used to obtain information about the surrounding plasma. Prior to flying the

diagnostic antennas, measurements of the admittance of the RAM C and RAM C-C antennas were performed<sup>39,40</sup> in a shock-tube facility. Such measurements can be very helpful in correctly interpreting the flight data.

The use of electrostatic probes to measure the electron density in the plasma layer of an entering spacecraft has been extensively discussed.<sup>41,42</sup> Smetana<sup>43</sup> developed a technique for obtaining electron densities from the ion current collected by constant-voltage wires located in a two-dimensional rarefied plasma stream. This theory was used by Scharfman<sup>41,42</sup> in reducing probe data obtained in an inviscid shock-tube flow to demonstrate the applicability of the theory to within a factor of  $\pm 2$  for the RAM C-1 probe for conditions at which the flow was free molecular with respect to the wire diameter. It was difficult to investigate the probe operation in a boundary-layer flow in this facility because the boundary layer was too thin for conditions at which sufficient uniform test flow could be obtained.

The purpose of this section is to describe laboratory measurements of electron density obtained in the inviscid and boundary-layer flow of a conical nozzle using the RAM C-1 constant bias-voltage probe and measurements of electron density and electron temperature obtained in the inviscid flow using the RAM C-C voltage-swept thin-wire probes. An important difference between the experiments discussed in this report and those mentioned above is that relatively thick boundary layers with electron temperatures significantly greater than the heavy-particle translational temperatures can be obtained on the sidewall of the nozzle. Both the previous shock-tube experiments and the present nozzle experiments contribute to establishing confidence in the interpretation of the flight data obtained with the electrostatic probes.

### 3.1 Experimental Apparatus and Technique

The shock tube and nozzle described in Section 2 and shown in Fig. 1 was also used for these experiments. The test gas used here was UPC nitrogen supplied by Air Product and Chemicals, Inc. A chemical analysis of the gas indicated the following: oxygen less than 0.5 ppm, total hydrocarbons less than 1 ppm, and water less than 0.15 ppm. The shock tube was purged with the test gas to approximately 5 torr just prior to each run. A detailed discussion of the nozzle starting process, uniform-flow duration, and boundary-layer growth has been previously presented.<sup>44,45</sup> The dominant chemical species at the nozzle measuring stations were calculated<sup>2</sup> to be  $N_2$ ,  $N$  and  $N^+$ .

The RAM C-1 electrostatic probe consists of eight iridium wires with a length of approximately 0.180 inches and a diameter of approximately 0.009 inches. The wires are supported on a wedge-shaped dielectric material with the center-to-center separation distance between adjacent wires of approximately 0.4 inches. The wires were located in the nozzle so that their length was perpendicular to the velocity vector. These wires were operated

in the inviscid flow at axial locations of 14.5, 32.5 and 42.5 inches from the throat and in the boundary layer at 34.5 inches from the throat. The probe voltage was maintained constant at -5 volts relative to the side collectors.

At the nozzle locations noted above, voltage-swept thin-wire probes aligned with the flow direction were used to obtain an independent measurement of the electron density and electron temperature. The ion-current portion of the probe characteristic was used to infer the electron density. The experimental procedure used to obtain the Langmuir-probe data in this nitrogen plasma has been described in detail in previous papers.<sup>2,26</sup>

The RAM C-C flight probe consists of four lengths of iridium wire with diameter and length of approximately 0.0047 inches and 0.41 inches, respectively. These wires were mounted in a wedge-shaped dielectric material similar to the RAM C-1 probe but in this case the wires were oriented parallel to the flow direction. In the present experiments, the voltage on these probes was swept from -5 to +2 volts in approximately 80  $\mu$  sec, which is slow enough to avoid transient effects.<sup>46</sup> In some cases the voltage ramp was referenced to tunnel ground and in other cases it was referenced to the side collectors. The results were insensitive to the voltage reference. However, the inferred electron density and electron temperature were found to be very sensitive to probe contamination as will be discussed later.

During all of the experiments noted above an independent measurement of the integrated free-stream electron density was obtained just upstream of the probe stations using microwave interferometers operating at frequencies of either 35 or 17 GHz.

### 3.2 Discussion of Constant Bias-Voltage Probe Results in Inviscid Flow

It was noted above that the RAM C-1 probe was used in the inviscid flow at axial locations of 14.5, 32.5 and 42.5 inches. Figure 11 presents the relative magnitudes of the mean free paths  $\lambda_{i-n}$ ,  $\lambda_{n-n}$ ,  $\lambda_{e-n}$ ,  $\lambda_{i-i}$ , and  $\lambda_{e-e}$  as a function of inviscid area ratio. These values were calculated using the expressions summarized by Sonin<sup>25</sup> and the previously reported nozzle-flow properties.<sup>2</sup> For the purpose of estimating mean free paths, the electron temperature can be assumed to be equal to the heavy-particle translational temperature from the reservoir down to 3500°K at which point it can be considered to freeze. Measuring stations at 12.5, 32.5 and 42.5 inches are located on Fig. 11. Also included in Fig. 11 is the relative magnitude of the various probe radii used, i.e., 0.002 and 0.0045 inches. At all of the measuring stations the electron mean free paths are large compared to the probe radius. Figure 11 further shows that at the 14.5-inch measuring station the RAM C-1 wire diameter is sufficiently large that interpretation of data using free-molecule theory should not provide the correct electron densities because current collection should be inhibited by the relatively small values of  $\lambda_{i-n}$  and  $\lambda_{n-n}$ . At the 32.5- and 42.5-inch stations the 0.009-inch diameter probes should be in free-molecular flow. It was therefore decided to operate the RAM C-1 probe at 32.5 and

42.5 inches from the throat to confirm the data reduction technique, and at 14.5 inches to investigate the influence of collisions on the number density deduced using the free-molecular flow theory.

Figure 12 illustrates typical RAM C-1 probe and microwave-interferometer data records obtained in the inviscid portion of an expanding nitrogen plasma at 32.5 inches from the throat. Figures 12(a) and (b) are the probe outputs for wires 4, 5, 7 and 8 (see Fig. 13 for relative location) obtained across a 1000 ohm resistor with a constant bias voltage of -5 volts relative to the probe side collectors. The test-flow period is delineated on the data records. The nozzle starting process<sup>44</sup> is also evident on these data records. Figure 12(c) is the 17 GHz microwave interferometer record obtained one inch upstream of the electrostatic probes. The electron density measured with this interferometer is used as the reference with which the number density calculated from the probe current is compared.

Before calculating the number density from the probe data it is helpful to know the local electron temperature. These temperature measurements were performed in previous experiments and were repeated here for verification. As shown in Fig. 5 of Ref. 2 an average value of 3500°K is representative of the plasma at the 32.5- and 42.5-inch locations. The corresponding heavy-particle translational temperature calculated for these stations is in the range 500 to 600°K. It should be noted that the electron densities obtained from the theory are a weak function of temperature. That is, if 500°K were used as the electron temperature instead of 3500°K, then the electron density would be overpredicted by approximately 15 to 20 per cent which is within the experimental scatter presented in Figs. 13 and 14. From the viewpoint of flight-data analysis this insensitivity is important because it suggests that knowledge of  $T_e$  is not essential for reduction of the RAM C-1 probe data. It should be emphasized that this observation is not true when obtaining electron densities from voltage-swept probes aligned with the flow since in this case the number density is approximately proportional to the square root of the electron temperature. The RAM C-1 data analysis procedure has been discussed in detail elsewhere<sup>32,41,42</sup> and will not be repeated here.

Figures 13 and 14 present the ratio of the number density deduced from the probe to that obtained from the microwave interferometer with the probe located in the inviscid flow at 32.5 and at 42.5 inches from the throat, respectively. Boundary-layer measurements were previously performed<sup>45</sup> at these stations for similar reflected-shock reservoir conditions but with air as the test gas instead of nitrogen. The boundary-layer thicknesses should not be significantly different for these two gases. At the nozzle stations of interest here the width of the uniform inviscid flow is approximately 21 to 24 inches which is considerably larger than the 3.53-inch width of the RAM C-1 probe.

At each location the experiment was repeated approximately 12 to 14 times as indicated by the separate symbols. The centerline of the wedge leading edge was located on the nozzle centerline. Figures 13 and 14 illustrate that for the majority of the measurements the ratio was in the range

from 0.80 to 1.20. Part of this scatter is due to the slight nonuniformity of the plasma as illustrated by Fig. 12(c) and part is due to the accuracy with which the data records shown in Figs. 12(a) to 12(c) can be read. On the basis of this comparison it was concluded that the theory predicts the correct electron density when used in the flow regime for which it was intended.

After completing the electrostatic-probe measurements in the free-molecular-flow regime, the probe was moved to a location 14.5 inches from the nozzle throat (where the uniform inviscid-flow width was approximately 5 inches) and the experiment was repeated. From Fig. 11 one sees that at this location both  $\lambda_{n-n}$  and  $\lambda_{i-n}$  were less than the wire radius. The ratio of the probe radius to this ion-neutral mean free path was approximately 2.8. Since the probes were in a transition-flow regime, interpretation of the collected-current data in terms of Smetana's free-molecular flow theory should not be expected to give the correct results. However, this theory was employed to deduce the number densities in order to qualitatively evaluate the sensitivity of the results to collisions. The results of these measurements are presented in Fig. 15 and illustrate that the probe-deduced number densities were approximately 0.6 to 0.9 of the microwave interferometer values. The lower number densities measured by probes #1 and #8 at the extremities of the 3.53-inch wide probe suggest that the electron density may vary by approximately 10 to 15 per cent across the 5-inch wide inviscid core. However, this variation is not important for the purposes of this study since the remaining data suggest that if the probe is operated in a transition flow, then the number densities obtained in the conventional manner will be somewhat less than actual.

The influence of collisions on the inferred number density discussed above is considerably less than that obtained in previous work by Weissman, et al.<sup>47</sup> These authors performed experiments under conditions for which the ratio of the probe radius to ion-neutral mean free path was the same as experienced here but they found that the inferred number density was approximately 0.05 of the microwave interferometer values. The difference between the results of the two experiments is felt to be due to a free-stream velocity effect since Weissman's experiments were performed in a low-velocity flame facility in contrast to the much higher-velocity flow of the shock-tunnel results reported here.

A simple analysis has been published by Talbot and Chou<sup>24</sup> that has been used successfully<sup>26</sup> to correct thin-wire data (aligned with the flow direction) for collisional effects. The analysis is a scheme for interpolating between the free-molecular theory of Laframboise<sup>23</sup> and the collision dominated results of Shulz and Brown.<sup>48</sup> The technique of Talbot and Chou in its present form is not applicable to the RAM C-1 geometry but it would be helpful for extending the altitude range of the probe data if such a correction technique could be found. A brief but unsuccessful literature search was made for an appropriate correction technique.

### 3.3 Discussion of Constant Bias-Voltage Probe Results in Boundary-Layer Flow

The RAM C-1 probe was also used to obtain the electron-density distribution in the nozzle-wall boundary layer at 34.5 inches from the nozzle throat. The electron-temperature distribution and an independent measurement of the electron-density distribution were obtained using voltage-swept thin-wire Langmuir probes. Detailed boundary-layer velocity and density distributions had previously been performed at this nozzle location (using air as the test gas) and the results suggested that the wire probes should be in a free-molecular flow regime. The velocity distribution from Ref. 45 was used in reducing the probe data because of the similarity in test conditions. The measured electron temperatures presented in Fig. 16 were also utilized. The boundary-layer thickness ( $\delta$ ) and displacement thickness ( $\delta_*$ ) noted on Figs. 16 and 17 were calculated using the method given by Burke and Bird<sup>22</sup> for a turbulent boundary layer. The boundary-layer and displacement thicknesses calculated in this manner have been shown to be in good agreement with experimental data for reflected-shock reservoir conditions similar to those used here but with air as the test gas. Calculations indicate that the nozzle-wall boundary-layer growth for nitrogen should be very similar to what it was for air.

The temperature results presented in Fig. 16 suggest that the electron temperature decreases as the nozzle wall is approached. The scatter in the data is approximately  $\pm 15$  to 20 per cent which is somewhat greater than previously experienced ( $\pm 10$  per cent) with the thin-wire probes when they were used in the inviscid-flow environment.

The electron-density distribution measured in the wall boundary layer is presented in Fig. 17. The results obtained with the RAM C-1 probe are shown to be in good agreement with the voltage-swept Langmuir probe measurements. As previously mentioned, these latter number densities were obtained from the ion-current portion of the current-voltage characteristic. Typical data records for these probes and the interpretation method has been previously presented.<sup>2,49</sup> The scatter in the thin-wire electron-density measurements is again somewhat greater than previously experienced using the same diagnostic technique in the inviscid flow.

It was noted in Ref. 2 that the indicated number density can be greater than the real value when using thin-wire probes in a region where the ratio of probe radius to Debye length becomes less than one. Care was taken in these experiments to avoid this problem by using relatively large diameter wire (still within constraints of free-molecular flow) in the low electron-density region of the boundary layer.

Within the accuracy of the experimental data presented in Fig. 17 the electron-density distribution appears to approach the measured free-stream value at approximately 2.25 inches from the wall. As noted, this is in good agreement with the anticipated boundary-layer thickness. Further, the electron-density distribution obtained with the RAM C-1 probe appears to be

in good agreement with the distribution obtained with the thin-wire probes.

### 3.4 Discussion of RAM C-C Swept-Voltage Probe Data in Inviscid Flow

The RAM C-C swept-voltage probe was operated in the inviscid flow at 32.5 inches from the nozzle throat. The probe voltage was swept from -5 to +2 volts referenced to either tunnel ground or the side collectors. The electron-density and electron-temperature results were found to be independent of the voltage reference. At this nozzle location the wires were in the free-molecular flow regime (see Fig. 11) and thus the theory of Laframboise was used in the data reduction.

The electron-density and electron-temperature measurements obtained with this probe were found to be in excellent agreement with previous thin-wire measurements at this nozzle location. The electron-density measurements were also in good agreement with simultaneously obtained microwave interferometer values measured one inch upstream of the probes.

In order to obtain reproducible data from the swept-voltage probes it is essential that the surface be free of contaminants. Experience with these probes indicates that when the surface is contaminated, high electron temperatures are indicated. This observation is consistent with that reported in Ref. 50. It is normal laboratory procedure to ultrasonically clean each probe immediately prior to each experiment in a dilute solution of sodium hydroxide if the probe is tungsten or a dilute sodium chloride-hydrochloric acid solution if the probe material is iridium. The probe is used for a single run and then discarded. It thus becomes important for the flight application to have some idea of the susceptibility of the flight probes to relatively small contamination levels. For this reason, the probes were operated for three consecutive experiments without cleaning. For each experiment the probe is exposed to the high-temperature test gas and interface gas for a total time of approximately one millisecond. The electron temperature results obtained in these experiments were reproduced with  $\pm 10$  per cent which is within the limits of normal experimental scatter. Further use in the absence of cleaning resulted in increases in indicated electron temperatures by a factor of two to four. The identity or quantity of the contaminant responsible for the increased temperatures is not known at the present time.

### 3.5 Concluding Remarks

The RAM C-1 and RAM C-C flight probes have been used to measure electron density and electron temperature in the inviscid and boundary-layer flow of the conical nozzle of a reflected-shock tunnel. Nitrogen was used as the test gas and was expanded from an equilibrium reservoir condition of 7200°K and 17.1 atm.

The electron densities deduced from the current collected by the RAM C-1 probe and Smetana's theory were found to be in good agreement with

independent measurements when the conditions of the theory were obeyed. The electron densities and electron temperatures measured with the RAM C-C probe were also in good agreement with independent measurements. However, the electron-temperature measurement is sensitive to probe-surface contamination which could be troublesome at some point in the re-entry trajectory.

#### 4. ANTENNA ADMITTANCE MEASUREMENTS IN THE PRESENCE OF IONIZED BOUNDARY LAYERS

The purpose of this phase of the studies was to investigate the agreement between measured and predicted antenna admittance for a known distribution of electron density in the plasma layer adjacent to the plate surface. This research is essentially an extension of the work of Taylor<sup>40</sup> who has previously measured the admittance of the antennas used here in a shock-tube flow under much different conditions. His boundary layers were much thinner than the present ones and the length of the uniform plasma was much less. The collision frequency,  $\nu/\omega$ , of his plasma (0.1 torr experiments) was less than 0.15 which is of the same order as that obtained here. Taylor illustrates good comparison between his experimental data and the predictions of Croswell, et.al.<sup>51</sup> At the present time, the theoretical calculations (being performed by W. F. Croswell and C. T. Swift of the Langley Research Center) for the conditions of interest here cannot be finalized because a more detailed study of the boundary-layer electron-density profiles for the carbon monoxide plasma is yet to be completed.

As part of this research, two S-band and one X-band antennas typical of the RAM flight hardware were mounted in a sharp flat-plate model which was subsequently placed in the fiberglass nozzle of the shock tunnel (see Fig. 1). The boundary layer over the plate provided an electron-density gradient in the near field of the antennas. This boundary-layer was sufficiently thick so as to permit good resolution of the electron-density profile by detailed probing with thin-wire Langmuir probes.

The initial antenna-admittance and electron-density measurements were conducted in an argon +0.12% nitrogen test gas. The boundary layer was probed in detail at two locations along the plate and the result will be discussed later in this section. Using this test gas, it was possible to achieve critical electron density for the 3348 MHz antennas but difficult to obtain values sufficiently in excess of critical to investigate the antenna response for overdense plasmas. The test gas was changed to carbon monoxide and sufficiently high electron densities were obtained to achieve this goal. All of these measurements were performed for low collision frequency plasmas ( $\nu/\omega \leq 0.15$ ) and therefore the influence of collisions on the results was not investigated. However, it is considered important to investigate the influence of collisions, but that will necessarily be done at a later date. As previously mentioned, the electron-density distributions in these boundary layers are not precisely known because it was not possible to probe the

carbon monoxide boundary layers under support of the current contract. However, for the purposes of preliminary calculations, the profiles measured in the argon plus 0.12% nitrogen plasma can be used because the gas dynamic parameters and the chemical kinetics are similar for the test conditions considered.

The width of the ground plane used in these experiments was such that it was not possible to move the flat plate sufficiently close to the nozzle throat so as to achieve X-band critical electron density. It is currently planned to re-structure the model so that this can be done in the future. In so doing, the collision frequency,  $\nu/\omega$ , will also be increased. For this reason, the discussion presented here will be confined to the admittance measurements obtained with the two S-band antennas.

#### 4.1 Electron-Density Distributions in Boundary Layer Over Flat Plate Model

In preparation for the antenna admittance measurements, the boundary-layer electron-density profiles at two plate locations were measured. The plate was located in the inviscid nozzle flow such that the leading edge was at 22.5 inches from the throat and the top surface was on the nozzle centerline. The test gas used in these experiments was argon plus 0.12 per cent nitrogen. The reflected-shock processed gas was at an equilibrium reservoir condition of 12,150°K at 30.1 atm pressure. The dominant chemical species at the leading edge of the plate were calculated to be Ar and Ar<sup>+</sup> and the free-stream Mach number was calculated to be 15.0.

A small amount of nitrogen (0.12 per cent) was added to the argon test gas in order to obtain ionization equilibrium in the reflected-shock reservoir prior to termination of the useful test time. As a result of this nitrogen addition, the electron temperatures in the expansion are greater than the argon temperatures because of the electron thermal energy transfer with the vibrational degrees of freedom of molecular nitrogen.<sup>52</sup>

The flat-plate model was 7-inches wide by 30-inches long. The top surface was constructed of plexiglas with the exception of a 1-inch long stainless steel leading edge. Boundary-layer surveys were performed at distances from the leading edge of 6.75 and 19.25 inches. At the most upstream location, the flow is considered to be two-dimensional since spanwise static-pressure measurements obtained by Boyer<sup>53</sup> at 5 and 10 inches from the leading edge, for similar flow conditions, indicated that the flow was uniform across the plate. However, for the 19.25 inch location pressure measurements were not obtained, and it is possible that the flow here may not have been two-dimensional.

During all of the experiments noted above an independent measurement of the integrated freestream electron density was obtained just upstream of the probe stations using microwave interferometers operating at frequencies of either 35 or 17 GHz.

The voltage-swept thin-wire probes used for these measurements were described in previous sections. In performing the probe measurements, care was taken to keep the probe holder far out in the flow to avoid any possible interference effects in the subsonic flow region. The quartz tubing surrounding the probes was bent as shown in Fig. 18. The 1/16-inch diameter tubing used in the probe construction did not permit probing to distances less than 0.060 inches off the plate surface.

A typical swept-voltage probe data record obtained at 0.060 inches from the plate surface is shown in Fig. 19. Also shown is a 17 GHz microwave-interferometer data record obtained 1-inch upstream of the leading edge. The calculated Mach number of the freestream at the leading edge of the plate was equal to 15.0 and the mean free paths were as follows:

$\lambda_{e-e} \cong 1.5$  cm,  $\lambda_{i-i} \cong 1.7 \times 10^{-3}$  cm,  $\lambda_{e-n} \cong 2.7$  cm,  
 $\lambda_{n-n} \cong 7.8 \times 10^{-3}$  cm, and  $\lambda_{i-n} \cong 2.4 \times 10^{-3}$  cm. The magnitude of these mean free paths increased with increasing distance from the throat. At the first measuring station over the plate the smallest of these mean free paths,  $\lambda_{i-i}$ , was about 0.5 of the probe radius. It was assumed that the probes were operating in free molecular flow and the free molecular flow theory<sup>23</sup> was used in reducing the data.

Number-density measurements obtained in the boundary layer at 6.75 inches are shown in Fig. 20. The measurements approach the estimated freestream value at approximately  $1.0 \pm 0.2$  inches from the surface and decrease by an order of magnitude as the wall is approached which is consistent with the estimated gas density in this region.

The leading edge of the flat plate (first 1 inch) was constructed of stainless steel and the remainder of the plate surface was plexiglas. It was realized that this construction represents a potential step-function change in surface catalysis. However, results presented by Chung<sup>54</sup> suggest that such a change should not influence the boundary-layer profiles at the two downstream measuring stations for these experiments. The dominant ion in this flow environment was calculated to be  $\text{Ar}^+$ . In addition, the freestream  $\text{Ar}^+$  concentration was found to be frozen well upstream of the plate leading edge. It is thus unlikely that gas-phase recombination of ions and electrons in the boundary layer would be important. Also doubtful is the possibility that the plexiglas surface would provide a good catalyst for surface recombination which would then result in a diffusion controlled boundary layer that could have a profile consistent with the measurements. Most likely, the boundary-layer electron concentration was frozen at an upstream value and the measured profile reflects the boundary-layer gas-density distribution. However, it is difficult to be certain of the mechanism responsible for the measured number-density profile. The scatter in these ion-density data is less than experienced in the wall boundary layer but consistent with that observed in inviscid-flow measurements.

The flat-plate boundary layer electron-temperature measurements are presented in Fig. 21. Unfortunately, there was significant scatter in the results of these temperature measurements. It was not possible to observe

the trend of decreasing electron temperature through the boundary layer as was seen in the nozzle-wall experiments reported here and in the previous flat-plate experiments of Tseng and Talbot.<sup>55</sup> On the basis of these measurements it could only be concluded that the electron temperature was relatively constant through the boundary layer at a level considerably higher than the argon translational temperature of approximately 130°K.

Electron-density and electron-temperature measurements obtained at 19.25 inches from the leading edge are presented in Figs. 22 and 23. The number-density measurements suggest a reasonably thick boundary layer on the order of 2.0 inches, at which the measured number density approaches the estimated freestream value of  $4.0 \times 10^{10} \text{ e}^-/\text{cm}^3$ . This estimate of the number-density is included for comparison purposes and was obtained from microwave-interferometer data taken at the measuring station in the absence of the plate. This comparison assumes that the plate does not significantly disturb the flow. The decrease in the outer-flow electron density between the 6.75 and 19.25 inch locations is consistent with that anticipated as a result of gas-density decrease and frozen electron concentration.

The electron-temperature data presented in Fig. 23 suggests that the electron temperature was relatively uniform through the boundary layer. The data scatter is considerably less than experienced at the 6.75 inch location. The explanation for this difference is not clear since the same diagnostic techniques and flow environment were used to obtain the measurements. Comparison of Figs. 21 and 23 suggests that the electron temperature was not only constant through the boundary layer, but it was also relatively constant along the plate. This observation is consistent with a frozen boundary-layer flow in the absence of energy sinks such as thermalization, exchange with vibration, etc. and the absence of energy sources such as recombination.

#### 4.2 Admittance Measurements with RAM Antennas

Figure 24(a) and (b) illustrate the RAM C-C S-band antenna (3348 MHz) and the RAM C S-band (3348 MHz) and X-band (10044 MHz) antennas mounted in the flat-plate model. As can be seen from Fig. 24(b), the RAM C-C antenna does not extend through the plexiglas top surface of the plate. However, both of the RAM C antennas do so that their apertures are immediately adjacent to the ionized boundary layer. For all of the data reported in this section, the test gas was carbon monoxide. It should be emphasized that the boundary-layer measurements described earlier were performed in an Argon + 0.12% nitrogen test gas. A description of the flat-plate construction is given in Section 4.1.

Schematic diagrams of the S-band and X-band four-probe reflectometers are given in Figs. 25 and 26. The reflected signal was also monitored as indicated on the schematics. These systems were very convenient for data reduction purposes in that five arcs were always available for Smith-Chart construction. Waveguide instead of coaxial cable was used wherever possible in the systems.

In the remainder of this section, the experimental data obtained to date for the RAM C and the RAM C-C S-band antennas are described separately. As previously noted, the electron densities at the measuring stations were not sufficiently high to excite the X-band antenna.

4.2.1 RAM C S-band antenna measurements. - As part of the pre-experiment calibration, the diode spacings were measured using a moveable short. If the microwave diodes are numbered so that #1 is nearest the generator and #4 is nearest the short, then the spacings were  $1-2 = 0.1255 \lambda_G$ ,  $2-3 = 0.1218 \lambda_G$ ,  $3-4 = 0.1278 \lambda_G$ , and  $4-1 = 0.1252 \lambda_G$  where  $\lambda_G$  was the guide wavelength of 11.378 cm. The reflectometer system was tuned using a matched load with VSWR of approximately 1.025 to 1.035. Each of the diodes was then calibrated as follows. An attenuation of 3 db was set on the variable attenuator and the four diode outputs were adjusted until they were equal. The attenuation was increased in increments of 1 db until reaching 26 db. The attenuator was then set to  $\infty$  attenuation and the final readings taken. The voltages were normalized so that the diode output at 3 db attenuation represented the radius of the Smith Chart. During the experiments this 3 db tare was always set on the variable attenuator.

The free-space admittance was measured with the antenna inside and outside of the shock tunnel, but no difference was observed between the results. Aluminum foil was then placed over the antenna aperture to obtain the antenna short reference. In addition, the coaxial cable was shorted at the antenna input terminal to obtain an additional reference.

This antenna was operated at two locations in the flat plate, 6.75 and 11.25 inches from the leading edge. The major differences between these measuring stations are the boundary-layer thickness and the peak value of the electron density. Previous Langmuir-probe measurements in the argon-nitrogen test gas suggested that the boundary-layer peak electron density would be nearly equal to the freestream value at the antenna location. Three experiments were performed at the 6.75-inch location, but in each case the plasma was considerably overdense. Several additional experiments were performed at the 11.25-inch location and these spanned the range from underdense thru critical to overdense. The results of these experiments are given in Table 2.

Figure 27 is typical of the reflectometer and microwave-interferometer oscilloscope records obtained. The test-flow duration is noted on the oscilloscope records. The 50- $\mu$ sec duration pulse near the right side of these records is the zero-signal level obtained by turning off the TWT and the microwave interferometer power supply with a gating pulse. The horizontal line is the no-plasma signal level recorded approximately two milliseconds prior to plasma arrival at the plate leading edge. A limited number of lower confidence-level data points can be obtained from the post-test time plasma. In some cases this was done and the data points are so designated in the discussion to follow.

The measured voltage reflection coefficients are presented in Fig. 28 as a function of peak electron density over the antenna divided by critical electron density for 3348 MHz (approximately  $1.4 \times 10^{11} \text{ e}^-/\text{cm}^3$ ). Recall that these electron densities are obtained by extrapolating upstream microwave interferometer measurements because Langmuir-probe measurements above the plate were not performed for carbon monoxide test gas. Previous experience in an argon-nitrogen test gas has indicated that this type of extrapolation gives reasonably good results.

One of the more interesting results of these experiments is the difference between the voltage reflection coefficients of approximately 1.0 measured at the 6.75-inch location and the value of approximately 0.70 measured at the 11.25-inch location for  $n_e/n_{e,cr}$  values in the range 1.5 to 3. The most obvious difference between these locations is that the boundary layer was somewhat thinner at the upstream location than it was downstream suggesting that boundary-layer thickness may have a significant influence on the results. The data presented in Fig. 28 also illustrate a rapid change in reflection coefficient in the range  $0.4 < n_e/n_{e,cr} < 1.0$ . Outside of this number-density range, the reflection coefficient alone is not a sensitive indicator of electron density.

All of the results obtained with this antenna are plotted on a single Smith Chart and given in Fig. 29. The circles indicate this uncertainty in the five arc intersections. The phase rotation and voltage reflection coefficient with changing electron density are both illustrated by this plot. For purposes of completeness, these phase measurements and their estimated uncertainty are replotted in Fig. 30 as a function of  $n_e/n_{e,cr}$ .

As previously noted, the reflection coefficient was essentially zero when the X-band antenna was used at these locations even for the highest electron densities. For this reason, the X-band results are not presented here.

4.2.2 RAM C-C S-band antenna measurements. - The RAM C-C antenna was installed in the flat plate at 6.75 inches from the leading edge and the top side of the plate was located on the nozzle centerline with the leading edge at 22.5 inches from the nozzle throat. Carbon monoxide was used as the test gas so that relatively high electron-density levels could be achieved in the boundary layer over the plate. The average freestream electron density was measured at 11.5 and 21.5 inches from the nozzle throat using microwave interferometers.

The reflectometer diode spacings for these experiments were the same as those given in Section 4.3.1 for the S-band system. The free space admittance was found to be independent of whether the antenna was inside or outside of the fiberglass nozzle. Aluminum foil was placed under the plexiglas and over the antenna aperture to obtain the aperture-short reference. The coaxial cable was also shorted at the antenna input terminal in order to obtain an additional reference.

For these experiments, the peak electron density over the antenna was varied in the range of approximately  $0.6 < n_e/n_{e,cr} < 2.9$  by adjusting the strength of the incident shock. The experimental results obtained, including the arc lengths for the five diodes, are summarized in Table 3.

Figure 31 is typical of the oscilloscope records obtained for the reflectometer diodes and the microwave interferometers. The test time is noted on the oscilloscope records as are the no-plasma voltages and the voltages with the TWT and interferometer power supply turned off. Once again, it was possible to use the post test-time flow (see Fig. 31(g)) and obtain lower confidence-level microwave-interferometer and reflectometer data.

All of the reflectometer data obtained in the CO plasma with the RAM C-C antenna are presented on the Smith Chart of Fig. 32. Again, the circles represent the uncertainty of the measurements as determined by the intersection of the five diode voltages. Much of the phase rotation uncertainty associated with these records was due to the #1 diode arc being consistently long. Care was taken to calibrate each of the oscilloscopes just prior to and after each experiment using a VTVM, thus it is doubtful that the difficulty is associated with a calibration error. This diode appeared to operate satisfactorily when obtaining the free space admittance for which the circle of uncertainty was comparatively small.

The voltage reflection-coefficient measurements for the RAM C-C antenna are presented in Fig. 33 as a function of  $n_e/n_{e,cr}$ . The peak electron-density level at the measuring station was extrapolated from the two upstream (11.5 and 21.5-inches from the throat) microwave-interferometer measurements in the manner described in Section 4.2.1. The free space reflection coefficient (see Table 3) measured just prior to plasma arrival ranged from 0.33 to 0.36. A decrease from this free space value to a value of 0.25 was observed when the ratio of  $n_e/n_{e,cr}$  reached about 0.64 suggesting that the plasma may have tuned the antenna. In support of this suggestion, the oscilloscope record of the reflected-signal diode is given in Fig. 34 along with the microwave-interferometer oscilloscope records obtained at the upstream locations. During the useful test-flow period, the reflected signal can be seen to be significantly less than the no-plasma or free space value. For electron densities greater than  $n_e/n_{e,cr}$  of 0.64, the reflection coefficient increases rapidly to a value of approximately 0.86 at  $n_e/n_{e,cr}$  of 1.2 and remained relatively constant for increasing electron-density levels.

### 4.3 Conclusions

Number-density and electron-temperature distributions were measured in the boundary layer of a sharp flat plate at 6.75 and 19.25 inches from the plate leading edge. Significant gradients in electron density were measured through the boundary layer but the electron temperature was found to be relatively constant. In addition, the electron temperature remained

relatively constant along the plate. These measurements were performed in an argon + 0.12% nitrogen test gas. This choice of gas was unfortunate because it was later found that significantly greater electron densities could be obtained in carbon monoxide test gas. These higher number densities were necessary for the purpose of the antenna admittance measurements also reported herein.

The RAM C and RAM C-C S-band antennas were operated in the presence of an ionized boundary layer of low collision frequency. Both antennas illustrate marked increases in voltage reflection coefficient and phase rotation when the peak electron density over the antenna approached critical. The influence of boundary-layer thickness was investigated for the RAM C antenna measurements and found to be significant. Comparison of the experimental results with existing theory is yet to be completed.

#### REFERENCES

1. Dunn, M.G. and Lordi, J.A., "Measurement of Electron Temperature and Number Density in Shock-Tunnel Flows: Part II,  $\text{NO}^+ + e^-$  Dissociative Recombination Rate in Air," AIAA Journal, Vol. 7, No. 11, November 1969, pp. 2099-2104.
2. Dunn, M.G. and Lordi, J.A., "Measurement of  $\text{N}_2^+ + e^-$  Dissociative Recombination in Expanding Nitrogen Flows," AIAA Journal, Vol. 8, No. 2, February 1970, pp. 339-345.
3. Dunn, M.G. and Lordi, J.A., "Measurement of  $\text{O}_2^+ + e^-$  Dissociative Recombination in Expanding Oxygen Flows," AIAA Journal, Vol. 8, No. 4, April 1970, pp. 614-618.
4. Makin, B. and Keck, J.C., "Variational Theory of Three-Body Electron-Ion Recombination Rates," Phys. Rev. Letters, Vol. 11, No. 6, September 1963, pp. 281-283.
5. Bates, D.R., Kingston, A.E. and McWhirter, R.W.P., "Recombination Between Electrons and Atomic Ions I. Optically Thin Plasmas," Proc. Roy. Soc., A. Vol. 267, 1962, pp. 297-312.
6. D'Angelo, N., "Ion-Electron Recombination," Phys. Rev., Vol. 140, No. 5A, November 1965, p. A1488.
7. Thomson, J.J., Phil. Mag., Vol. 47, 1924, p. 337.
8. Hinnov, E. and Hirschberg, J.G., "Electron-Ion Recombination in Dense Plasmas," Phys. Rev., Vol. 125, No. 3, February 1962, pp. 795-801.
9. Motley, R.W. and Kuckes, A.F., "Recombination in a Helium

- Plasma," Proc. Fifth Inter. Conf. on Ionic Phen., Munich 1961, pp. 651-659 (North-Holland Publishing Co., Amsterdam, 1964).
10. Byron, S., Stabler, R.C. and Bortz, P.I., "Electron-Ion Recombination by Collisional and Radiative Processes," Phys. Rev. Letters, Vol. 8, No. 9, May 1962.
  11. Dugan, J.W., "Three-Body Collisional Recombination of Cesium Seed Ions and Electrons in High Density Plasmas with Argon Carrier Gas," NASA Report TN D-2004, October 1964.
  12. Abramov, V.A., "Electron-Ion Recombination in a Cesium Plasma," Teplo fizika Vysokikh Temperatur, Vol. 3, No. 1, January-February 1964, pp. 23-27.
  13. D'Angelo, N., "Recombination of Ions and Electrons," Phys. Rev., Vol. 121, No. 2, January 1961, pp. 505-507.
  14. Aleskovski, Y.M., "Investigation of Volume Recombination in a Cesium Plasma," Soviet Physics JETP, Vol. 17, No. 3, September 1963, pp. 570-575.
  15. Robben, F., Kunkel, W.B. and Talbot, L., "Spectroscopic Study of Electron Recombination with Monatomic Ions in a Helium Plasma," Phys. Rev., Vol. 132, No. 6, December 1963, pp. 2363-2371.
  16. Park, C., "Measurement of Ionic Recombination Rate of Nitrogen," AIAA Journal, 1968, pp. 2090-2094.
  17. Park, C., "Collisional Ionization and Recombination Rates of Atomic Nitrogen," AIAA Journal, 1969, pp. 1653-1654.
  18. Mentzoni, M.H. and Donohoe, J., "Electron Removal During the d.c. Discharge Afterglow of Carbon Monoxide," Physics Letts, Vol. 26A, No. 7, February 1968, pp. 330-331.
  19. Mentzoni, M.H. and Donohoe, J., "Electron Recombination and Diffusion in CO at Elevated Temperatures," Canadian Journal of Physics, Vol. 47, 1969, pp. 1789-1795.
  20. Lordi, J. A., Mates, R.E. and Moselle, J.R., "Computer Program for the Numerical Solution of Nonequilibrium Expansions of Reacting Gas Mixtures," Report AD-1689-A-6, June 1965, Cornell Aeronautical Laboratory, Buffalo, N.Y.
  21. Fehsenfeld, F.C., Schmeltekopf, A.L. and Ferguson, E.E., "Thermal-Energy Ion-Neutral Reaction Rates v. Measured Rate Constants for  $C^+$  and  $CO^+$  Reactions with  $O_2$  and  $CO_2$ ," The Journal of Chemical Physics, Vol. 45, No. 1, 1 July 1966, pp. 23-25.

22. Burke, A.F. and Bird, K.D., "The Use of Conical and Contoured Expansion Nozzles in Hypervelocity Facilities," Report 112, Cornell Aeronautical Laboratory, Inc., July 1962.
23. Laframboise, J.G., "Theory of Cylindrical and Spherical Langmuir Probes in a Collisionless, Maxwellian Plasma at Rest," Rarefied Gas Dynamics, Vol. II, Academic Press, New York, 1965, pp. 22-44.
24. Talbot, L. and Chou, Y.S., "Langmuir Probe Response in the Transition Regime," Sixth Rarefied Gasdynamics Symposium, Boston, Mass., June 1968.
25. Sonin, A.A., "The Behavior of Free Molecule Cylindrical Langmuir Probes in Supersonic Flows, and Their Application to the Study of the Blunt Body Stagnation Layer," Report 109, August 1965, Univ. of Toronto, Institute for Aerospace Studies, Toronto, Canada.
26. Dunn, M.G. and Lordi, J.A., "Thin-Wire Langmuir-Probe Measurements in the Transition and Free-Molecular Flow Regimes," AIAA Journal, Vol. 8, No. 6, June 1970, pp. 1077-1081.
27. Hansen, C.F., "Temperature Dependence of the  $\text{NO}^+ + e^-$  Dissociative Recombination-Rate Coefficient," The Physics of Fluids, 1968, pp. 904-906.
28. O'Malley, T.F., "On the Temperature Dependence of the Dissociative Recombination Rate," 6th Electronic and Atomic Collisions Conf., 1969, Boston, Mass.
29. Cunningham, A.J. and Hobson, R.M., "Experimental Measurements of Dissociative Recombination in Vibrationally Excited Gases," Physical Review, Vol. 185, No. 1, 1969, pp. 98-100.
30. Huber, P.W., Evans, J.S. and Schexnayder, C.J., "Comparison of Theoretical and Flight-Measured Ionization in a Blunt Body Reentry Flow Field," AIAA Paper 70-756, Third Fluid and Plasma Dynamics Conference, Los Angeles, California, 28 June - 1 July 1970.
31. Schexnayder, C.J., Evans, J.S. and Huber, P.W., "Comparison of Theoretical and Experimental Electron Density for RAM-C Flights," 4th Plasma Sheath Symposium, NASA Langley Research Center, October 13-15, 1970.
32. Akey, N.D. and Cross, A.E., "Radio Blackout Alleviation and Plasma Diagnostic Results From a 25,000 ft/sec Blunt-Body Reentry," NASA TN D-5615, February 1970.
33. Schroeder, L.C., "Flight Measurements at 25,000 ft/sec of Plasma Alleviation by Water and Electrophilic Injection," 4th Plasma Sheath Symposium, NASA Langley Research Center, October 13-15, 1970.

34. Jones, W.L. and Cross, A.E., "Electrostatic Probe Measurements of Plasma Surrounding Three 25,000 ft/sec Reentry Flight Experiments," 4th Plasma Sheath Symposium, NASA Langley Research Center, October 13-15, 1970.
35. Swift, C.T., Beck, F.B. and Thomson, J., "The RAM C-C S-Band Diagnostic Experiments," 4th Plasma Sheath Symposium, NASA Langley Research Center, October 13-15, 1970.
36. Swift, C.T., Croswell, W.F. and Evans, J.S., "Diagnosis of Planetary Atmospheres from Effects of Entry Plasma on Antenna Impedance," AIAA 6th Aerospace Sciences Meeting, New York, January 22-24, 1968.
37. Grantham, W.L., "Reentry Plasma Measurements Using a Four Frequency Reflectometer," 4th Plasma Sheath Symposium, NASA Langley Research Center, October 13-15, 1970.
38. Croswell, W.F. and Jones, W.L., "Effects of Entry Plasma on RAM C VHF Telemetry Antennas," 4th Plasma Sheath Symposium, NASA Langley Research Center, October 13-15, 1970.
39. Taylor, W.C., "Shock Tube Measurement of Admittance of RAM C and RAM C-C Diagnostic Antenna," 4th Plasma Sheath Symposium, NASA Langley Research Center, October 13-15, 1970.
40. Taylor, W.C., "An Experimental Investigation of the Interaction of Plasmas with Antennas," NASA CR-1727, December 1970.
41. Scharfman, W.E., "The Use of Langmuir Probes to Determine the Electron Density Surrounding Re-entry Vehicles," Final Report Contract NAS 1-3942, Stanford Research Institute, Menlo Park, California, June 1965.
42. Scharfman, W.E. and Bredfeldt, H.R., "Use of the Langmuir Probe to Determine the Electron Density and Temperature Surrounding Re-entry Vehicles," Final Report Contract NAS1-4872, NASA 66275, Stanford Research Institute, Menlo Park, California, December 1966.
43. Smetana, F.O., "On the Current Collected by a Charged Circular Cylinder Immersed in a Two-Dimensional Rarefied Plasma Stream," Third Symposium on Rarefied Gas Dynamics, 1962, Paris, France, edited by Laurmann.
44. Dunn, M.G., "Experimental Study of High-Enthalpy Shock-Tunnel Flow: Part I Shock-Tube Flow and Nozzle Starting Time," AIAA Journal, Vol. 7, No. 8, August 1969.
45. Dunn, M.G., "Experimental Study of High-Enthalpy Shock-Tunnel Flow: Part II Nozzle-Flow Characteristics," AIAA Journal, Vol. 7, No. 9, September 1969.

46. Smy, P.R. and Greig, J.R., "Transient Response of the Langmuir Probe at Low Pressure," *British Journal of Applied Physics*, Ser. 2, Vol. 1, 1968, pp. 351-359.
47. Weissman, D.E., Scharfman, W.E. and Guthart, H., "Electrostatic Probe Measurements in a Short Mean Free Path Plasma," Stanford Research Institute, Contract AF 04(694)-931, July 1966.
48. Shulz, G.J. and Brown, S.C., "Microwave Study of Positive Ion Collection by Probes," *Physical Review*, Vol. 98, No. 6, 1955, pp. 1642-1649.
49. Dunn, M.G. and Lordi, J.A., "Measurement of Electron-Temperature and Number Density in Shock-Tunnel Flows: Part I Development of Free-Molecular Langmuir Probes," *AIAA Journal*, Vol. 7, No. 8, August 1969.
50. Thomas, T.L. and Battle, E.L., "Effects of Contamination on Langmuir Probe Measurements in Glow Discharge Plasmas," *J. Appl. Physics*, Vol. 41, No. 8, July 1970, pp. 3428-3432.
51. Croswell, W.F., Taylor, W.C., Swift, C.T., and Cockrell, C.R., "The Input Admittance of a Rectangular Waveguide Fed Aperature Under an Inhomogeneous Plasma: Theory and Experiment," *Trans. Antenna and Propagation, AP.-16*, July 1968, pp. 475-484.
52. Lordi, J.A. and Dunn, M.G., "Sources of Electron Energy in Weakly Ionized Expansions of Nitrogen," Rept. AI-2187-A-16, August 1969, Cornell Aeronautical Laboratory.
53. Boyer, D.W., Private Communication of Work to be Published.
54. Chung, P.M., "Chemically Reacting Nonequilibrium Boundary Layers," *Advances in Heat Transfer*, Vol. 2, edited by Hartnett and Irvine, Academic Press, 1965.
55. Tseng, R.C. and Talbot, L., "Flat Plate Boundary Layer Studies in a Partially Ionized Gas," *AIAA 8th Aerospace Sciences Meeting*, Paper No. 70-86, New York, New York, January 1970.

Table 1 CHEMICAL KINETICS MODEL USED IN DATA CORRELATION

NO.	REACTION	THIRD BODY, M	RATE COEFFICIENT IN DIRECTION SHOWN, IN $\text{cm}^3/\text{mole sec}$ OR $\text{cm}^6/\text{mole}^2\text{sec}$	COMMENTS
1.	$\text{O}_2 + \text{M} \xrightarrow{k_f} 2\text{O} + \text{M}$	O	$2.1 \times 10^{18} T^{-0.5} \exp(-1.1796 \times 10^5/R_0T)$	
2.	$\text{O}_2 + \text{M} \xrightarrow{k_f} 2\text{O} + \text{M}$	C, CO, CO <sub>2</sub>	$1.2 \times 10^{21} T^{-1.5} \exp(-1.1796 \times 10^5/R_0T)$	
3.	$\text{CO} + \text{M} \xrightarrow{k_f} \text{C} + \text{O} + \text{M}$	C, O, O <sub>2</sub> , CO, CO <sub>2</sub>	$4.48 \times 10^{19} T^{-1.0} \exp(-2.56 \times 10^5/R_0T)$	
4.	$\text{CO}_2 + \text{M} \xrightarrow{k_f} \text{O} + \text{CO} + \text{M}$	C, O, O <sub>2</sub> , CO, CO <sub>2</sub>	$8.81 \times 10^{22} T^{-2.0} \exp(-1.256 \times 10^5/R_0T)$	
5.	$\text{CO} + \text{CO} \xrightarrow{k_f} \text{C} + \text{CO}_2$		$2.33 \times 10^9 T^{0.5} \exp(-1.305 \times 10^5/R_0T)$	
6.	$\text{O} + \text{CO} \xrightarrow{k_f} \text{C} + \text{O}_2$		$2.73 \times 10^{11} T^{0.5} \exp(-1.381 \times 10^5/R_0T)$	
7.	$\text{CO} + \text{CO}^+ \xrightarrow{k_f} \text{CO}_2 + \text{C}^+$		$1.07 \times 10^{12} T^{-0.5} \exp(-6.705 \times 10^4/R_0T)$	300°K VALUE OF $k_r = 1.14 \times 10^{15} \text{ cm}^3/\text{mole sec}$ (OR $1.9 \times 10^{-9} \text{ cm}^3/\text{sec}$ ) FROM EXPERIMENTAL DATA OF REF. 21
8.	$\text{CO} + \text{C}^+ \xrightarrow{k_f} \text{C} + \text{CO}^+$		$6.03 \times 10^{11} T^{-0.5} \exp(-6.336 \times 10^4/R_0T)$	300°K VALUE OF $k_r$ ESTIMATED TO BE $9.1 \times 10^{12} \text{ cm}^3/\text{mole sec}$ (OR $1.5 \times 10^{-11} \text{ cm}^3/\text{sec}$ )
9.	$\text{O} + \text{C}^+ \xrightarrow{k_f} \text{C} + \text{O}^+$		$6.66 \times 10^{12} T^{-0.5} \exp(-5.416 \times 10^4/R_0T)$	300°K VALUE OF $k_r$ ESTIMATED TO BE $1.7 \times 10^{14} \text{ cm}^3/\text{mole sec}$ (OR $2.8 \times 10^{-10} \text{ cm}^3/\text{sec}$ )
10.	$\text{CO} + \text{O}^+ \xrightarrow{k_f} \text{O} + \text{CO}^+$		$1.09 \times 10^{12} T^{-0.5} \exp(-9.222 \times 10^3/R_0T)$	300°K VALUE OF $k_r$ ESTIMATED TO BE $2.8 \times 10^{13} \text{ cm}^3/\text{mole sec}$ (OR $4.6 \times 10^{-11} \text{ cm}^3/\text{sec}$ )
11.	$\text{O} + \text{CO}^+ \xrightarrow{k_f} \text{O}_2 + \text{C}^+$		$5.47 \times 10^{12} T^{-0.5} \exp(-7.470 \times 10^4/R_0T)$	
12.	$\text{CO}^+ + \text{e}^- \xrightarrow{k_r} \text{C} + \text{O}$		(DETERMINED FROM THESE EXPERIMENTS SEE FIG. 9)	
13.	$\text{C}^+ + \text{e}^- + \text{e}^- \xrightarrow{k_r} \text{C} + \text{e}^-$		(DETERMINED FROM THESE EXPERIMENTS SEE FIG. 6)	
14.	$\text{O}^+ + \text{e}^- + \text{e}^- \xrightarrow{k_r} \text{O} + \text{e}^-$		$1.9 \times 10^{40} T_e^{-4.5}$	ESTIMATED BY ANALOGY TO REACTION #13 WHICH WAS MEASURED

Table 2  
SUMMARY OF EXPERIMENTAL RESULTS OBTAINED WITH  
RAM C S-BAND ANTENNA IN CARBON MONOXIDE PLASMA

RUN #	LOCATION OF ANTENNA IN PLATE	PEAK ELECTRON DENSITY OVER ANTENNA $n_e$ e/cm <sup>3</sup>	$n_e/n_{eCR}$	ANTENNA IN FREE SPACE BEFORE PLASMA ARRIVAL					ANTENNA IN FREE SPACE ROTATED AND CORRECTED FOR LINE LOSS		ANTENNA WITH PLASMA OVER APERTURE					ANTENNA WITH PLASMA ROTATED AND CORRECTED FOR LINE LOSS	
				#1	#2	#3	#4	REFL.	$\gamma$	$ \Gamma $	#1	#2	#3	#4	REFL.	$\gamma$	$ \Gamma $
				ARC	ARC	ARC	ARC	ARC			ARC	ARC	ARC	ARC	ARC		
1	POS #1	2.2 x 10 <sup>11</sup>	1.58	1.00	0.85	1.03	1.156	0.152	1.48 + j 0.02	0.192	1.800	0.92	0.505	1.662	0.652	0 - j 1.72	1.0
2	POS #1	3.4 x 10 <sup>11</sup>	2.43	1.024	0.864	1.016	1.140	0.134	1.40 - j 0.02	0.172	1.636	0.51	0.990	1.840	0.698	0 - j 3.50	1.0
3	POS #1	4.3 x 10 <sup>11</sup>	3.07	1.044	0.876	1.016	1.144	0.128	1.38 - j 0.08	0.170	1.660	0.502	1.000	1.856	0.71	0 - j 3.70	1.0
SHORT OVER ANTENNA APERTURE				1.280	0.180	1.325	1.830	0.843									
4	POS #2	2.7 x 10 <sup>11</sup>	1.93	0.95	0.89	1.07	1.12	0.148	1.35 + j 0.19	0.17	1.376	1.498	0.916	0.630	0.565	0.205 - j 0.246	0.68
5	POS #2	3.15 x 10 <sup>11</sup>	2.25	0.96	0.864	1.078	1.14	0.148	1.38 + j 0.18	0.175	1.522	1.396	0.670	0.842	0.630	0.22 - j 0.470	0.705
6	POS #2	1.58 x 10 <sup>11</sup>	1.13	0.964	0.874	1.078	1.152	0.140	1.39 + j 0.19	0.18	0.722	1.516	1.572	0.774	0.600	0.17 + j 0.450	0.780
7	POS #2	1.72 x 10 <sup>11</sup>	1.23	0.976	0.890	1.086	1.144	0.131	1.36 + j 0.18	0.165	1.136	1.620	1.200	0.434	0.58	0.175 + j 0.04	0.710
	* POS #2	1.22 x 10 <sup>11</sup>	0.87	0.976	0.890	1.086	1.144	0.131	1.36 + j 0.18	0.165	0.58	1.124	1.550	1.176	0.515	0.49 + j 0.97	0.617
8	POS #2	1.72 x 10 <sup>11</sup>	1.23	0.970	0.862	1.050	1.134	0.130	1.38 + j 0.12	0.165	1.196	1.550	1.170	0.476	0.56	0.21 - j 0.016	0.652
	* POS #2	1.08 x 10 <sup>11</sup>	0.768	0.970	0.862	1.050	1.134	0.130	1.38 + j 0.12	0.165	0.88	0.854	1.240	1.230	0.360	1.72 + j 0.85	0.38
9	POS #2	4.8 x 10 <sup>10</sup>	0.343	0.976	0.876	1.050	1.140	0.122	1.38 + j 0.10	0.165	0.976	0.876	1.050	1.140	0.122	1.38 + j 0.10	0.165
10	POS #2	3.4 x 10 <sup>10</sup>	0.243	0.944	0.876	1.064	1.122	0.140	1.33 + j 0.24	0.18	0.996	0.904	1.090	1.120	0.140	1.30 + j 0.13	0.145
11	POS #2	4.8 x 10 <sup>10</sup>	0.342	0.944	0.861	1.058	1.122	0.145	1.38 + j 0.18	0.175	0.944	0.861	1.058	1.122	0.145	1.38 + j 0.18	0.175
12	POS #2	8.3 x 10 <sup>10</sup>	0.592	0.944	0.864	1.050	1.122	0.143	1.36 + j 0.17	0.17	0.830	0.900	1.232	1.160	0.280	1.19 + j 0.70	0.315
	* POS #2	7.34 x 10 <sup>10</sup>	0.522	0.944	0.864	1.050	1.122	0.143	1.36 + j 0.17	0.17	0.856	0.762	1.110	1.240	0.305	1.70 + j 0.65	0.341
13	POS #2	8.4 x 10 <sup>10</sup>	0.600	0.976	0.876	1.050	1.136	0.142	1.38 + j 0.10	0.165	0.856	0.840	1.312	1.296	0.415	1.51 + j 0.95	0.40
14	POS #2	1.42 x 10 <sup>11</sup>	1.012	0.966	0.836	1.038	1.136	0.141	1.43 + j 0.10	0.182	0.57	1.336	1.562	0.952	0.560	0.26 + j 0.67	0.70

NOTE: 1) THE VOLTAGE REFLECTION COEFFICIENT,  $|\Gamma|$ , GIVEN HERE HAS BEEN CORRECTED FOR LINE LOSS TO GET THE UNCORRECTED VALUE, MULTIPLY BY 0.835.  
2) ANTENNA FREQUENCY WAS 3348 MHz AND THEREFORE  $n_{eCR} \cong 1.4 \cdot 10^{11}$  e/cm<sup>3</sup>  
3) \* INDICATES POST TEST-TIME DATA

**Table 3**  
**SUMMARY OF EXPERIMENTAL RESULTS OBTAINED WITH RAM C-C S-BAND**  
**ANTENNA AT PLATE POS #1 IN CARBON MONOXIDE PLASMA**

RUN #	PEAK $n_e$ OVER ANTENNA $e^-/cm^3$	$n_e/n_e^{CR}$	ANTENNA IN FREE SPACE BEFORE PLASMA					ANTENNA IN FREE SPACE ROTATED & CORRECTED FOR LINE LOSS		ANTENNA WITH PLASMA OVER APERTURE					ANTENNA WITH PLASMA ROTATED & CORRECTED FOR LINE LOSS	
			#1 ARC	#2 ARC	#3 ARC	#4 ARC	REFL. ARC	$\gamma$	$ \Gamma $	#1 ARC	#2 ARC	#3 ARC	#4 ARC	REFL. ARC	$\gamma$	$ \Gamma $
FOIL UNDER PLEXIGLAS			1.872	1.08	0.342	1.58	0.90									
15	$2.7 \times 10^{11}$	1.93	0.716	1.14	1.30	0.944	0.318	$0.48 + j0.02$	0.35	0.476	1.472	1.764	1.070	0.76	$0.072 + j0.005$	0.862
16	$3.8 \times 10^{11}$	2.71	0.728	1.164	1.32	0.952	0.325	$0.47 - j0.01$	0.36	0.610	1.570	1.74	0.956	0.772	$0.077 - j0.009$	0.880
	* $2.67 \times 10^{11}$	1.91								0.464	1.476	1.716	0.896	0.762	$0.092 - j0.038$	0.830
17	† $1.95 \times 10^{11}$	1.39	0.734	1.144	1.306	0.956	0.31	$0.49 + j0.005$	0.342	0.376	1.404	1.816	1.230	0.80	$0.060 + j0.085$	0.890
	$1.77 \times 10^{11}$	1.26								0.324	1.304	1.780	1.290	0.792	$0.065 + j0.147$	0.880
	* $2.03 \times 10^{11}$	1.45								0.276	1.396	1.764	1.142	0.792	$0.063 + j0.08$	0.880
18	$4.06 \times 10^{11}$	2.90	0.722	1.12	1.284	0.944	0.302	$0.50 + j0.025$	0.33	0.590	1.520	1.720	0.974	0.780	$0.085 - j0.075$	0.845
19	$1.32 \times 10^{11}$	0.943	0.704	1.136	1.314	0.958	0.320	$0.48 + j0.03$	0.35	0.514	1.040	1.674	1.444	0.710	$0.14 + j0.418$	0.790
	* $1.04 \times 10^{11}$	0.742								0.682	0.878	1.444	1.380	0.525	$0.34 + j0.49$	0.582
20	$9.0 \times 10^{10}$	0.642	0.704	1.136	1.310	0.96	0.318	$0.48 + j0.03$	0.35	0.796	1.020	1.240	1.056	0.249	$0.625 + j0.15$	0.25

NOTE: 1) THE VOLTAGE REFLECTION COEFFICIENT,  $|\Gamma|$ , GIVEN HERE HAS BEEN CORRECTED FOR LINE LOSS. TO GET THE UNCORRECTED VALUE, MULTIPLY BY 0.80.  
2) \* INDICATES POST TEST-TIME DATA AND † INDICATES PRE TEST-TIME DATA.

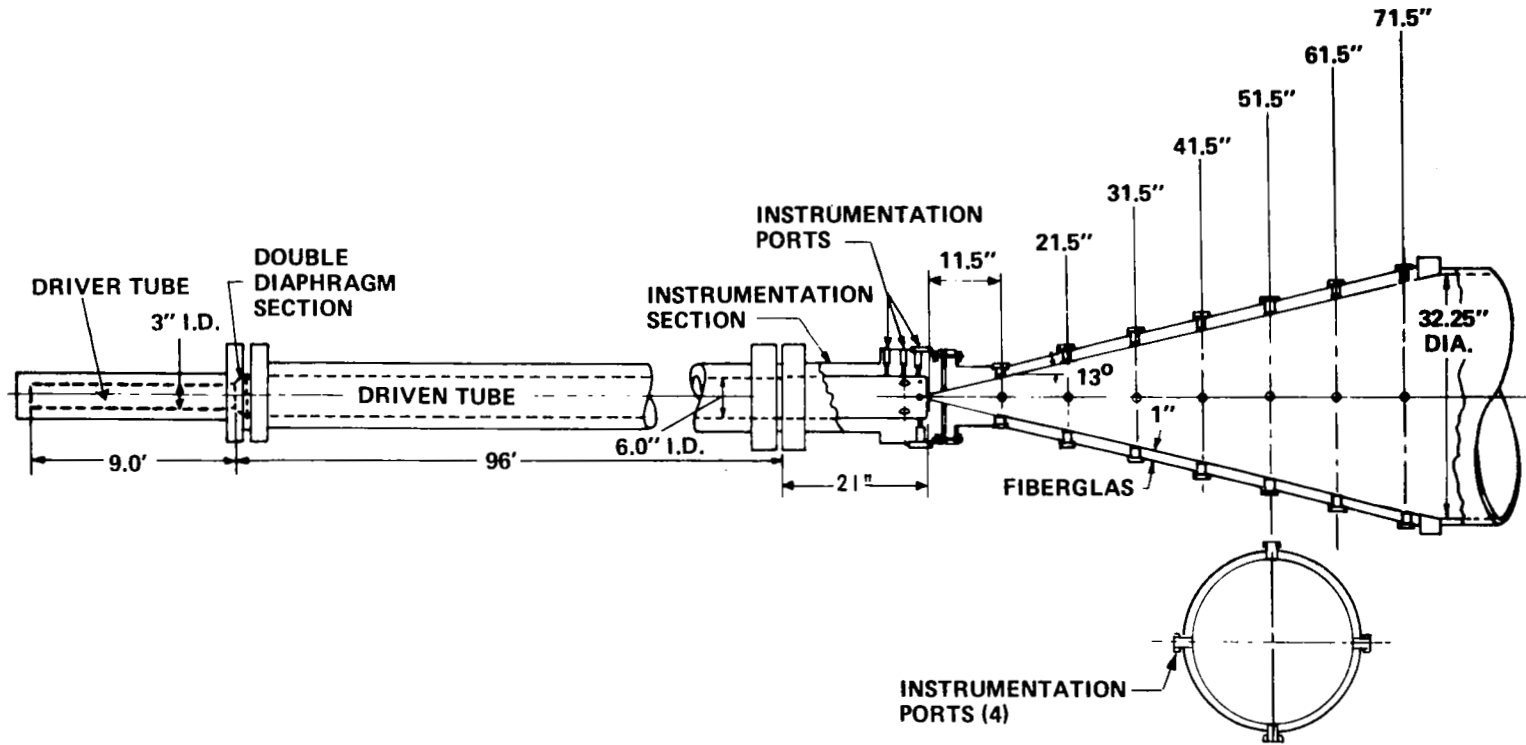
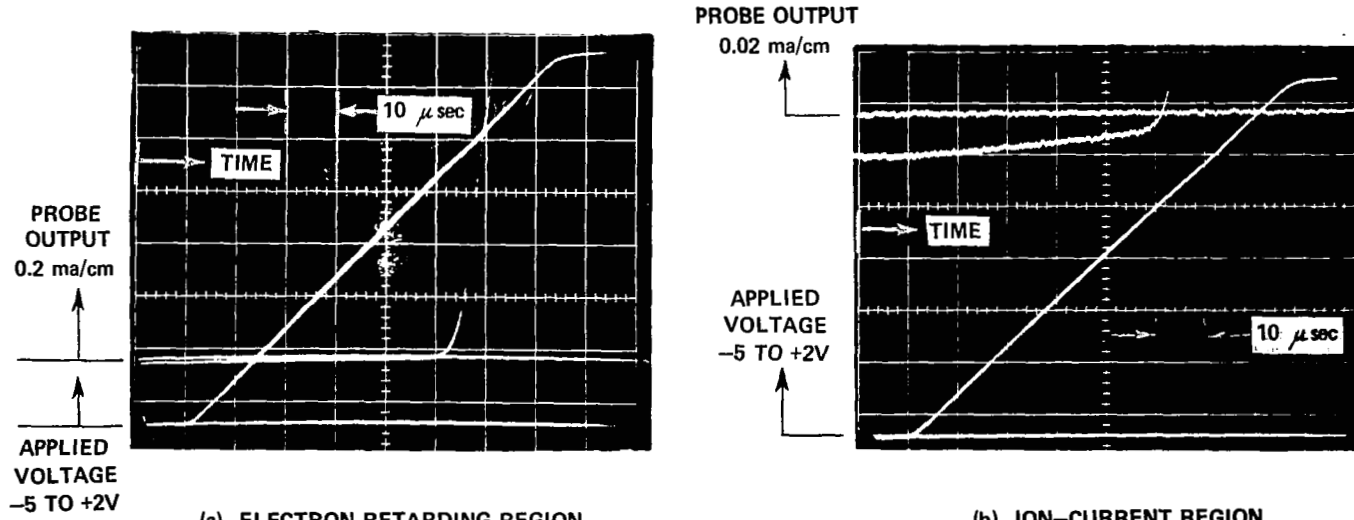


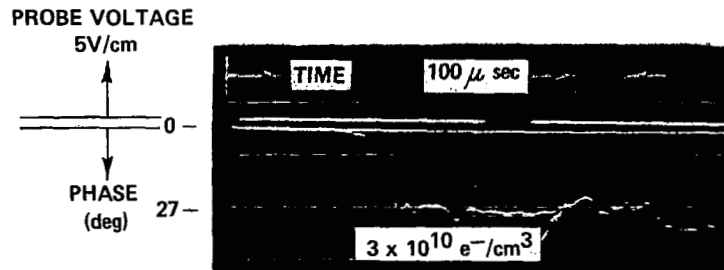
Figure 1 SCHEMATIC OF EXPERIMENTAL APPARATUS

REFLECTED-SHOCK TEMPERATURE: 6260 °K  
 REFLECTED-SHOCK PRESSURE: 10.0 atm



(a) ELECTRON RETARDING REGION

(b) ION-CURRENT REGION



(c) 17 GHz MICROWAVE INTERFEROMETER DATA

Figure 2 TYPICAL PROBE CHARACTERISTICS AND MICROWAVE-INTERFEROMETER DATA IN CARBON MONOXIDE PLASMA AT 32.5 in. FROM THE NOZZLE THROAT

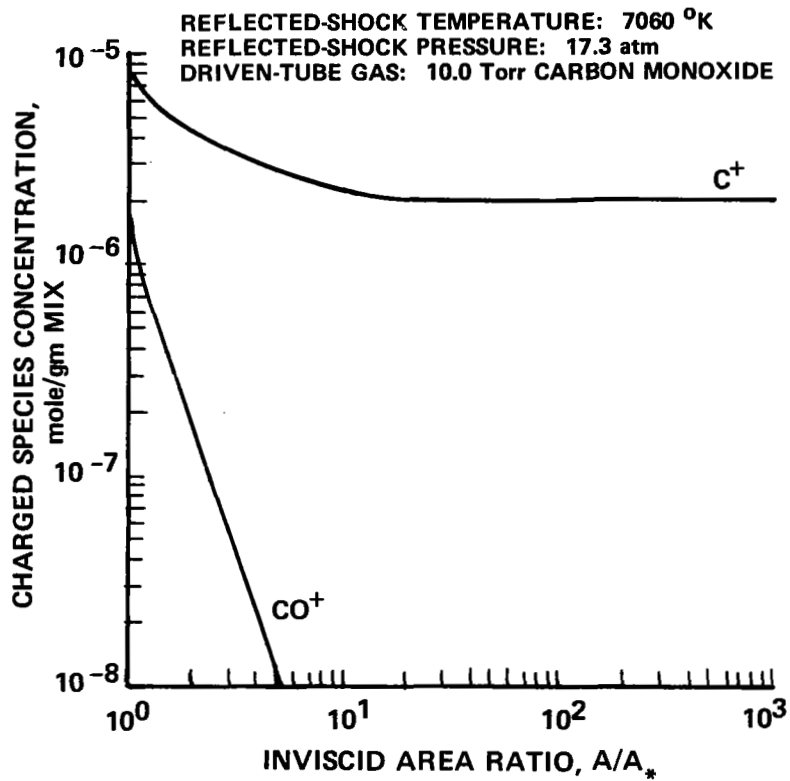


Figure 3(a) ION-SPECIES DISTRIBUTION  
 IN NOZZLE FLOW

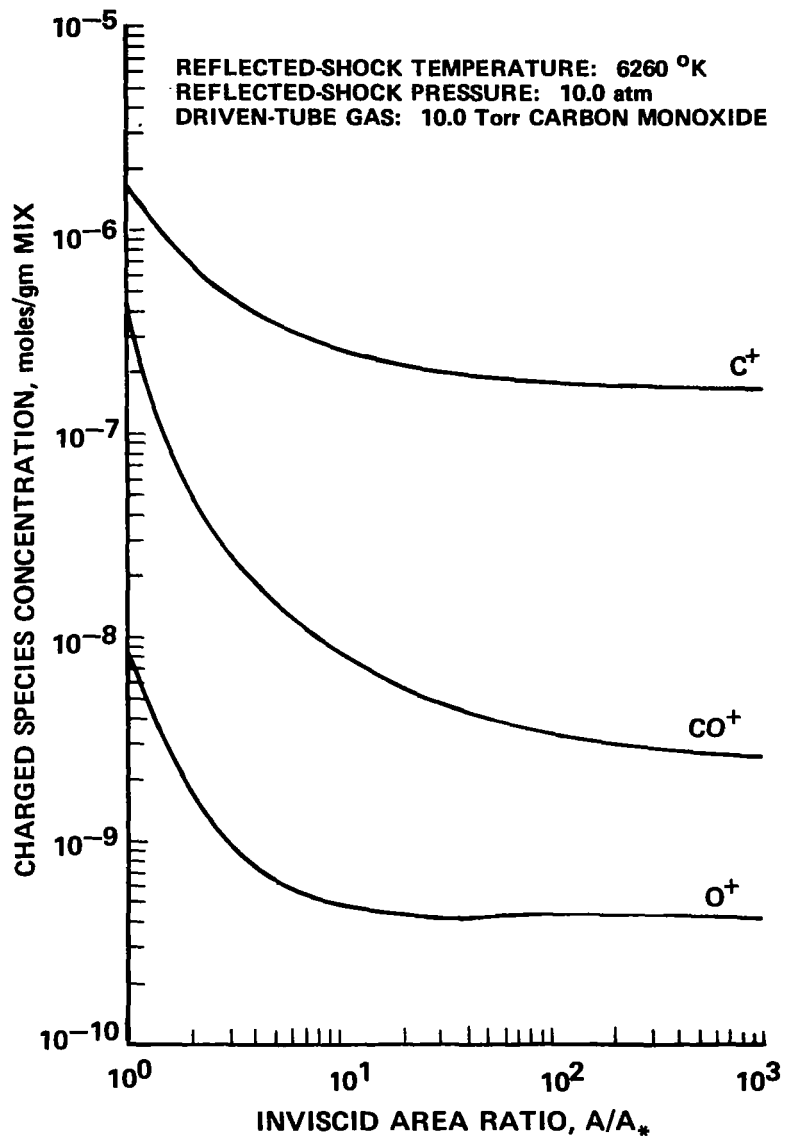


Figure 3(b) ION-SPECIES DISTRIBUTION  
 IN NOZZLE FLOW

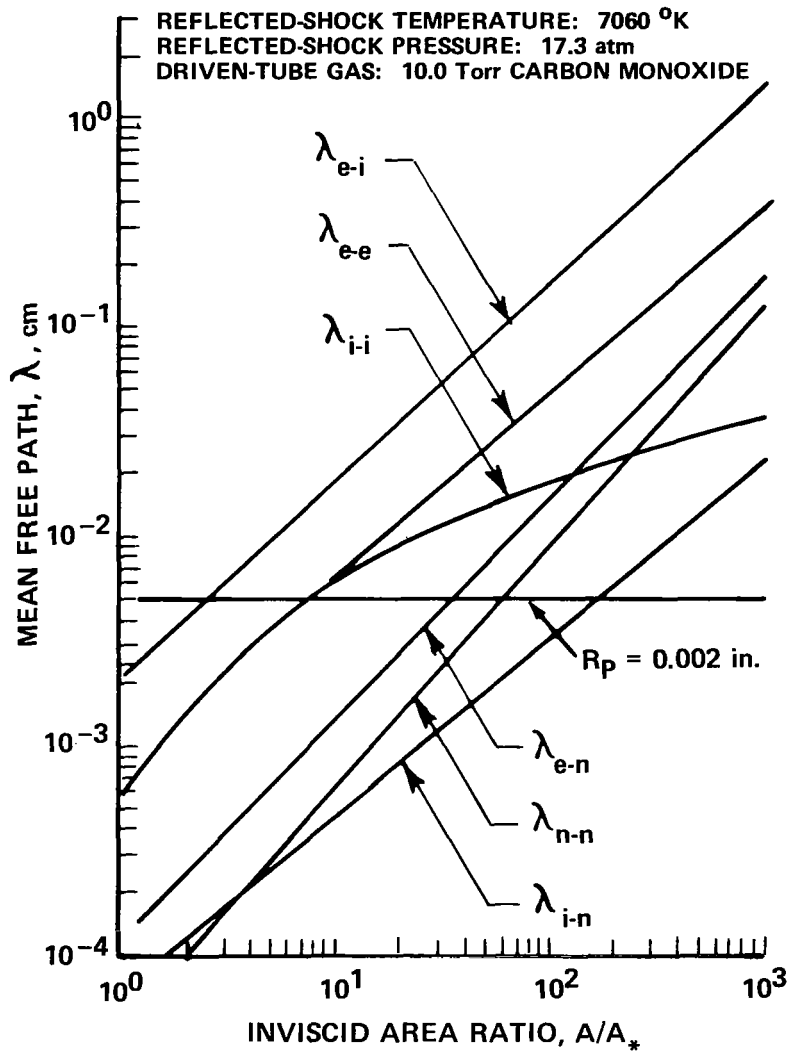


Figure 4 CALCULATED MEAN FREE PATHS IN CARBON MONOXIDE PLASMA

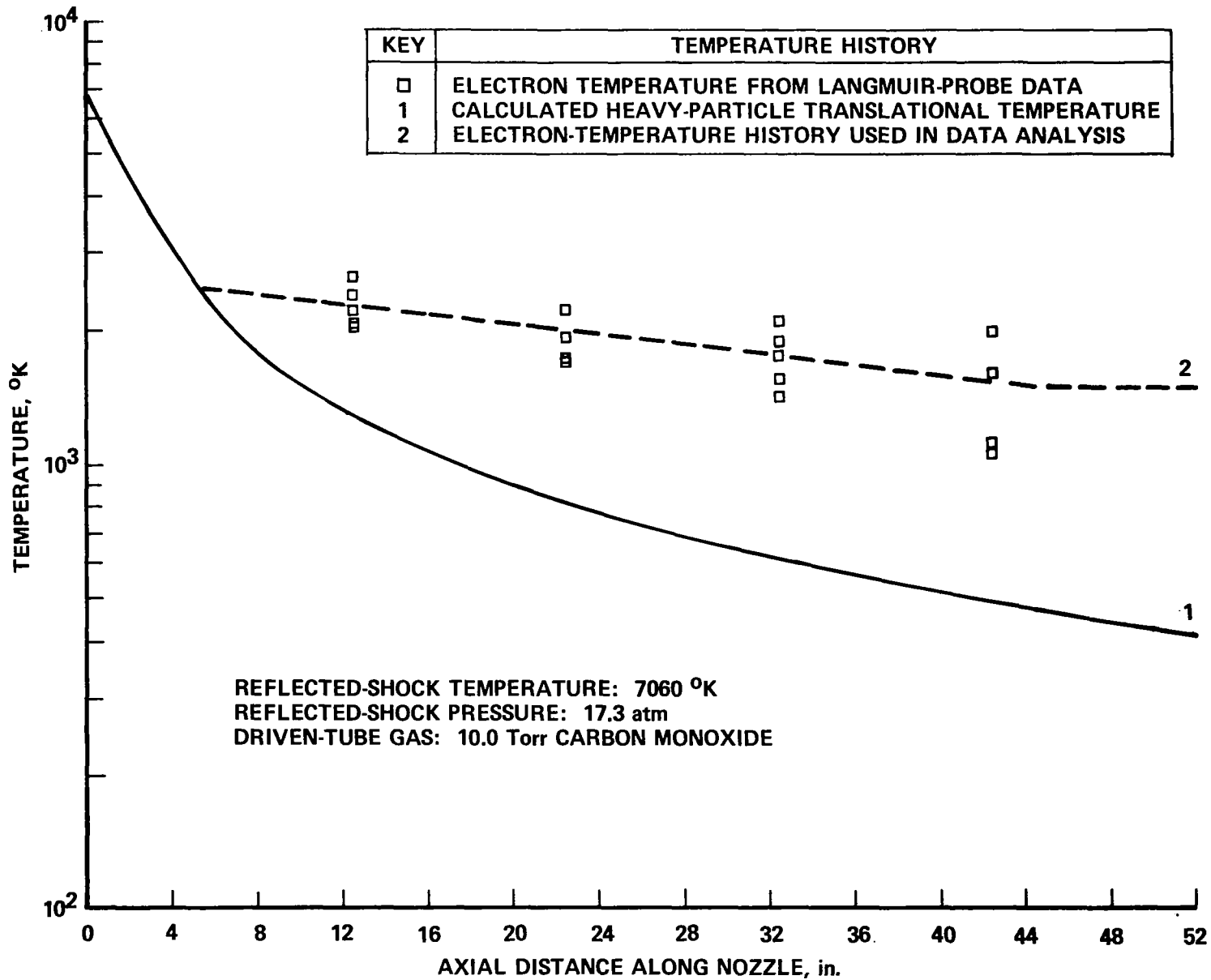
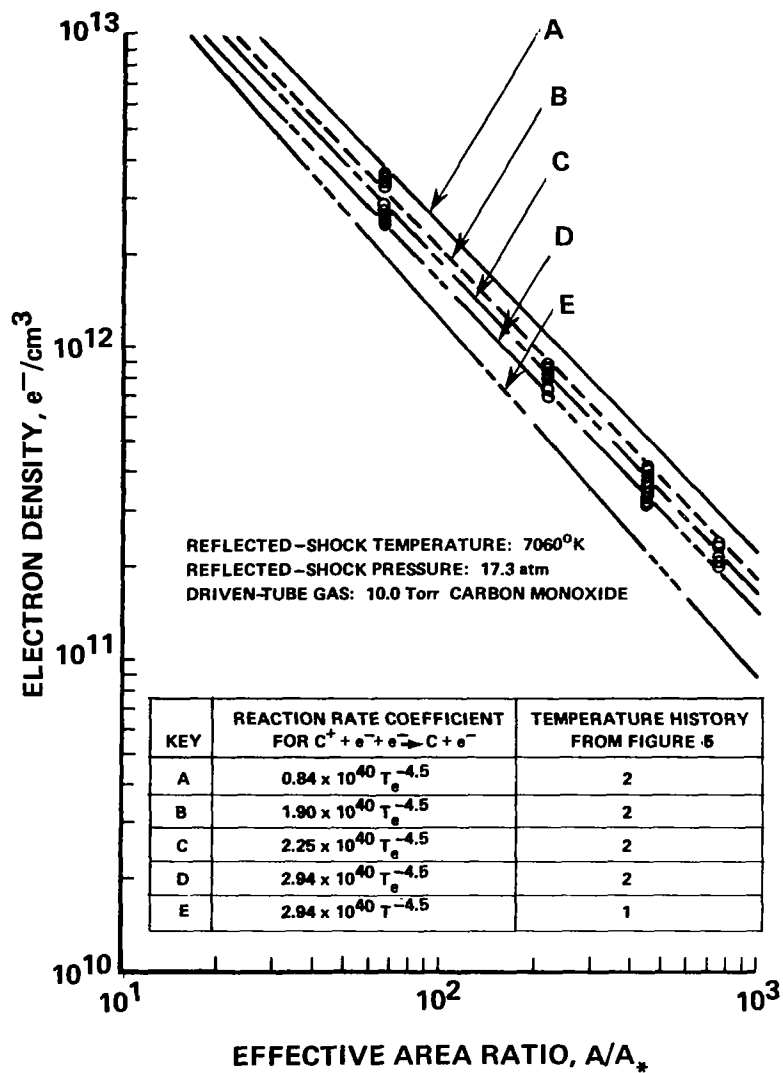
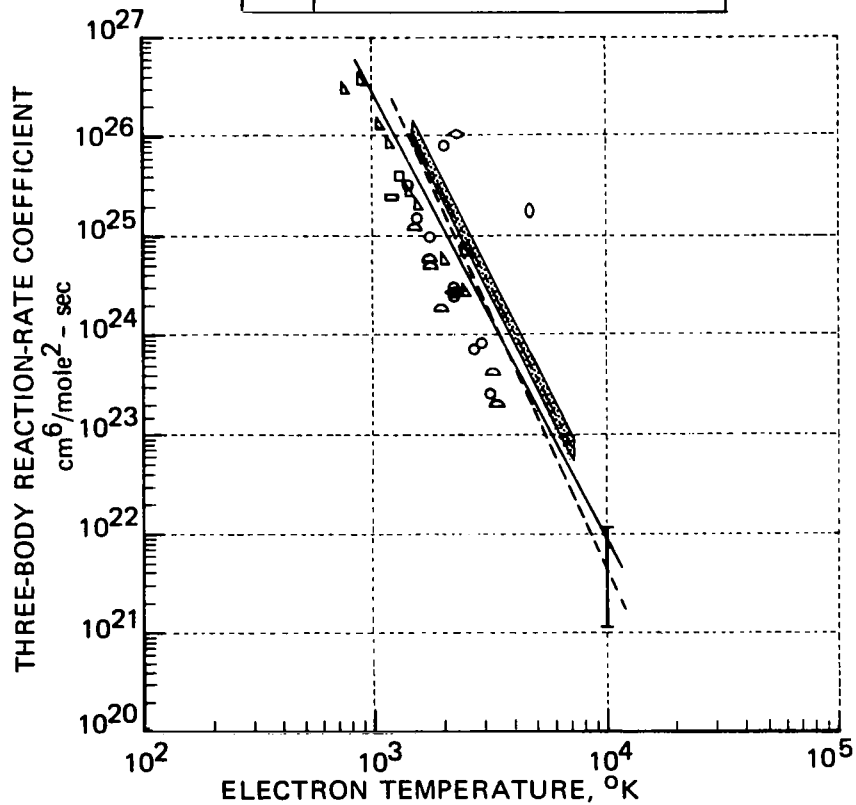


Figure 5 MEASURED ELECTRON TEMPERATURE IN EXPANDING CARBON MONOXIDE PLASMA



**Figure 6 ELECTRON-DENSITY DISTRIBUTION IN EXPANDING CARBON MONOXIDE PLASMA**

KEY	AUTHOR, TEST GAS, REFERENCE
$\left. \begin{array}{c} \circ \\ \square \\ \diamond \end{array} \right\}$	BYRON, STABLER, AND BORTZ (ARGON, CESIUM, MERCURY), 10
$\circ$	HINNOV AND HIRSHBERG (HELIUM), 8
$\square$	HINNOV AND HIRSCHBERG (HYDROGEN), 8
$\triangle$	MOTLEY AND KUCKES (HELIUM), 9
$\diamond$	ALESKOVSKI (CESIUM), 14
D	ROBBEN, KUNKEL, and TALBOT (HELIUM), 15
I	PARK (NITROGEN), 16
—	MAKIN AND KECK, $k_r = 8.34 \times 10^{39} T_e^{-4.5}$ , 4
- - -	PARK, $k_r = 4.17 \times 10^{21} (T/10,000)^{-5.27}$ , 17
▨	EXPERIMENTAL DATA OF THIS PAPER (CARBON)



**Figure 7 REACTION-RATE-COEFFICIENT DATA AND THEORY FOR THE REACTION**  
 $M^+ + e^- + e^- \rightarrow M + e^-$

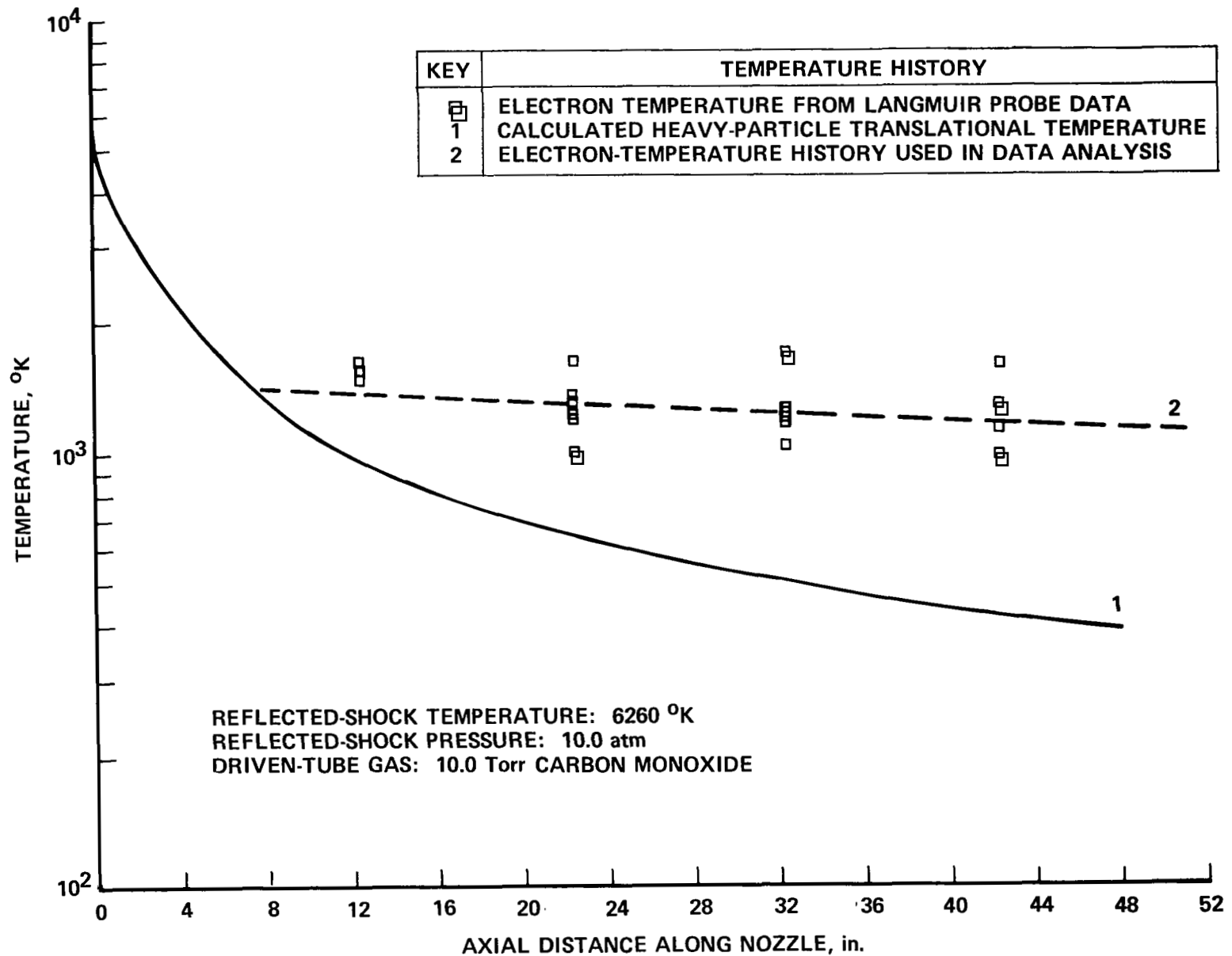
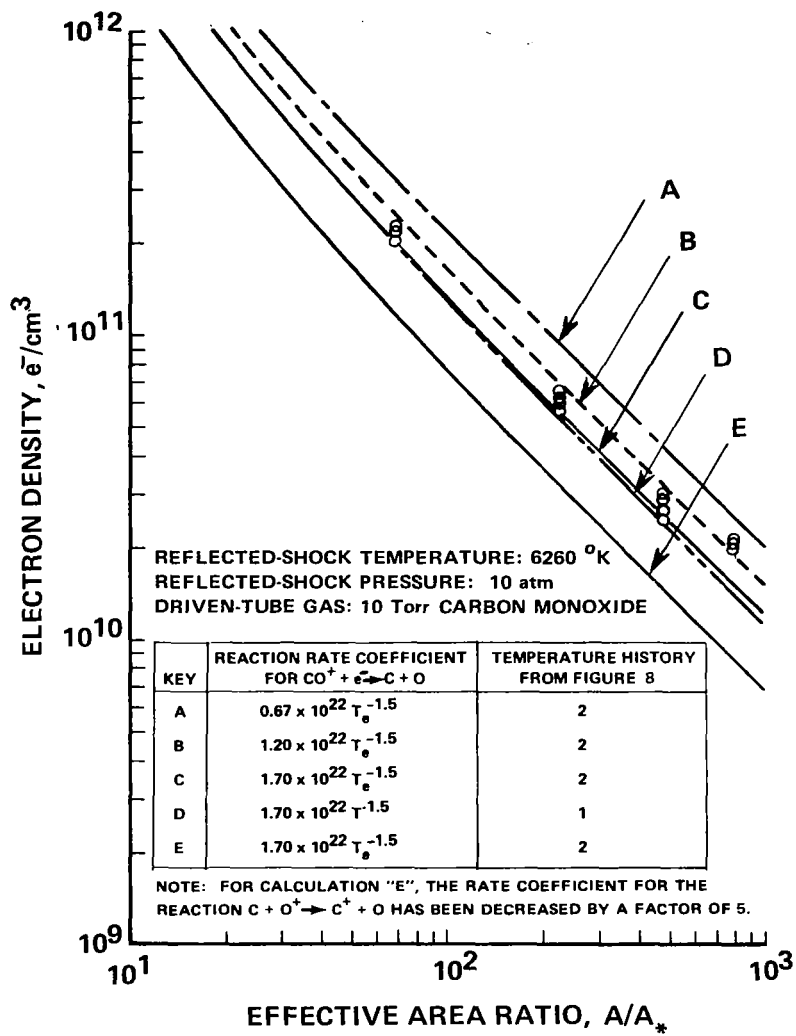


Figure 8 MEASURED ELECTRON TEMPERATURE IN EXPANDING CARBON MONOXIDE PLASMA



**Figure 9 ELECTRON DENSITY DISTRIBUTION IN EXPANDING CARBON MONOXIDE PLASMA**

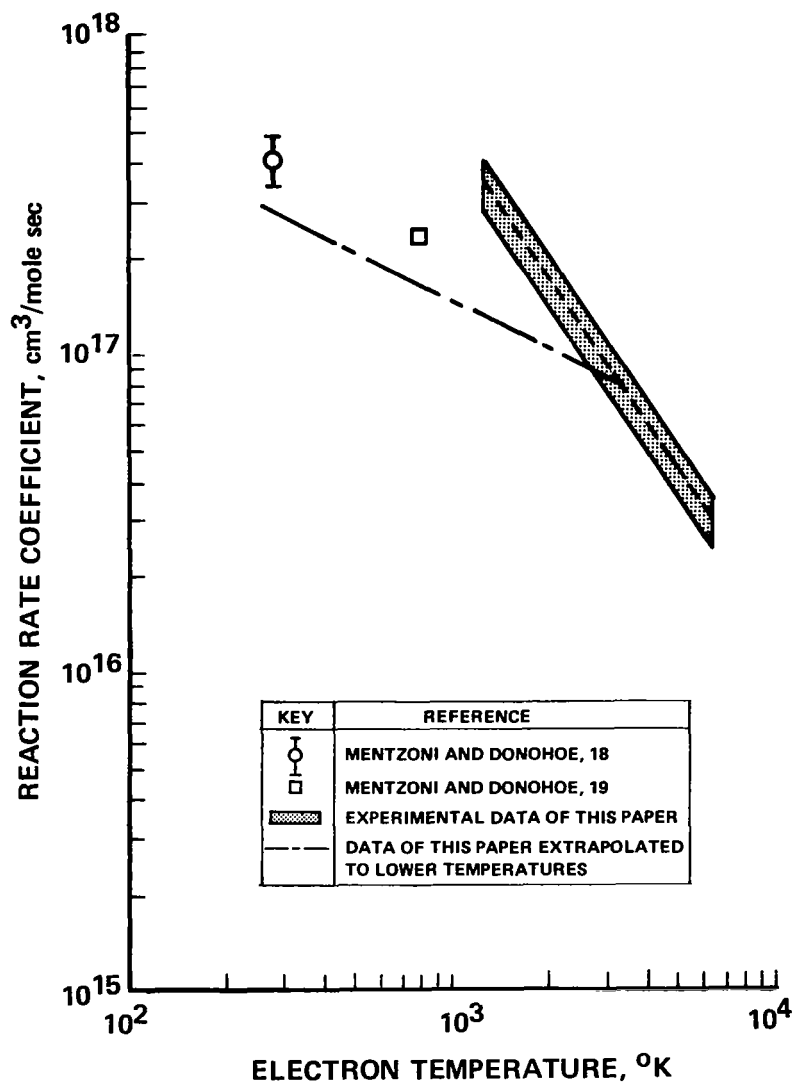


Figure 10 REACTION RATE COEFFICIENT DATA FOR THE REACTION  $\text{CO}^+ + e^- \rightarrow \text{C} + \text{O}$

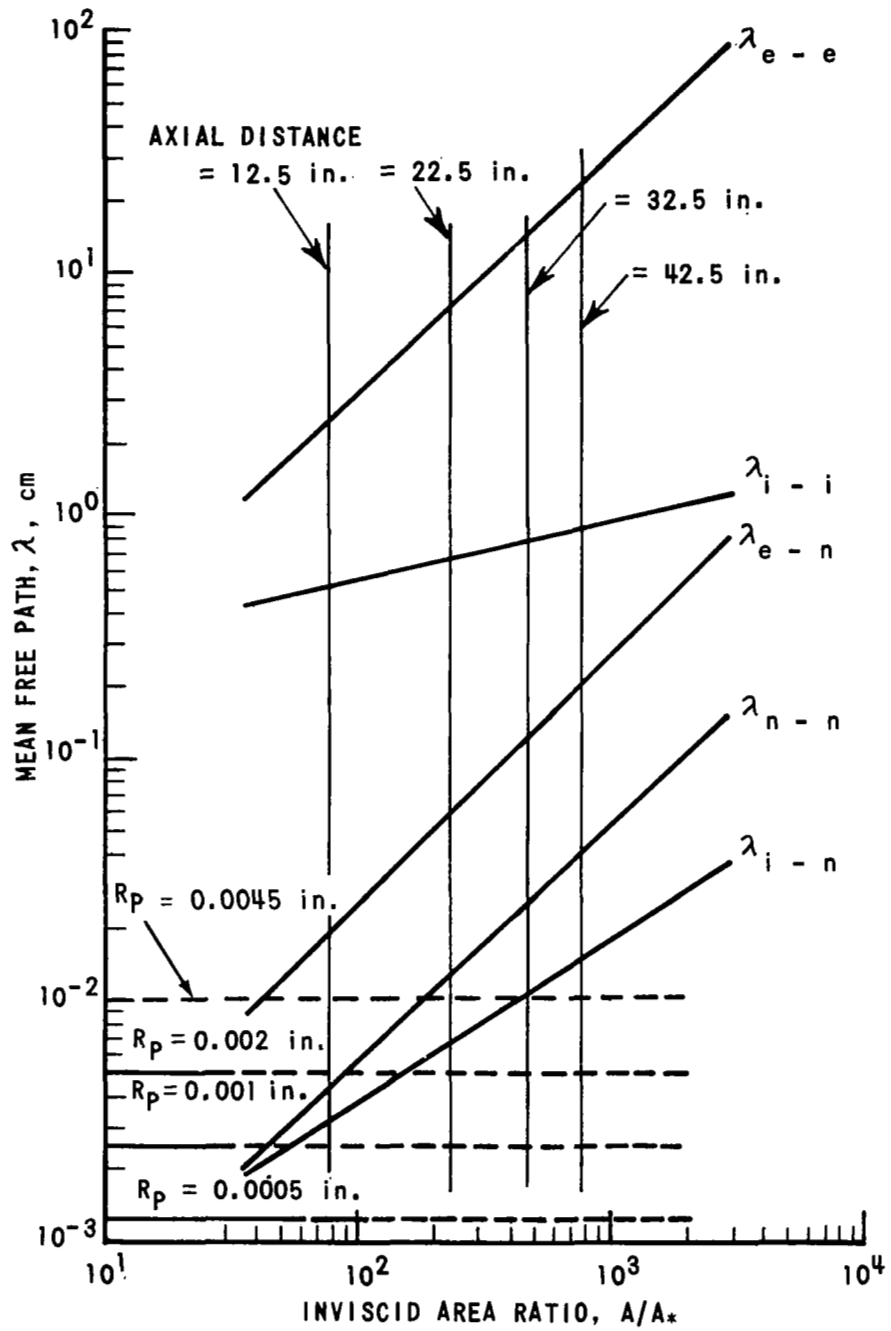
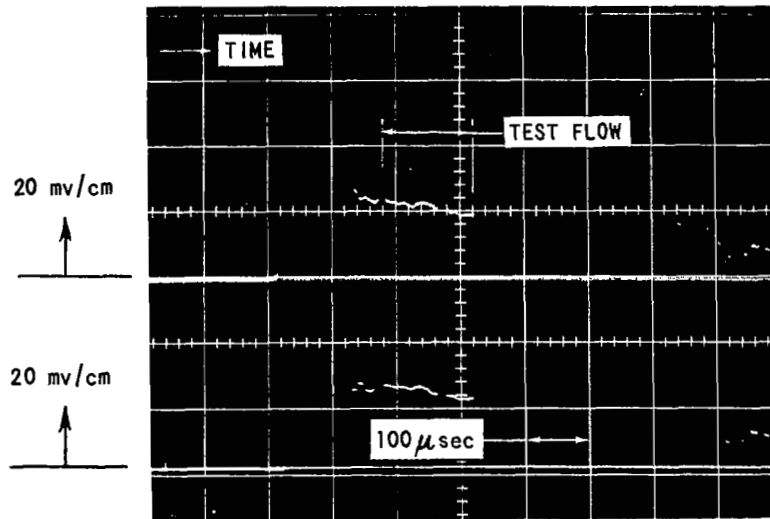
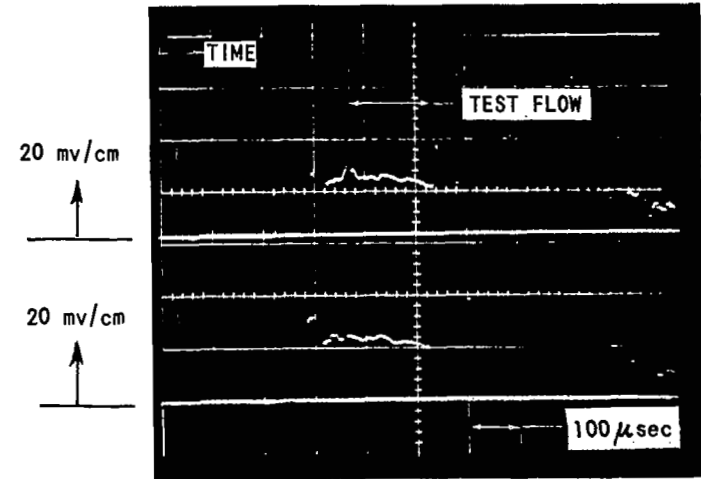


Figure 11 CALCULATED MEAN FREE PATHS IN EXPANDING NITROGEN FLOW



(a) WEDGE-PROBE OUTPUT AT 32.5 in.  
 FROM THROAT: UPPER - PROBE NO. 4  
 LOWER - PROBE NO. 5  
 BIAS VOLTAGE: -5.0 volts  
 RESISTOR: 1000 ohms

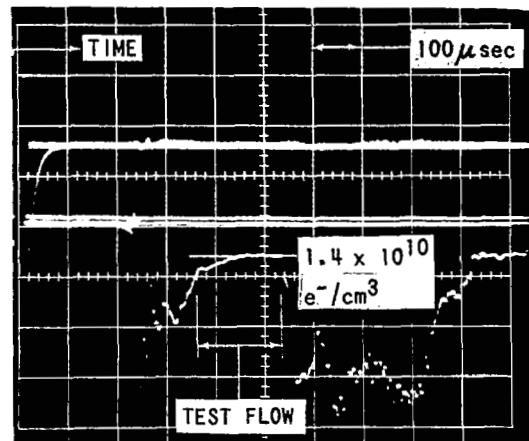


(b) WEDGE-PROBE OUTPUT AT 32.5 in.  
 FROM THROAT: UPPER - PROBE NO. 7  
 LOWER - PROBE NO. 8  
 BIAS VOLTAGE: -5.0 volts  
 RESISTOR: 1000 ohms

ATTENUATION  
 (dB)



PHASE  
 (deg)



(c) 17 GHz MICROWAVE INTERFEROMETER  
 OUTPUT AT 31.5 in. FROM THROAT

Figure 12 TYPICAL WEDGE-PROBE AND MICROWAVE INTERFEROMETER DATA IN A NITROGEN PLASMA

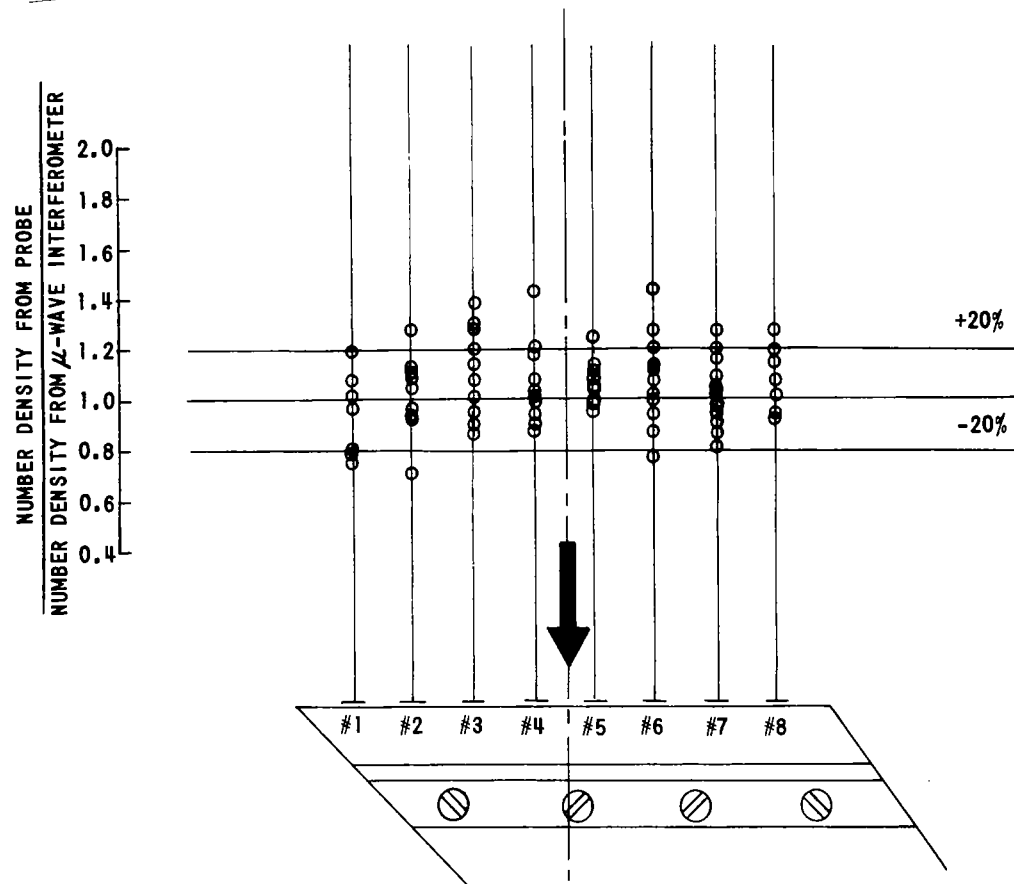


Figure 13 WEDGE-PROBE RESULTS OBTAINED IN INVISCID FLOW AT 32.5 inches FROM NOZZLE THROAT

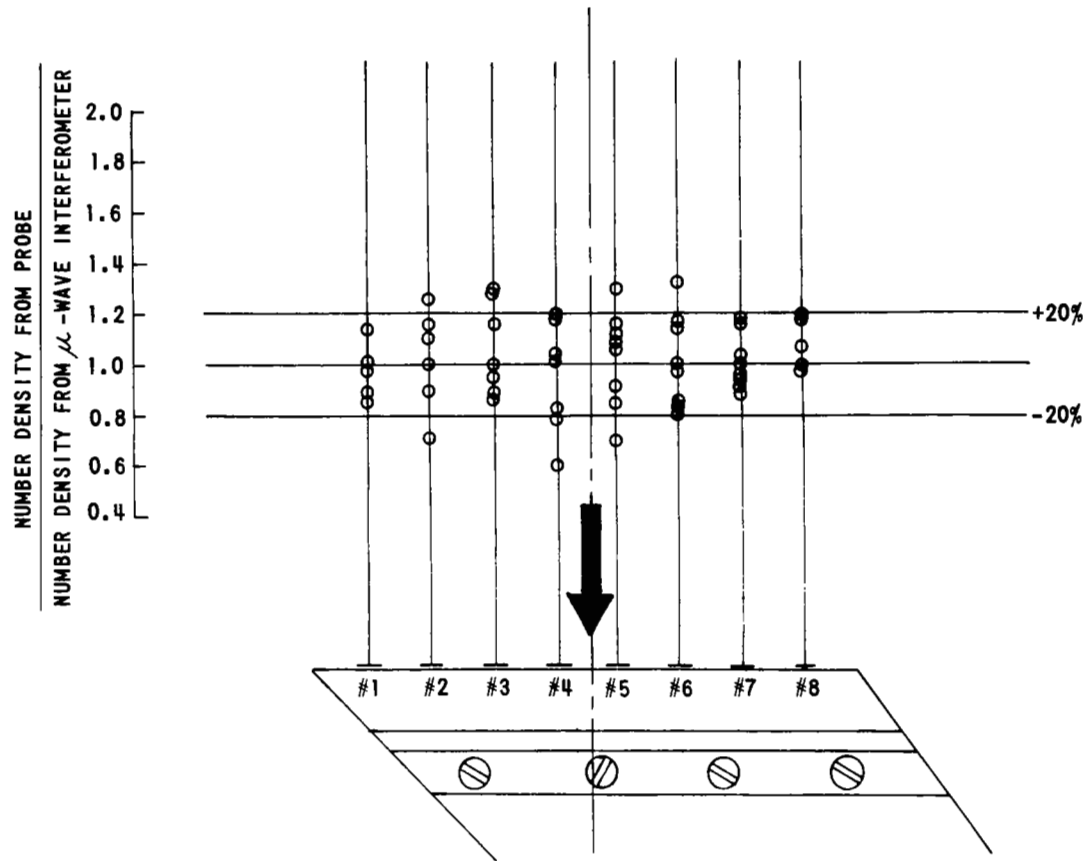


Figure 14 WEDGE-PROBE RESULTS OBTAINED IN INVISCID FLOW AT 42.5 inches FROM THE THROAT

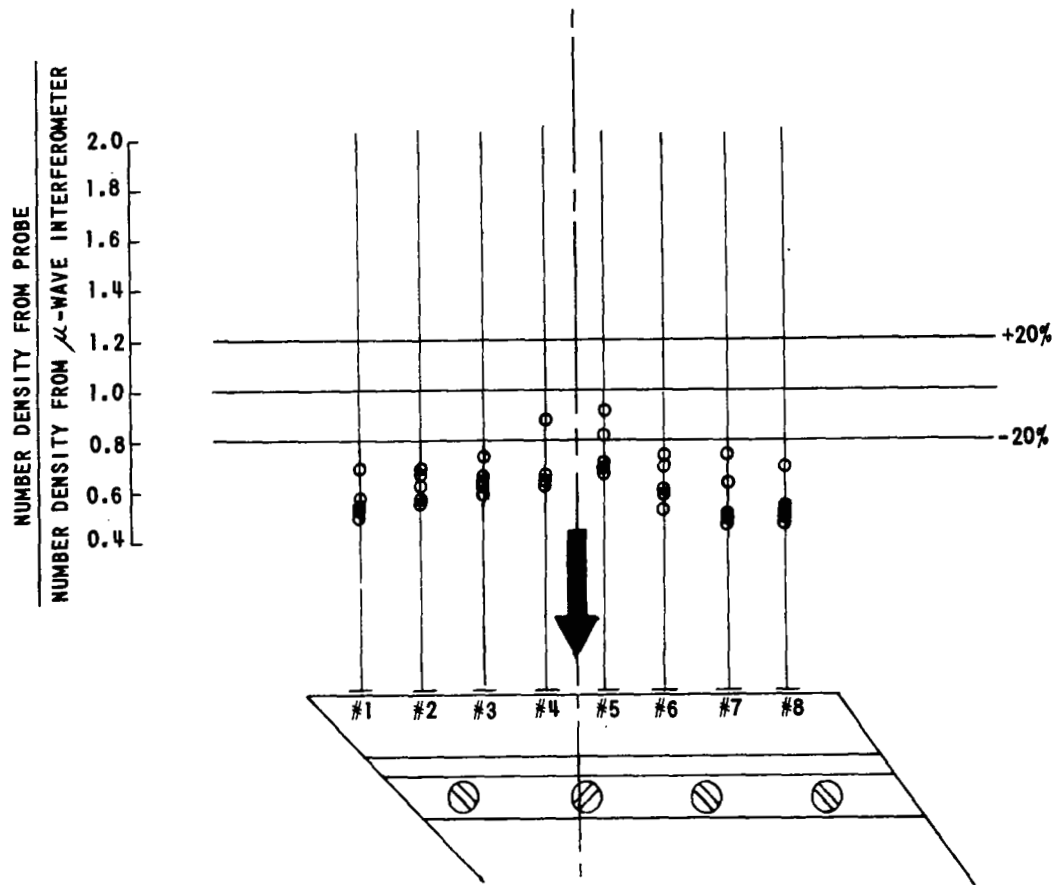


Figure 15 WEDGE-PROBE RESULTS OBTAINED IN INVISCID FLOW AT 14.5 inches FROM THE THROAT

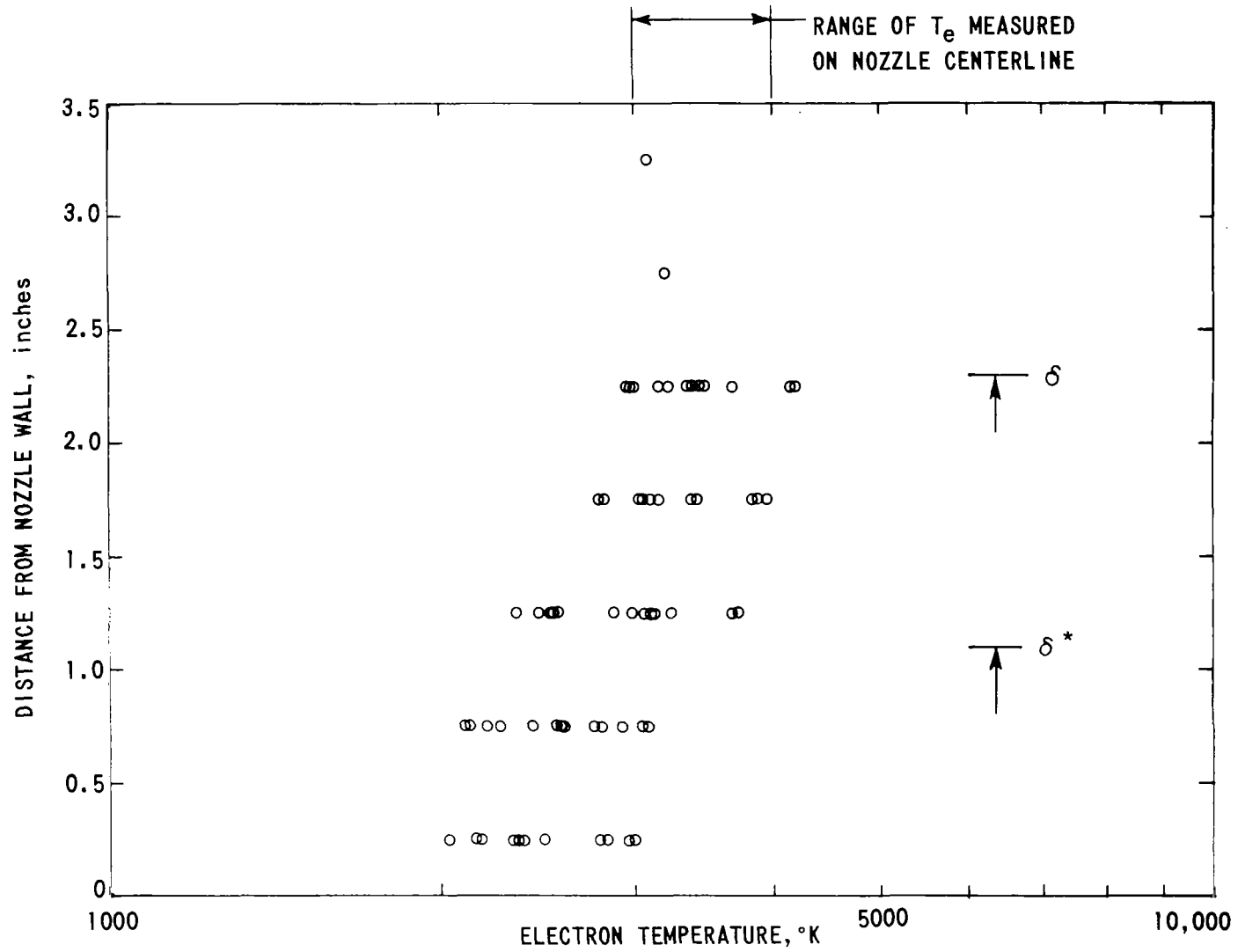


Figure 16 ELECTRON-TEMPERATURE DISTRIBUTION MEASURED IN NOZZLE BOUNDARY LAYER

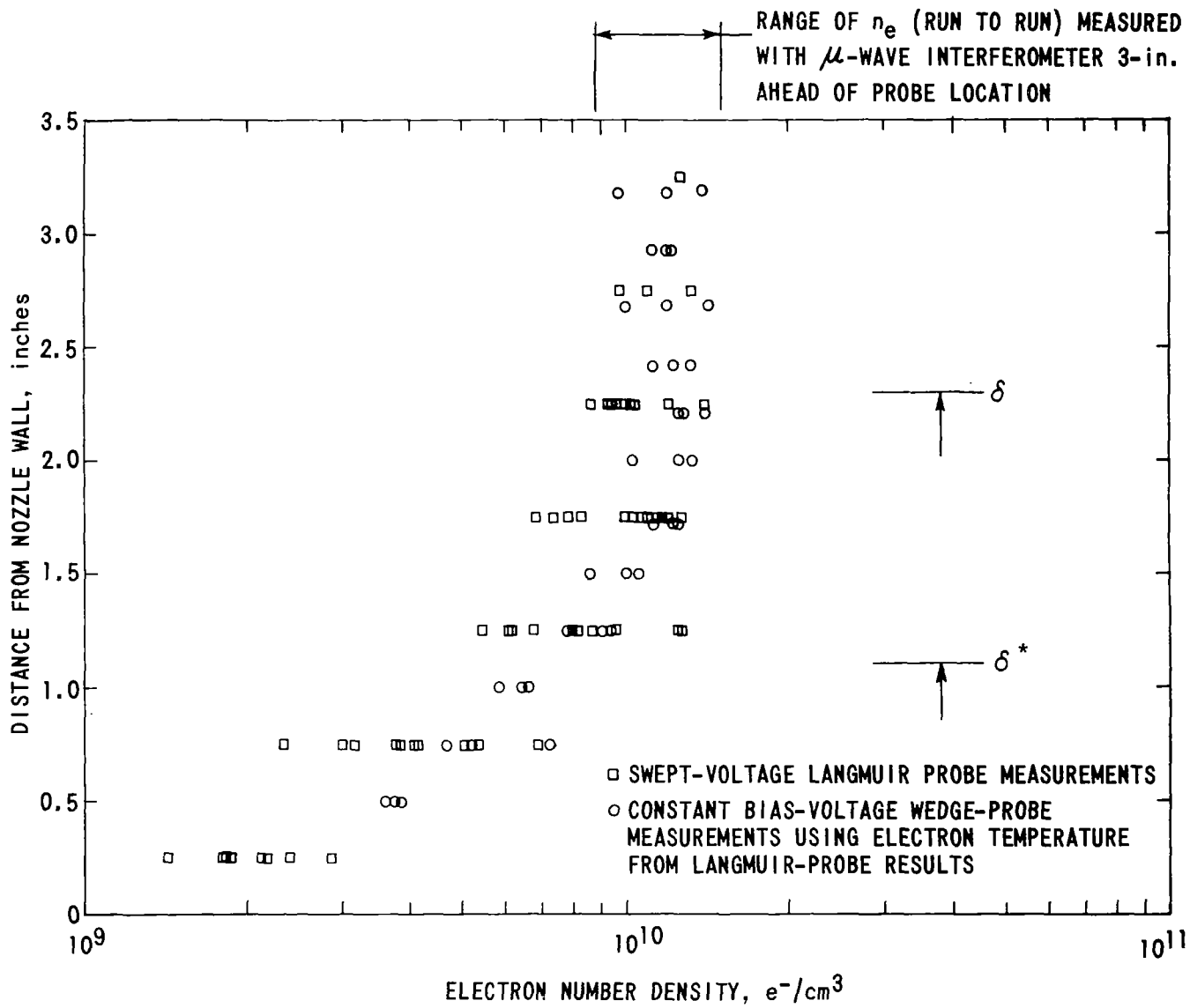


Figure 17 ELECTRON-DENSITY DISTRIBUTION MEASURED IN NOZZLE-WALL BOUNDARY LAYER

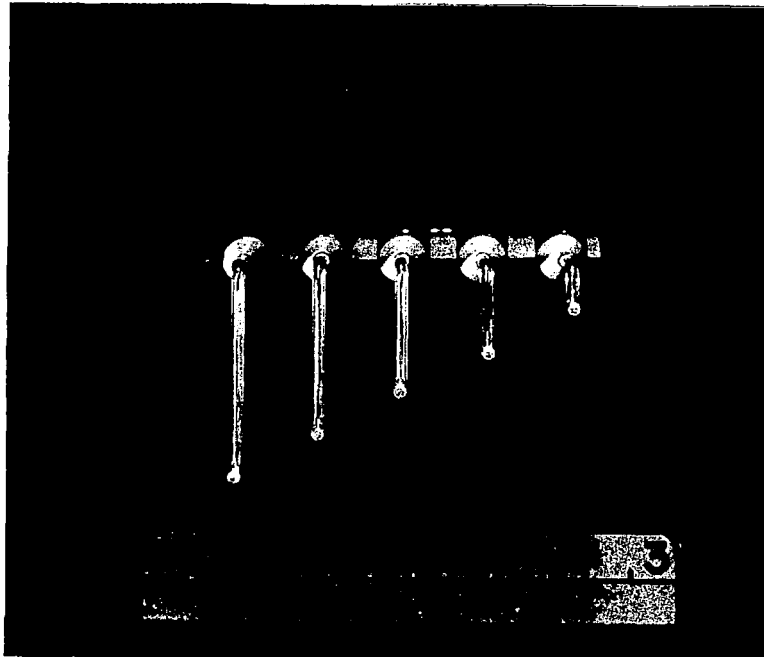
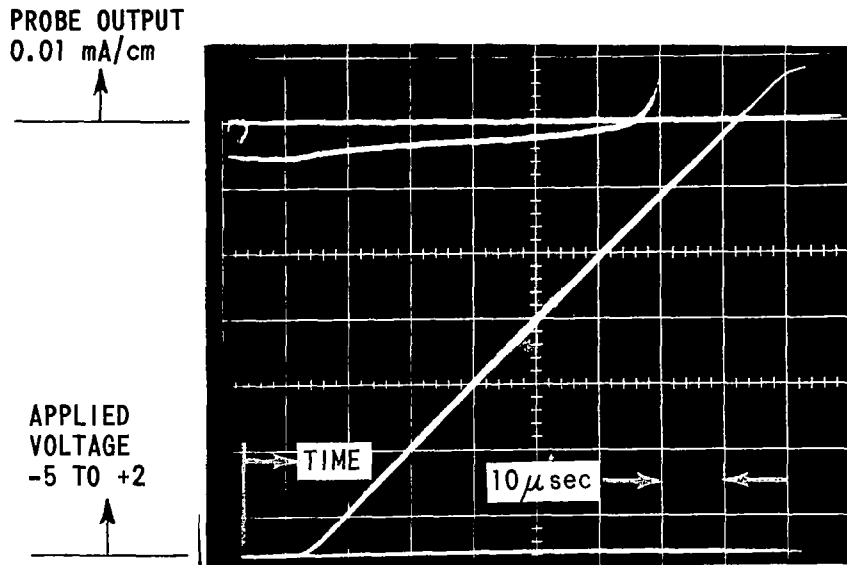
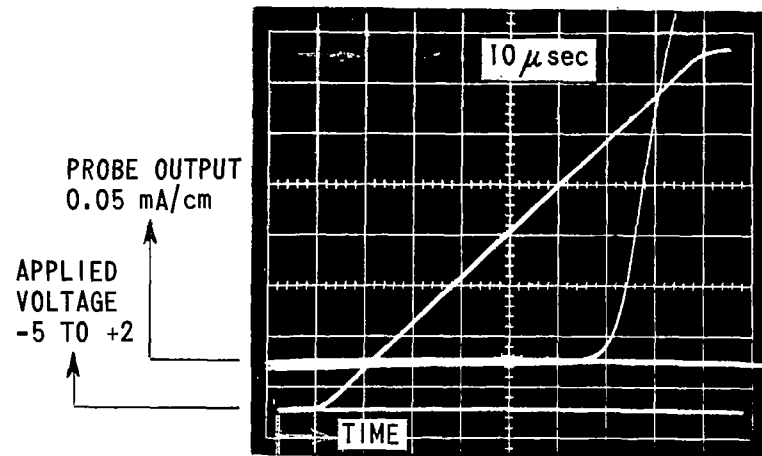


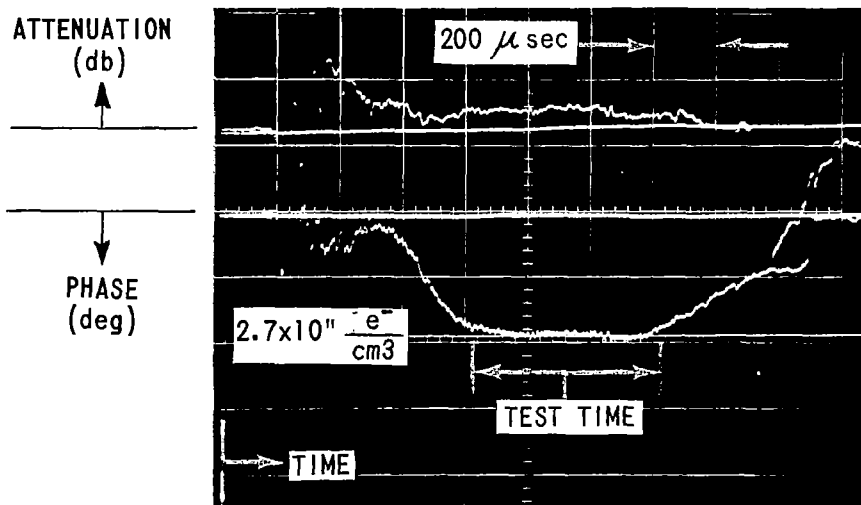
Figure 18 PROBE RAKE FOR BOUNDARY-LAYER PROBING



(a) ION-CURRENT REGION OBTAINED AT 0.060 in. FROM PLATE SURFACE AT 6.75 in. FROM LEADING EDGE



(b) ELECTRON-RETARDING AND ELECTRON-CURRENT REGIONS OBTAINED AT 0.060 in. FROM PLATE SURFACE AT 6.75 in. FROM LEADING EDGE



(c) 17 GHz MICROWAVE INTERFEROMETER OBTAINED AT 21.5 in. FROM THROAT

REFLECTED-SHOCK TEMPERATURE: 12,150 °K  
 REFLECTED-SHOCK PRESSURE: 30.1 atm  
 DRIVEN-TUBE GAS: ARGON + 0.12% N<sub>2</sub>

Figure 19 TYPICAL PROBE CHARACTERISTIC AND MICROWAVE-INTERFEROMETER DATA IN ARGON-NITROGEN PLASMA

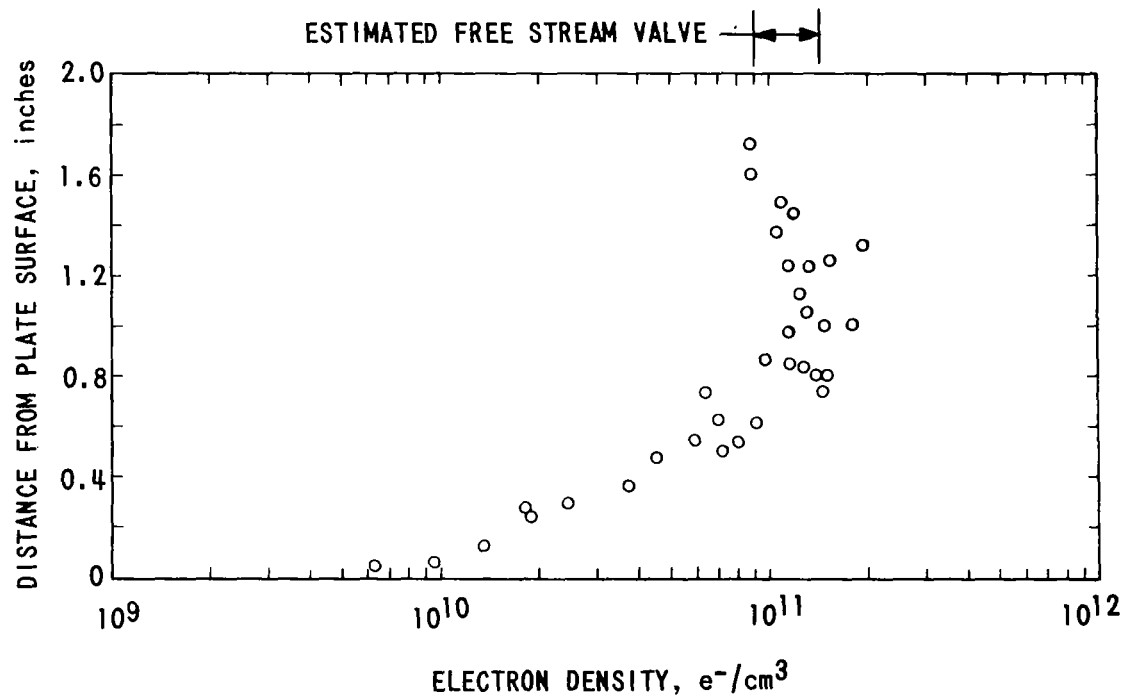


Figure 20 ELECTRON NUMBER DENSITY ABOVE PLATE AT  
6.75 inches FROM LEADING EDGE

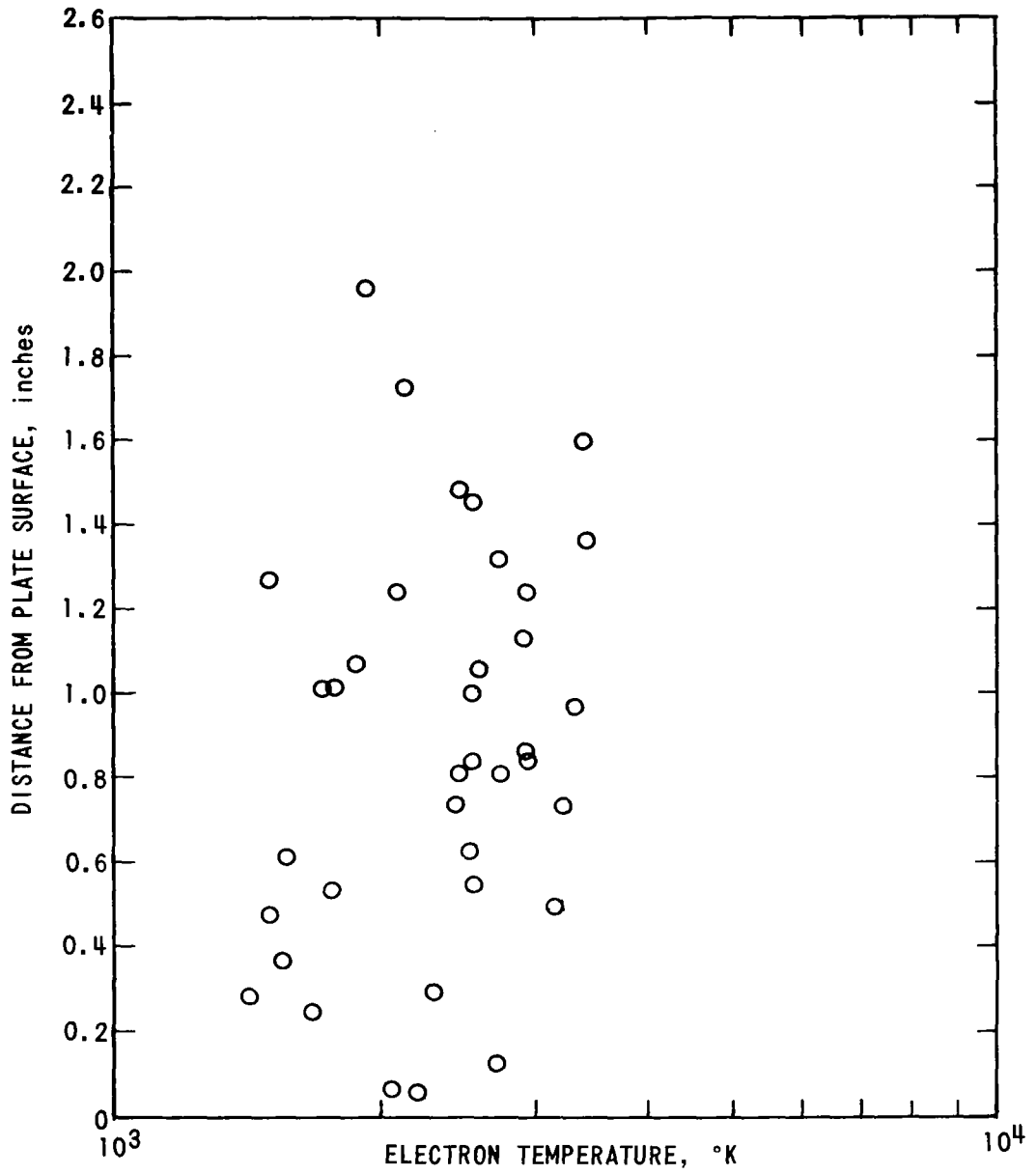


Figure 21 ELECTRON TEMPERATURE ABOVE PLATE AT  
6.75 inches FROM LEADING EDGE

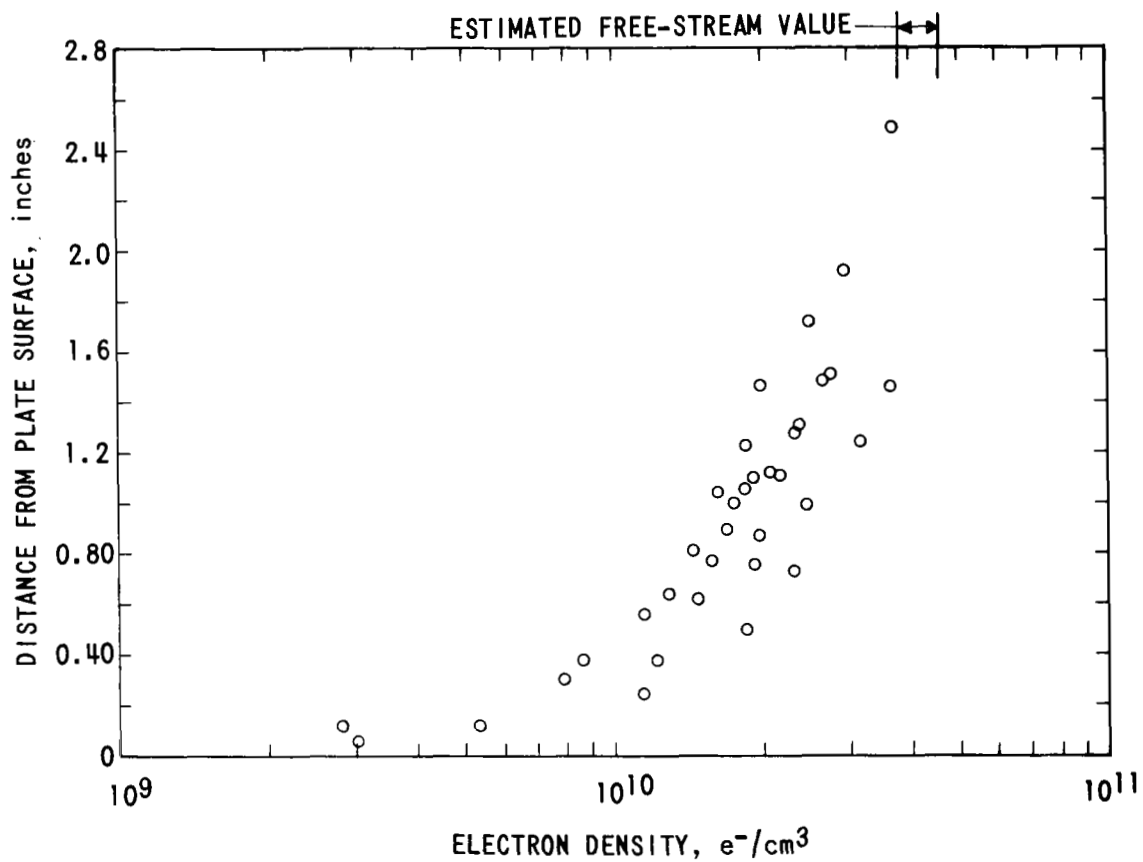


Figure 22 ELECTRON NUMBER DENSITY ABOVE PLATE AT  
19.25 inches FROM LEADING EDGE

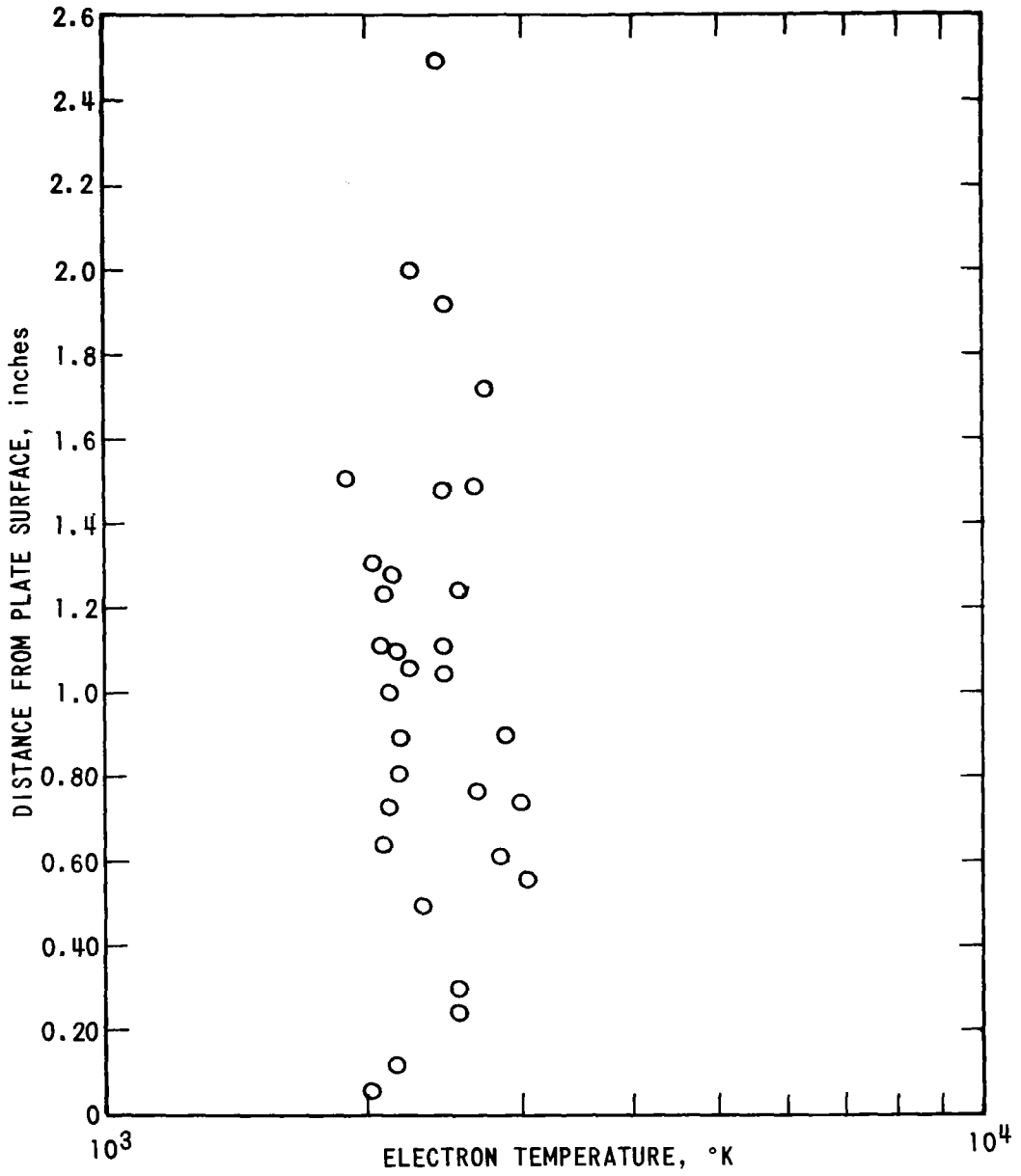


Figure 23 ELECTRON TEMPERATURE ABOVE PLATE AT  
19.25 inches FROM LEADING EDGE

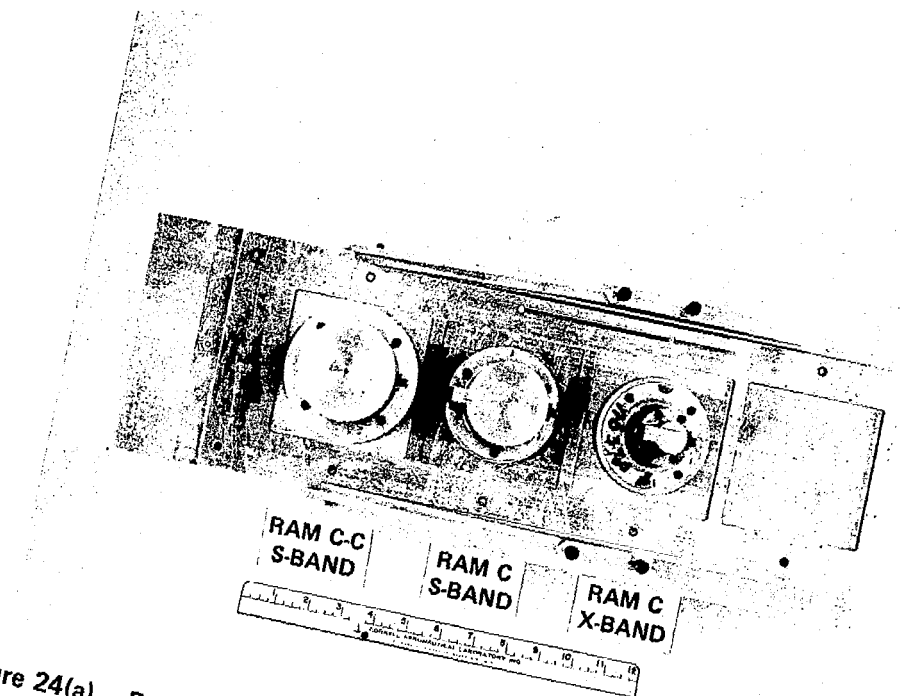


Figure 24(a) RAM C-C AND RAM C S-BAND AND X-BAND ANTENNAS MOUNTED IN FLAT PLATE

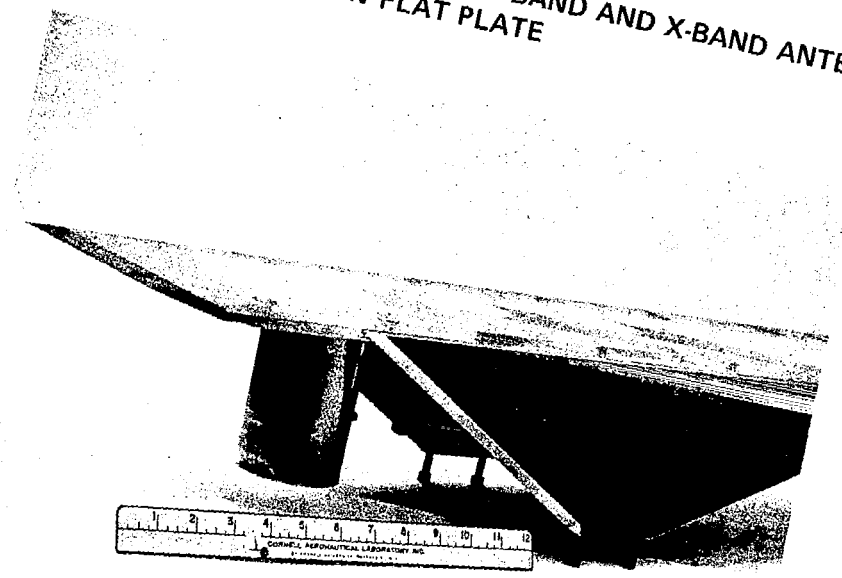


Figure 24(b) RAM C-C AND RAM C ANTENNAS IN FLAT-PLATE MODEL

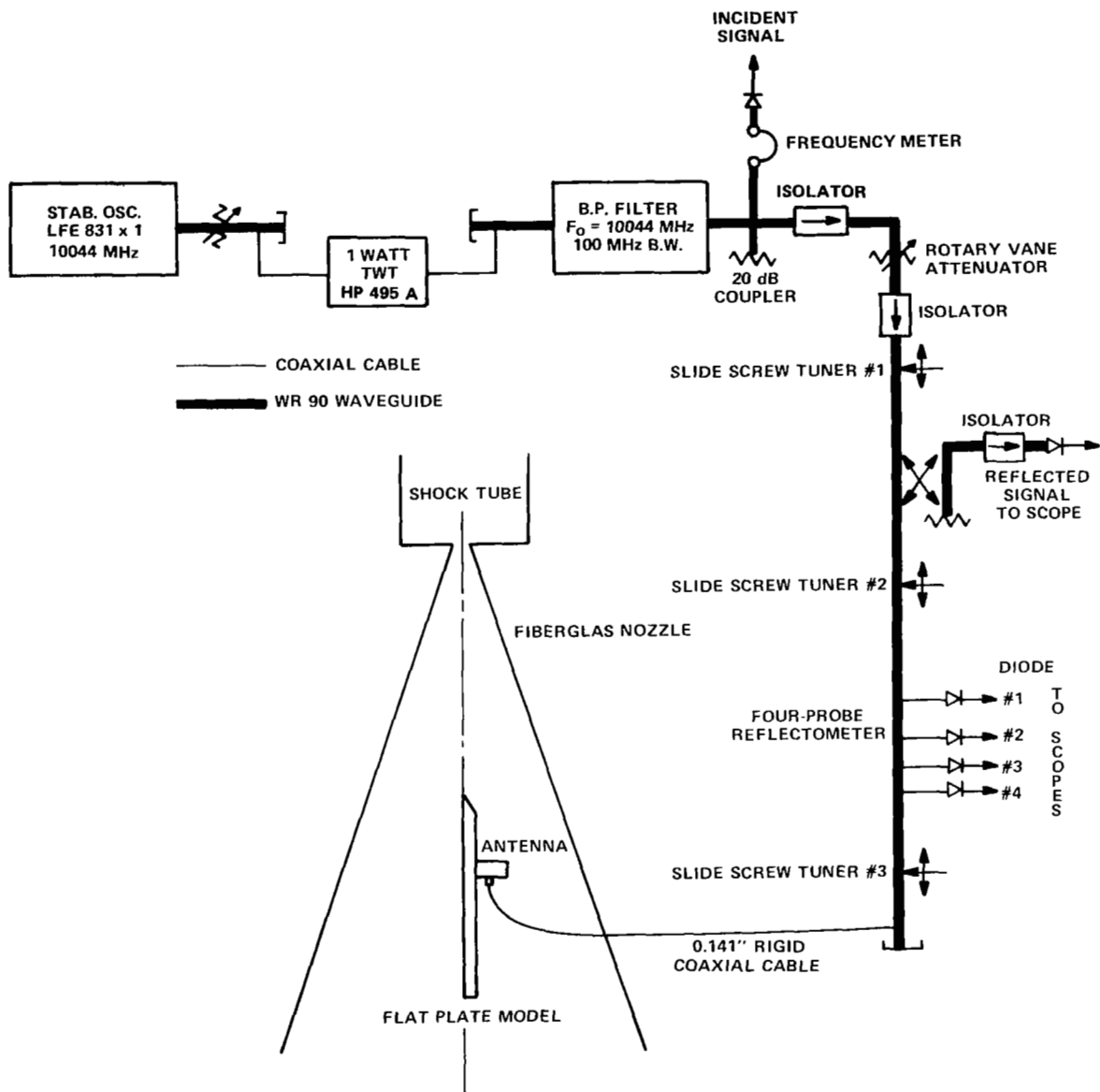


Figure 25 SCHEMATIC DIAGRAM OF FOUR-PROBE X-BAND REFLECTOMETER

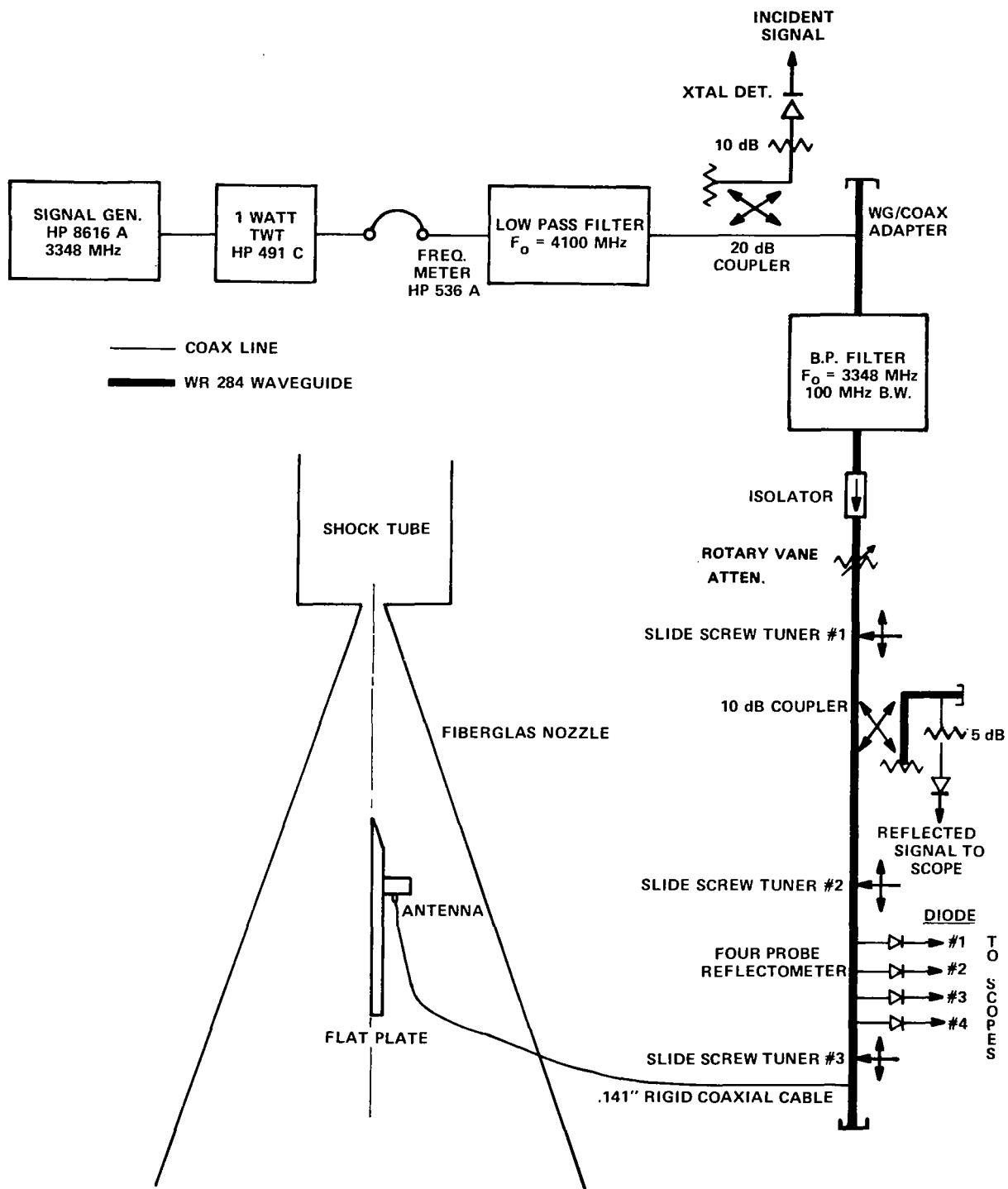
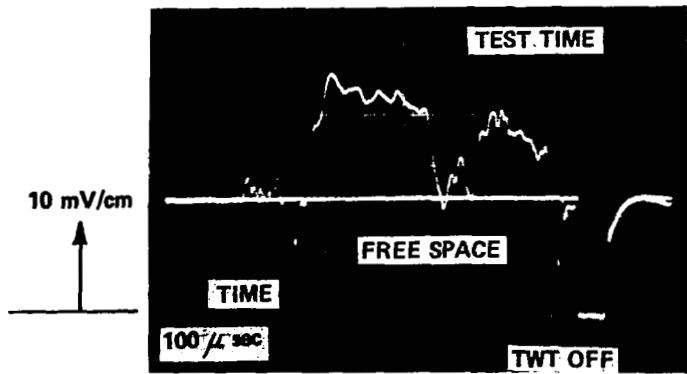
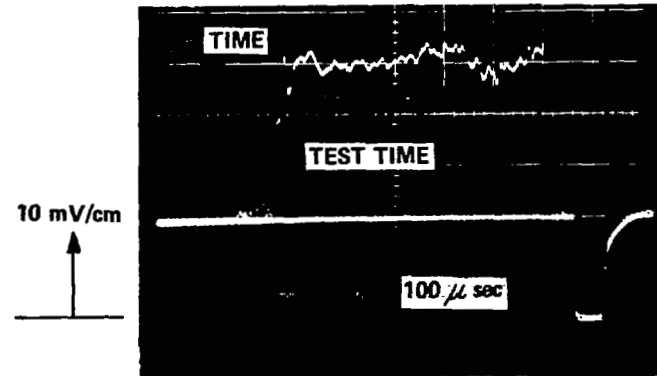


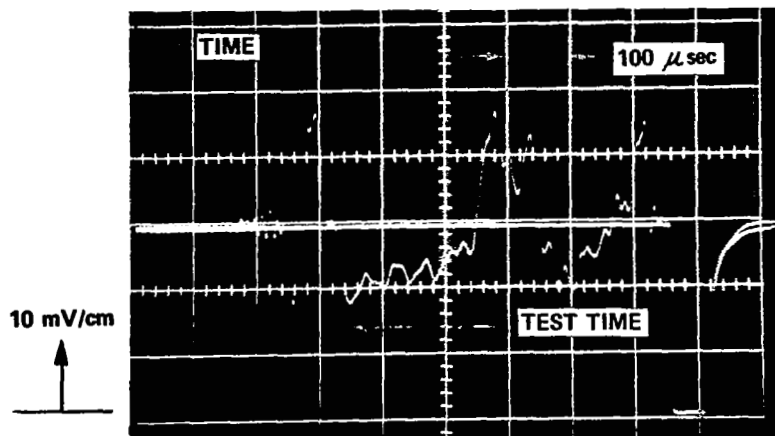
Figure 26 SCHEMATIC DIAGRAM OF FOUR-PROBE S-BAND REFLECTOMETER



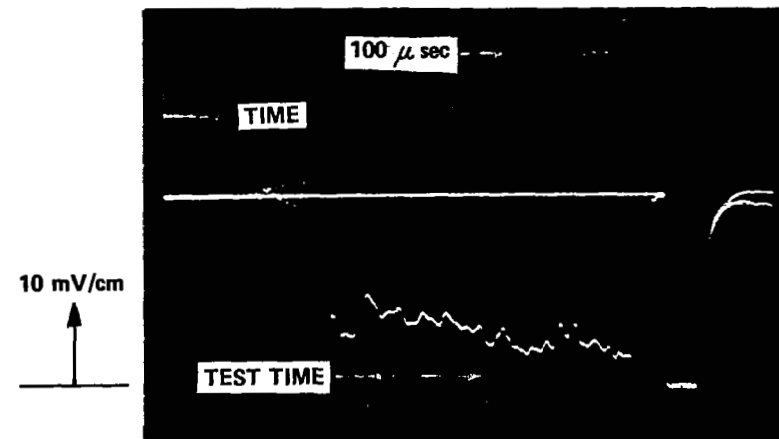
(a) REFLECTOMETER DIODE #1



(b) REFLECTOMETER DIODE #2



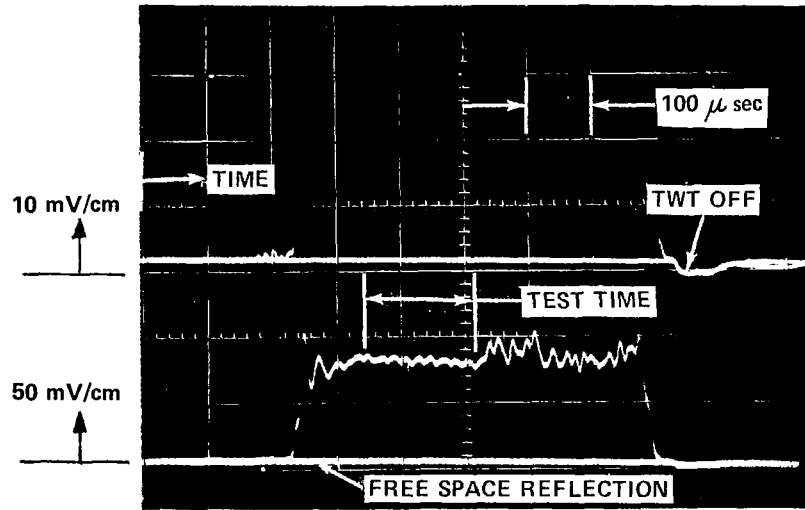
(c) REFLECTOMETER DIODE #3



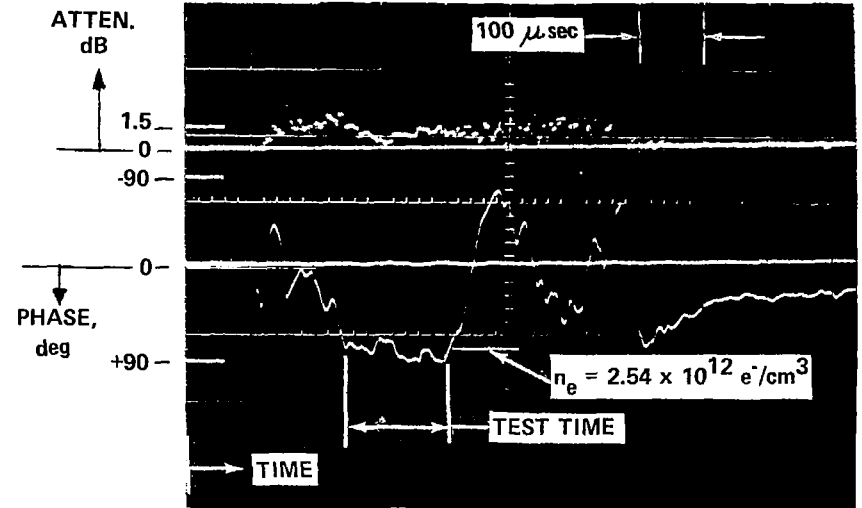
(d) REFLECTOMETER DIODE #4

- 1) ANTENNA LOCATED AT 11.25 in. FROM PLATE LEADING EDGE
- 2) PEAK ELECTRON DENSITY OVER ANTENNA DURING TEST TIME WAS  $\sim 2.7 \times 10^{11} \text{ e}^-/\text{cm}^3$
- 3) RUN #4, TABLE 2

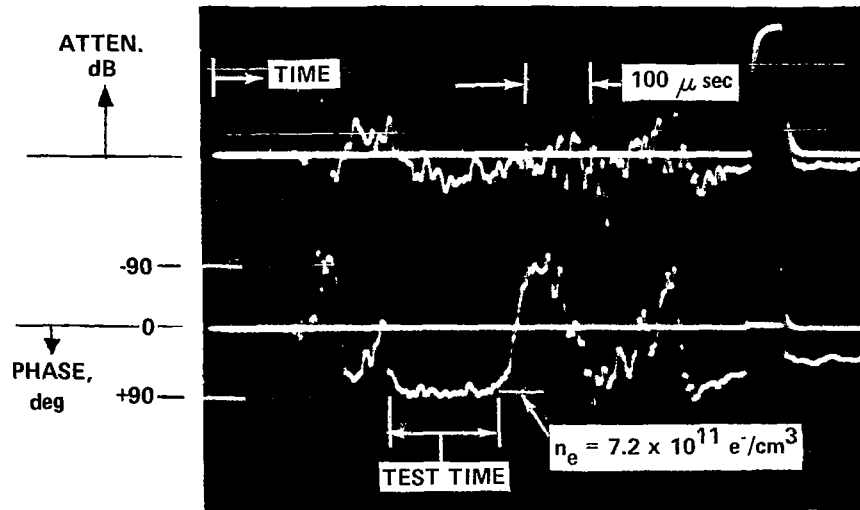
Figure 27 TYPICAL REFLECTOMETER AND MICROWAVE-INTERFEROMETER OSCILLOSCOPE RECORDS FOR RAM C S-BAND ANTENNA IN CARBON MONOXIDE PLASMA



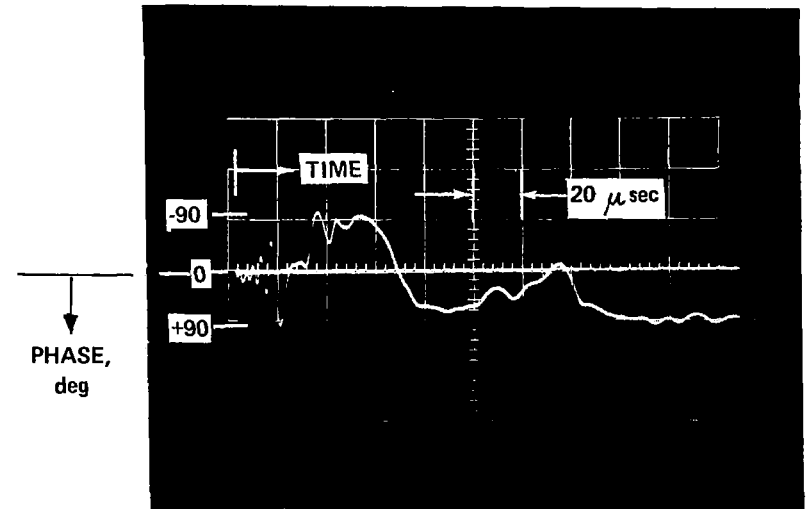
(d) REFLECTOMETER REFLECTED SIGNAL



(e) 35 GHz MICROWAVE INTERFEROMETER AT 11 in. UPSTREAM OF PLATE LEADING EDGE



(f) 17 GHz MICROWAVE INTERFEROMETER AT 1 in. UPSTREAM OF PLATE LEADING EDGE



(g) 17 GHz MICROWAVE INTERFEROMETER ON FAST SWEEP SPEED

Figure 27 TYPICAL REFLECTOMETER AND MICROWAVE-INTERFEROMETER OSCILLOSCOPE RECORDS FOR RAM C S-BAND ANTENNA IN CARBON MONOXIDE PLASMA (Cont.)

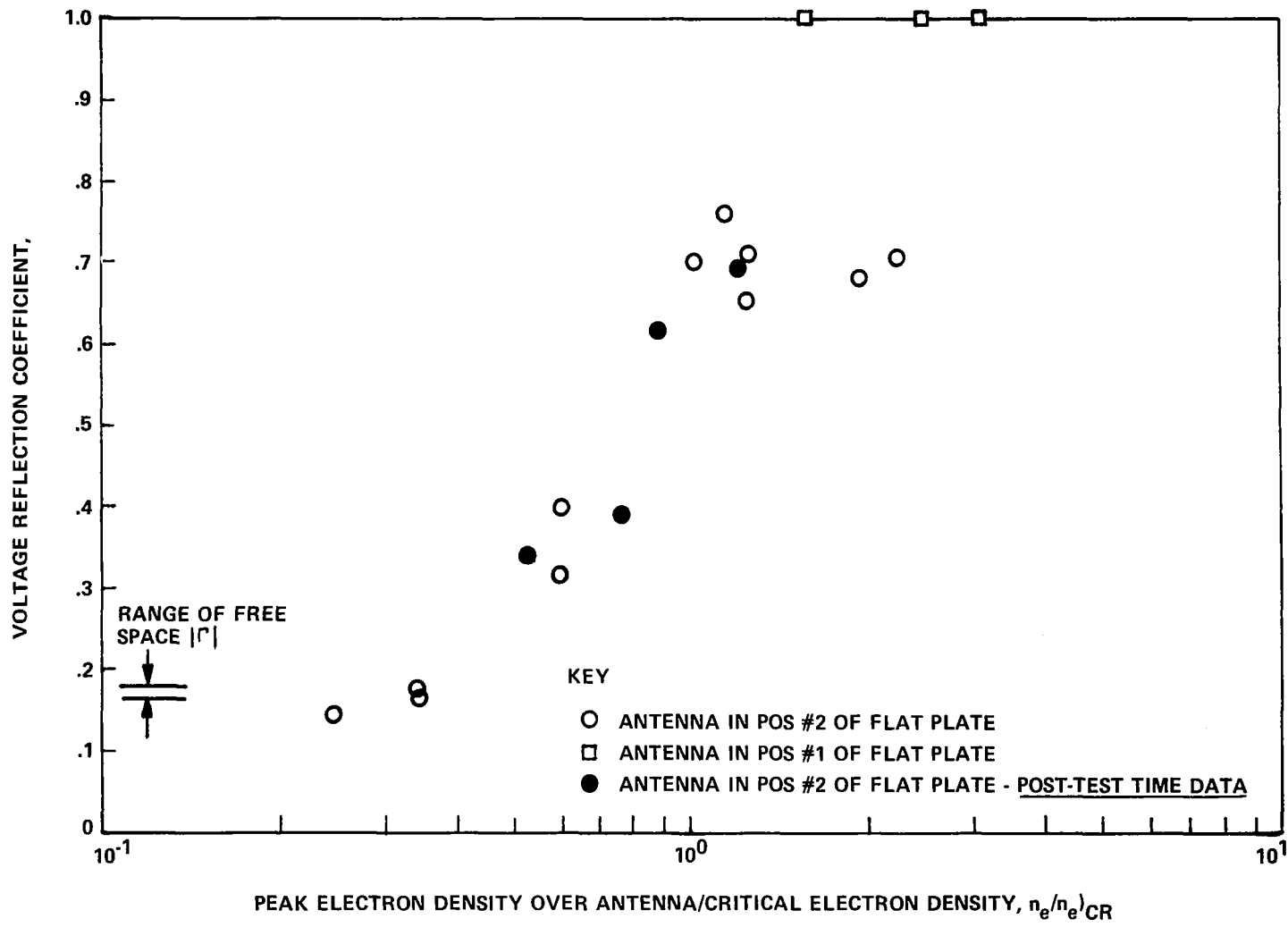


Figure 28 VOLTAGE REFLECTION COEFFICIENT MEASUREMENTS WITH RAM C S-BAND ANTENNA IN CARBON MONOXIDE PLASMA

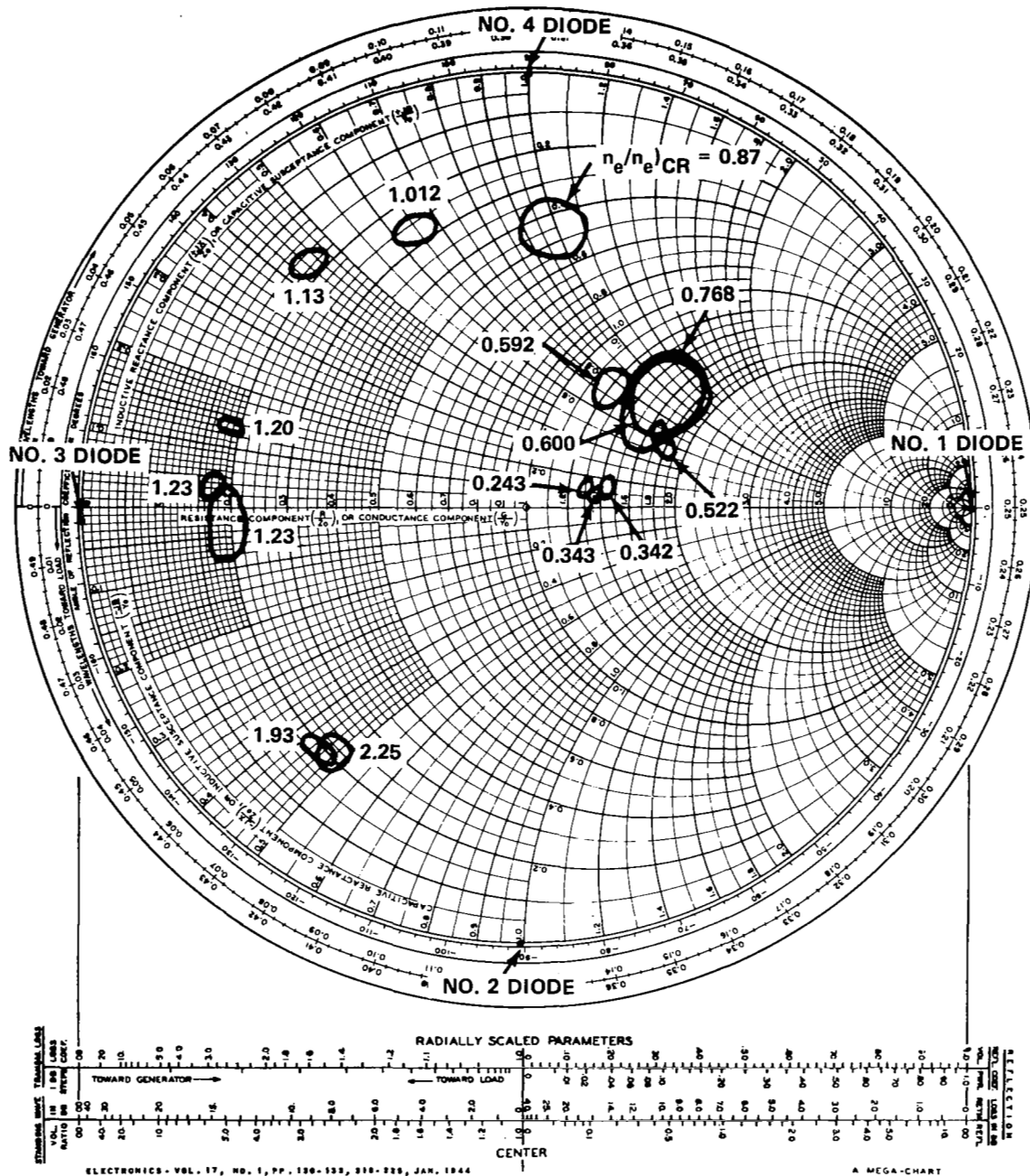


Figure 29 EXPERIMENTAL RESULTS OBTAINED WITH RAM C S-BAND ANTENNA AT PLATE POS. NO. 2 IN CARBON MONOXIDE PLASMA

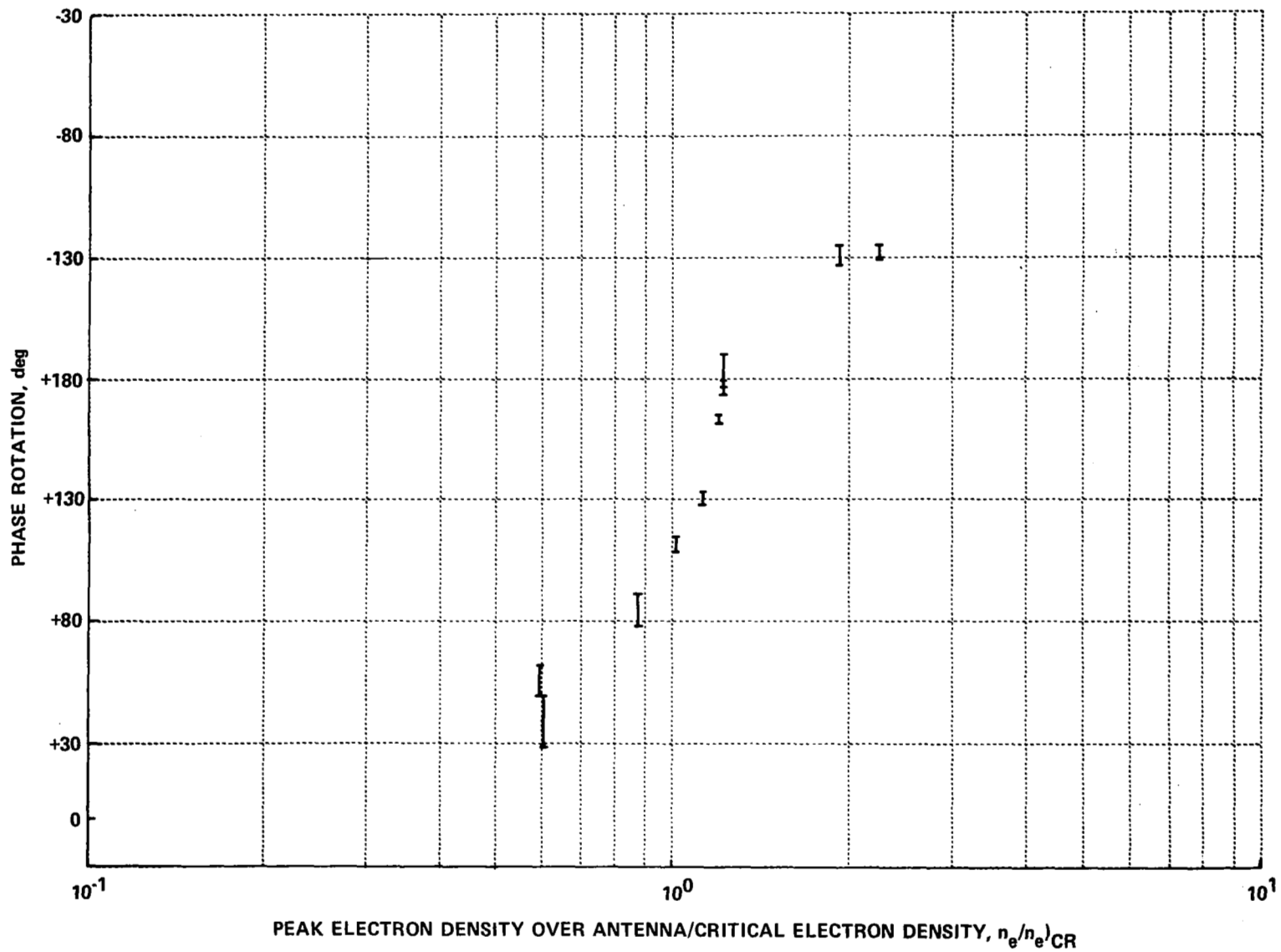
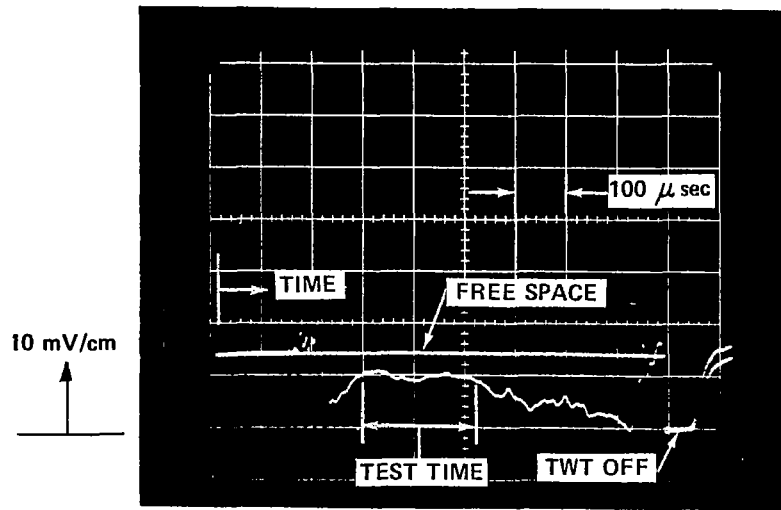
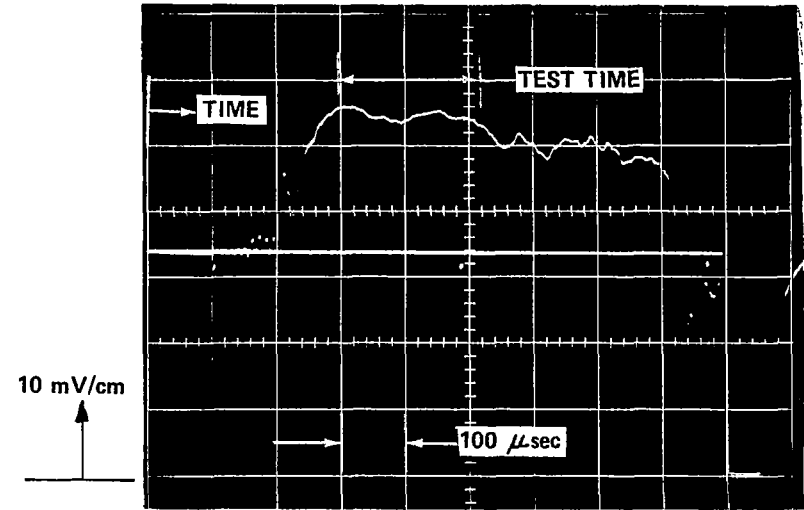


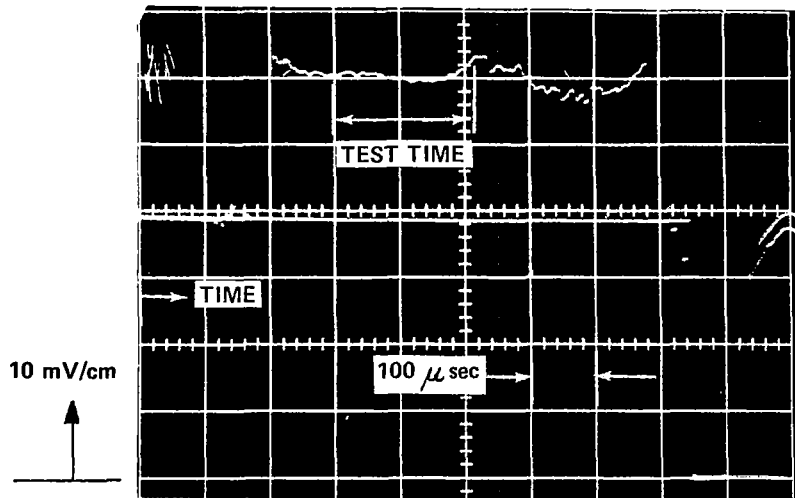
Figure 30 PHASE ROTATIONS MEASURED WITH RAM C S-BAND ANTENNA AT PLATE POS #2 IN CARBON MONOXIDE PLASMA



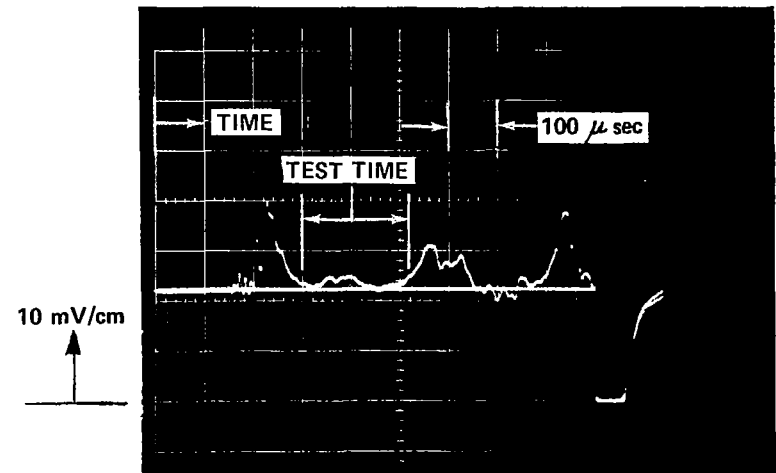
(a) REFLECTOMETER DIODE #1



(b) REFLECTOMETER DIODE #2



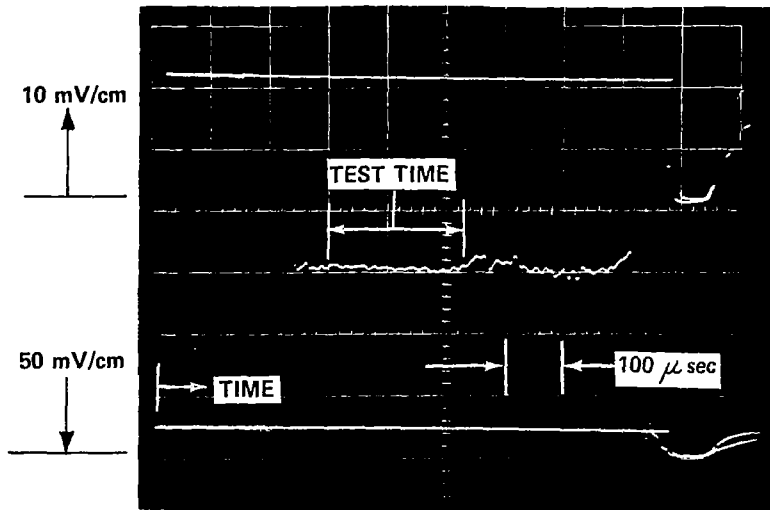
(c) REFLECTOMETER DIODE #3



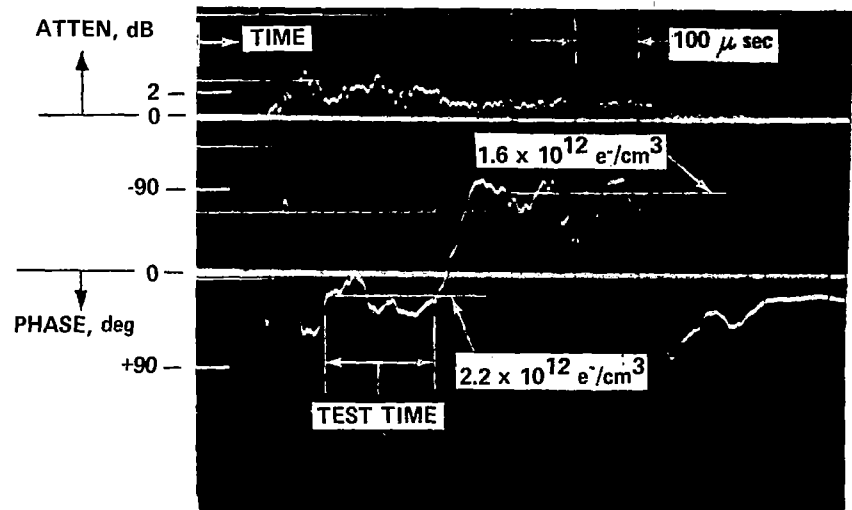
(d) REFLECTOMETER DIODE #4

- 1) ANTENNA LOCATED AT 6.75 in. FROM PLATE LEADING EDGE
- 2) PEAK ELECTRON DENSITY OVER ANTENNA DURING TEST TIME WAS  $n_e \approx 3.8 \times 10^{11} \text{ e}^-/\text{cm}^3$
- 3) RUN #16, TABLE 3

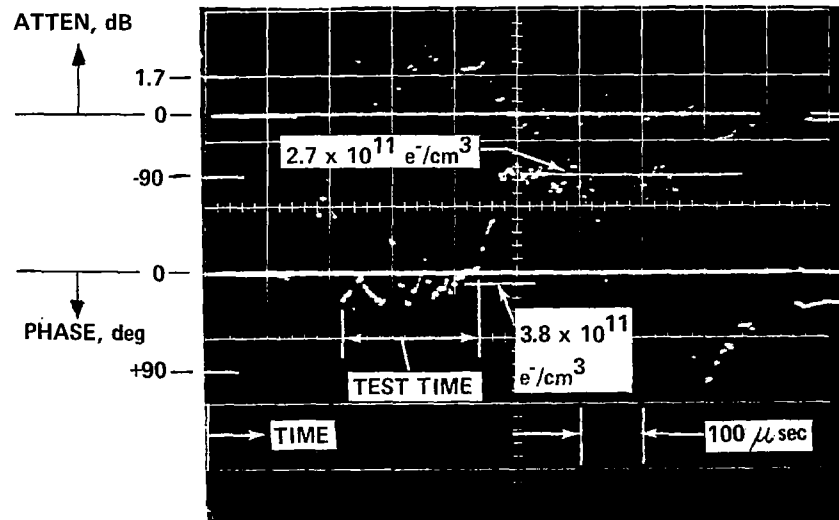
Figure 31 TYPICAL REFLECTOMETER AND MICROWAVE-INTERFEROMETER OSCILLOSCOPE RECORDS FOR RAM C-C S-BAND ANTENNA IN CARBON MONOXIDE PLASMA



(e) REFLECTOMETER REFLECTED SIGNAL



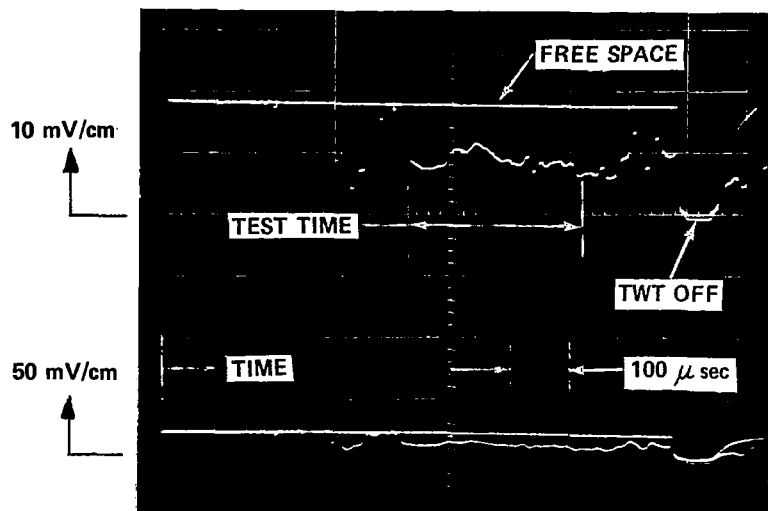
(f) 35 GHz MICROWAVE INTERFEROMETER AT 11 in. UPSTREAM OF PLATE LEADING EDGE



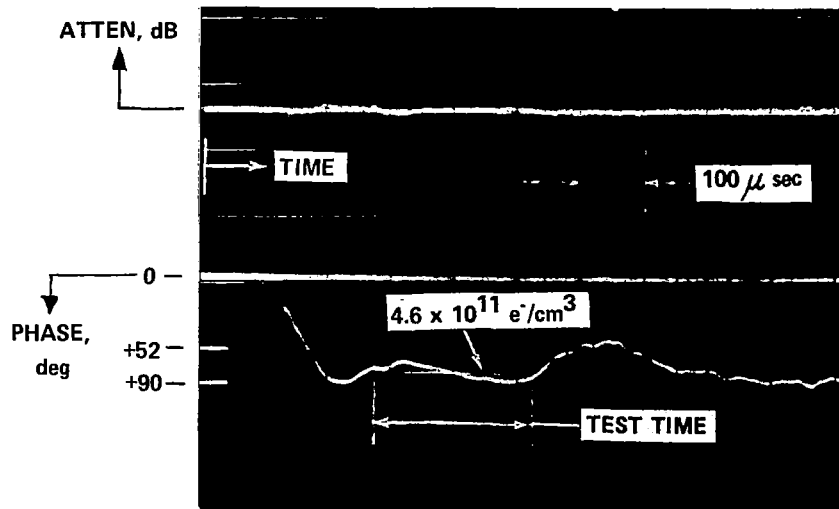
(g) 17 GHz MICROWAVE INTERFEROMETER AT 1 in. UPSTREAM OF PLATE LEADING EDGE

Figure 31 TYPICAL REFLECTOMETER AND MICROWAVE-INTERFEROMETER OSCILLOSCOPE RECORDS FOR RAM C-C S-BAND ANTENNA IN CARBON MONOXIDE PLASMA (Cont.)

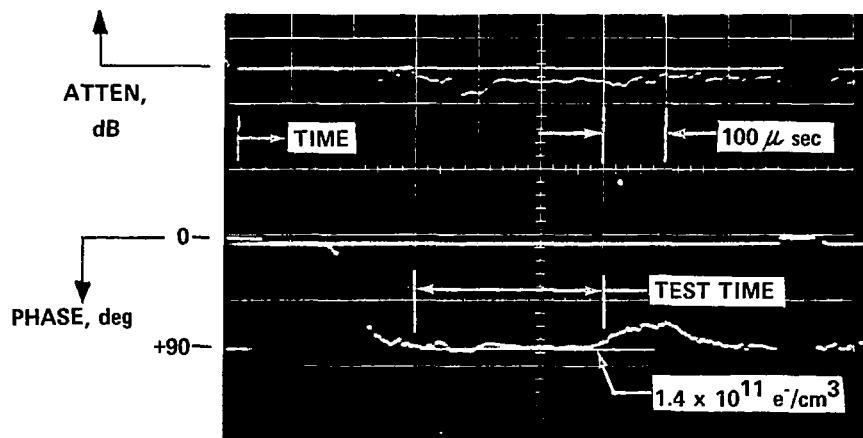




(a) REFLECTOMETER REFLECTED SIGNAL



(b) 35 GHz MICROWAVE INTERFEROMETER LOCATED 11 in. UPSTREAM OF PLATE LEADING EDGE



(c) 17 GHz MICROWAVE INTERFEROMETER LOCATED 1 in. UPSTREAM OF PLATE LEADING EDGE

Figure 33 VOLTAGE REFLECTION AND MICROWAVE-INTERFEROMETER MEASUREMENTS FOR RAM C-C ANTENNA SUGGESTING PLASMA TUNNING

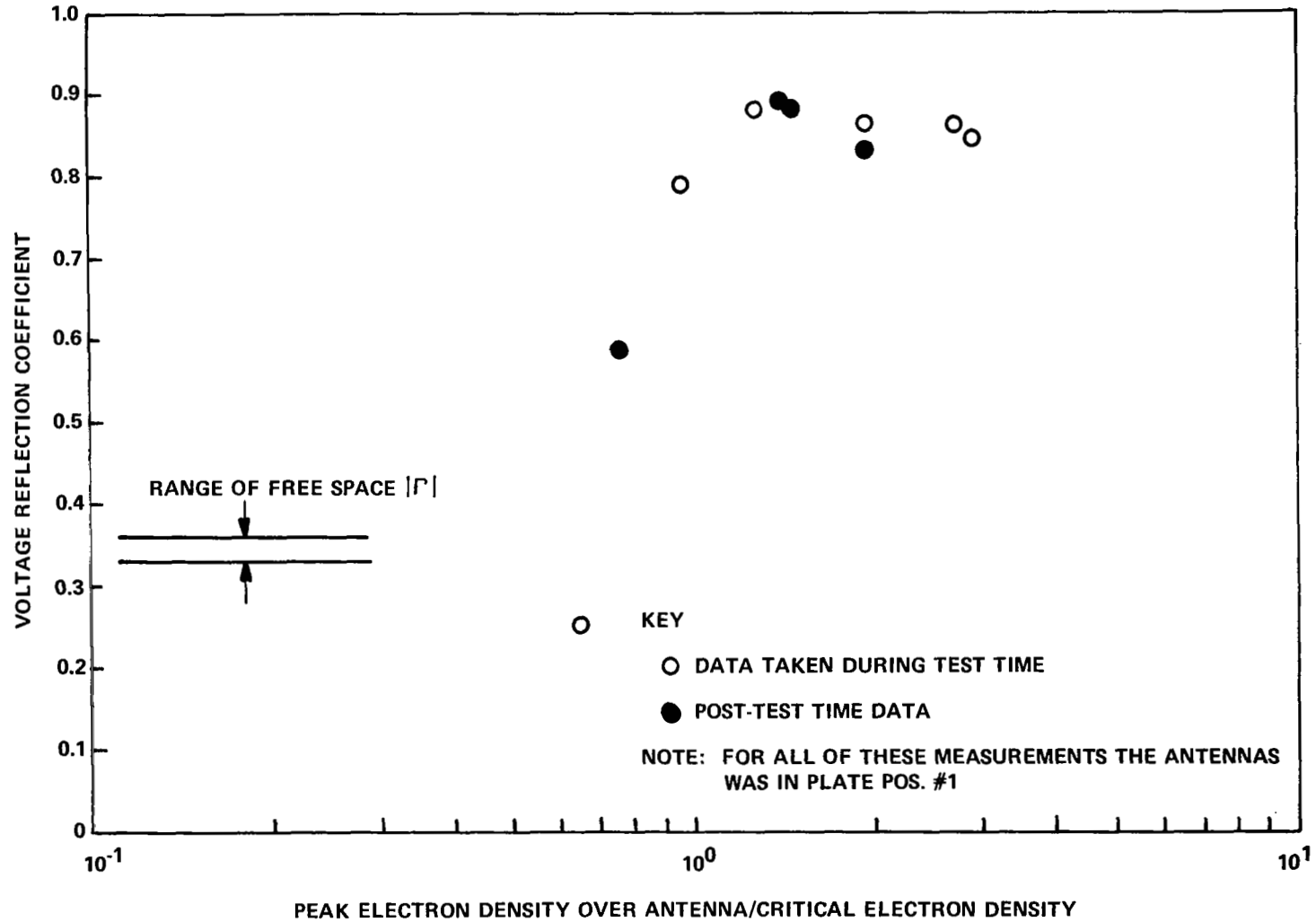


**Figure 34 VOLTAGE REFLECTION COEFFICIENT MEASUREMENTS WITH RAM C-C S-BAND ANTENNA IN CARBON MONOXIDE GAS**

## APPENDIX "A"

### SIGNAL ATTENUATION IN THE ABSENCE OF ABLATION FOR MARS-VIKING ENTRY CONDITIONS

By M. G. Dunn and S. W. Kang

Cornell Aeronautical Laboratory, Inc.  
Buffalo, New York

#### 1. INTRODUCTION

Near the end of this contract, a study was performed using state-of-the-art techniques to obtain estimates of the signal attenuation for the Mars-Viking entry conditions. Flow-field calculations with nonequilibrium chemical reactions were carried out in order to obtain preliminary estimates of the electron-density and collision-frequency distribution in the stagnation region of the Viking lander capsule for the  $\min \rho_s$ , mean  $\rho$ ,  $\max \rho_s$  and  $\max H \rho_s$  trajectories supplied by the Martin Company<sup>1</sup> for a  $-17^\circ$  entry angle.

For the purposes of the preliminary estimates required of this study and the short time period available, the stagnation-region plasma was felt to be reasonably representative of the plasma anticipated over the conical section of the forebody. Estimates of the plasma-layer thickness and the number-density distributions are presented later in the text for locations away from the stagnation region which provide an indication of the probable differences between the plasma in these locations. As will be discussed later, this downstream flow field should be analyzed in more detail in order to obtain improved estimates of the signal attenuation history.

The calculated electron-density and collision-frequency distributions in the stagnation region plasma were used to calculate the plane-wave transmission coefficient (for frequencies from 100 Mc to 3000 Mc) history for the  $\max \rho_s$  and  $\max H \rho_s$  trajectories. Both inviscid and viscous-layer flow-field analyses were performed. The atmospheric composition was considered to be either 99%  $\text{CO}_2$  + 1%  $\text{N}_2$  or 75%  $\text{CO}_2$  + 20% Ar + 5%  $\text{N}_2$ . Time did not permit an assessment of the influence of ablation impurities on the electron-density and collision-frequency distributions. It is felt that the ablation impurity question must be answered before appropriate estimates of these necessary distributions can be obtained.

The nonequilibrium calculations mentioned above utilized a set of reaction rate coefficients given in Table 1A that represented our best estimates considering the current state of the art. As will be shown later, the predicted electron densities are sensitive to the magnitude of the rate

coefficients selected for each of several reactions. It is important to emphasize that the predictions presented here are only as accurate as the reaction rate coefficients used in the analysis.

The technique used herein to calculate the inviscid, nonequilibrium flow behind the bow shock was that described by Marrone<sup>2</sup> and Gibson and Marrone.<sup>3</sup> Since this technique is well known, it is not necessary to discuss it in detail. However, the viscous-layer flow-field calculation technique is not as well known and Section 2 is included in this appendix in order to help clarify the physics of this problem. In section 3, typical results of the calculations performed during the available time period are presented. A brief description of the downstream viscous-layer solution and a description of the technique that could be used to predict the influence of ablation impurities on the plasma properties are given in Section 4. Recommendations for future work that should be completed before accurate estimates of the communication blackout boundaries can be defined are given in the conclusion of the text.

## 2. VISCOUS, HYPERSONIC SHOCK-LAYER

During entry into the Martian atmosphere, the flow field surrounding the Viking vehicle undergoes changes in character depending upon conditions such as the vehicle velocity, angle of attack, the Mars atmosphere model, and the altitude. For given flight conditions, the important parameter delineating the character of the flow is the altitude (or density) effect. Specifically, at low altitudes, the flow field consists of a thin boundary layer and an inviscid shock layer around the vehicle. However, the low-density effect (or low-Reynolds number effect) prevails at high altitudes, resulting in the completely viscous shock layer, and there no longer exists an "inviscid" hypersonic shock layer and a thin ("Prandtl") boundary layer. Thus it is important to determine where the viscous shock-layer regimes exist for given flight conditions in the Martian atmosphere.

For this purpose, calculations were performed for the boundary-layer thickness ( $\delta$ ) and the inviscid shock-layer thickness ( $\Delta$ ) as a function of the altitude for various Martian entry trajectories. The boundary-layer thickness was calculated from the Prandtl equations and is based on the works of Fay and Riddell<sup>4</sup> and Scala and Baulknight.<sup>5</sup> Separate calculations were made for the inviscid shock-layer thickness based on Hayes and Probst.<sup>6</sup>

Figure 1 shows the results of these calculations in terms of  $\delta/\Delta$  at the stagnation region as a function of the altitude and the flight trajectory. The lower shaded region describes the altitude ranges in which the thin boundary-layer approximation and the inviscid shock-layer equations are valid. And, strictly speaking, this is the region in which the above calculations are quantitatively meaningful. Beyond this region, that is, for  $\delta/\Delta \geq 0.1$  (higher altitudes), the flow-field character changes such that at first the viscous interaction is important and then the "inviscid" shock layer

disappears as a result of the viscous effects extending all the way to the shock wave. Therefore, beyond the lower shaded portion, it is no longer correct to treat the flow field in terms of the thin boundary-layer flow and the inviscid shock layer.

The upper shaded portion delineates the altitude ranges in which the shock layer is now entirely viscous. This brings about two effects which directly influence the magnitudes of the electron-number densities in the shock layer. The first is that the effect of the low surface temperature of the vehicle is felt in the entire shock layer, causing a decrease in the overall flow-field temperature. The second is that there exists species diffusion in the layer so that the electrons diffuse both to the vehicle surface and to the shock wave, resulting in lower values of the electron-number densities and a "smoothed-out" profile shape in the viscous shock layer.

It is thus clear that new analyses are necessary for this region dealing with the effects described above. This has been done by Kang for the case of mass injection,<sup>7</sup> for the ionized nonequilibrium case<sup>8</sup> and for the ablating nonequilibrium case.<sup>9</sup> These analyses were applied to the Mars entry case for the Viking vehicle and some of the results obtained to date will be presented in greater detail in the following sections. For the intermediate "viscous-interaction" region between the viscous-shock-layer flow regime and the boundary-layer flow regime, the analysis for the viscous-layer flow was extended to obtain the electron-number-density distributions. The results based on the thin boundary-layer and the inviscid shock-layer flow will also be presented for comparison in the following sections.

### 3. RESULTS OF INVISCID AND VISCOUS SHOCK-LAYER CALCULATIONS

The previous section described the altitude region of applicability for the four atmosphere-trajectories of interest in terms of the thin boundary-layer-inviscid flow regime and the viscous shock-layer regime. In this section we present results obtained throughout these entry trajectories assuming that each of these two flow-field analyses were valid. It is very important to emphasize that in the altitude region between these two regimes (see Fig. 1) the thin boundary-layer-inviscid flow analysis gives an upper limit of the number density and the viscous shock-layer analysis gives a lower limit of the number density. Therefore, it is necessary for the user of these calculations to apply some judgement, based upon his particular interest, in arriving at the predictions of electron number density in this intermediate flow-field regime.

Before continuing with the presentation of our results, it is important to re-emphasize that the calculations presented in this section do not include the influences of ablation products on the shock layer electron-density and collision-frequency profiles. The reader is cautioned against directly applying the results presented herein in view of the possible major effects of ablation products. The Martin Company<sup>1</sup> has already performed calculations

to assess this importance in the thin boundary-layer flow regime assuming conditions of chemical equilibrium. The possible influences of finite rate chemical reactions on these boundary-layer profiles should probably be assessed. A later section of this appendix describes a method that could be used to assess the importance of these impurities in the chemically-reacting viscous shock-layer regime. It would also then be possible to estimate the electron number densities in the altitude regime between these two flow regimes as discussed in the previous paragraph.

### 3.1 Chemical Kinetics Model and Rate Coefficients

The inviscid, nonequilibrium flow-field program was initially used with a large chemical kinetics model to ascertain the relative importance of various chemical reactions through the shock layer. By doing so, it was possible to reduce the model to the reactions and their respective rate coefficients given in Table 1A. Of these, reactions 14-18 and 20, 21 and 23 could in general be eliminated from the model without loss of accuracy providing that their rate coefficients given in Table 1 are correct.

The electron-density distributions and peak values predicted in the shock layer are sensitive to the magnitude of the reaction rate coefficients as illustrated in Fig. 2. For this particular case, the magnitude of the rate coefficient for the reaction  $\text{CO}_2 + \text{M} \rightarrow \text{CO} + \text{O} + \text{M}$  was varied by  $\pm 10$  from the Table 1 value. The difference between the peak values of predicted electron density is approximately an order of magnitude. The influence of this rate coefficient perturbation on the heavy-particle translational temperature distribution and on the  $\text{NO}^+$ ,  $\text{O}_2^+$ , and  $\text{CO}^+$  ion concentrations is shown on Figs. 3 and 3(a). The relative importance of the  $\text{O}_2^+$  and  $\text{NO}^+$  ions in the shock layer is shown to be influenced by the neutral chemistry reaction.

Several investigators<sup>11-13</sup> have studied this reaction at low temperatures in shock-tube environments. However, there still exist large uncertainties in the reaction rate coefficients for unknown reasons. Brokaw<sup>14</sup> has suggested that the difficulty associated with these previous measurements is the presence of hydrogenous impurities. To date, the difficulty has not been satisfactorily resolved.

Two additional reactions of importance in the plasma layer are (1)  $\text{N} + \text{CO}_2 \xrightarrow{k_1} \text{NO} + \text{CO}$  and (2)  $\text{O} + \text{N}_2 \xrightarrow{k_2} \text{NO} + \text{N}$ . The rate coefficient for reaction (2) has recently been measured<sup>15</sup> in a shock-tube environment and is known to within a factor of  $\pm 3$  for a temperature range of 2000 to 5000°K. The rate coefficient for reaction (1) has not been measured for the environment and temperature range of interest.

There are uncertainties in many of the remaining neutral chemistry reactions that also could result in pronounced influences on the predicted electron-density levels. If these influences happen to be additive, then it would be possible to realize much higher electron-density values than those presented in the remainder of this work.

### 3.2 Collision-Frequency and Electron-Density Distributions in Stagnation-Region Plasma

The collision-frequency and electron-density distributions in the stagnation region plasma were calculated for many points along each trajectory using the inviscid, nonequilibrium-flow analysis and the viscous shock-layer, nonequilibrium-flow analysis. The electron-neutral momentum-transfer cross sections for the species  $O_2$ ,  $CO$  and  $CO_2$  have been experimentally determined over the electron energy range of interest by Hake and Phelps.<sup>16</sup> Cross sections for the remaining species are well known from previous earth-entry studies. For all of the trajectory points considered, the electron-ion collision frequency was always small compared with the electron-neutral collision frequency.

Figure 4 presents a comparison of collision-frequency distributions calculated using the inviscid and merged-layer analyses for the  $\max \rho_s$  trajectory at an altitude of 285,000 ft and a velocity of 14,500 ft/sec. From Fig. 1 it is seen that at this trajectory point the merged-layer analysis would be the correct one to use. Because of the lower wall temperature associated with the merged-layer solution, the predicted collision frequency near the wall is somewhat higher than it is for the inviscid solution. Nearer the shock the results of the two solutions are in good agreement as to the magnitude of the collision frequency. This lower wall temperature results in a higher gas density near the wall with a corresponding thinning of the shock-layer thickness as can be seen from Fig. 4.

The corresponding electron-density profiles for this trajectory point are given in Fig. 5. The merged-layer profile has a peak electron density of approximately 1/50 the inviscid flow peak value. Near the body, the influence of the low wall temperature on the profile can be observed. Because diffusion is allowed towards both the body and the shock, the number density is fairly uniform over most of the shock layer.

Figures 6 and 7 present a similar comparison of collision frequency and electron density for an altitude of 215,000 ft at 14,800 ft/sec for the  $\max \rho_s$  trajectory. From Fig. 1, it can be seen that for this trajectory point the viscous shock-layer analysis should be valid. Figure 6 illustrates a significant difference between the collision-frequency distributions with the prediction of the merged-layer solution being almost a factor of 10 less than that of the inviscid solution near the shock. The electron-density profiles presented in Fig. 7 illustrate a significant viscous effect. The peak electron density predicted by the merged-layer analysis is in excess of  $10^3$  times less than that of the inviscid-flow prediction.

### 3.3 Predicted Peak Electron Densities for Various Atmosphere-Trajectories

Inviscid and merged-layer nonequilibrium flow calculations were performed for several points along the  $\min \rho_s$ ,  $\text{mean } \rho$ ,  $\max \rho_s$  and

$\max H\rho_{,s}$  trajectories for an entry angle of  $-17^\circ$  using an atmosphere composed of 99%  $\text{CO}_2$  + 1%  $\text{N}_2$ . These calculations were repeated for the  $\max\rho_{,s}$  and  $\max H\rho_{,s}$  trajectories using an atmosphere composed of 75%  $\text{CO}_2$  + 20%  $\text{Ar}$  + 5%  $\text{N}_2$ .

Figures 8 and 9 present the inviscid and merged-layer predictions of the peak electron densities as a function of altitude for the  $\min\rho_{,s}$  and mean  $\rho$  trajectories for an atmosphere composed of 99%  $\text{CO}_2$  + 1%  $\text{N}_2$ . Referring to Fig. 1, it can be seen that for the  $\min\rho_{,s}$  trajectory at altitudes less than 120,000 ft the thin-boundary layer-inviscid flow analysis is valid and above approximately 215,000 ft the merged layer analysis is valid. Between 120,000 ft and 215,000 ft altitude the inviscid prediction represents an upper bound and the merged-layer prediction represents a lower bound to the electron density. Similarly, for the mean  $\rho$  trajectory the boundary-layer regime is below 115,000 ft and the merged-layer regime is above approximately 195,000 ft. For intermediate altitudes the results can be used in the manner described earlier in this paragraph.

The influence of ablation products on the peak electron densities has not been included in these results. Because of this, the altitudes of predicted  $1\dot{q}_c)_{\max}$  and  $0.5\dot{q}_c)_{\max}$  are noted on Figs. 8-11. For the altitudes at which  $0.5\dot{q}_c)_{\max}$  occurs, the number density calculated assuming only atmospheric ionization can be seen to be decreasing. It is therefore clear that before these results can be used to predict the communications blackout boundaries, the additional electron production as a result of impurity ionization must be assessed.

Figures 10 and 11 present the inviscid-flow and merged-layer flow predictions of peak electron density for the  $\max\rho_{,s}$  and  $\max H\rho_{,s}$  trajectories using the 99%  $\text{CO}_2$  + 1%  $\text{N}_2$  and the 75%  $\text{CO}_2$  + 20%  $\text{Ar}$  + 5%  $\text{N}_2$  atmospheres. Again from Fig. 1, for the  $\max\rho_{,s}$  trajectory, the boundary-layer analysis is valid at altitudes below approximately 115,000 ft and the merged-layer analysis is valid above approximately 175,000 ft. The corresponding altitudes for the  $\max H\rho_{,s}$  trajectory are approximately 160,000 ft and approximately 250,000 ft. Between these altitude ranges, the electron density lies between the upper limit of the inviscid-flow prediction and the lower limit of the merged-layer prediction.

Figures 10 and 11 illustrate that adding 20%  $\text{Ar}$  and an additional 4%  $\text{N}_2$  to the atmospheric composition results in an increase in the predicted peak number density of a factor of approximately 10 near the maximum number-density region. Because of the limited time available, it was not possible to separate the relative influences of the Argon and the additional nitrogen.

### 3.4 Estimated Plane-Wave Transmission Coefficient

The collision-frequency and electron-density distributions described in Section 3.2 have been used to calculate<sup>17</sup> the plane-wave transmission coefficient as a function of altitude for the  $\max\rho_{,s}$  and  $\max H\rho_{,s}$

trajectories using the 75% CO<sub>2</sub> + 20% Ar + 5% N<sub>2</sub> atmosphere. The results of these calculations are shown in Figs. 12 and 13 for frequencies ranging from 100 Mc to 3000 Mc. For the purposes of this calculation, the gradients of collision frequency and electron density in the direction of propagation were accounted for by assuming the plasma layer to be composed of many smaller homogeneous slabs. However, the calculation technique is restricted in that it requires that these gradients normal to the direction of electromagnetic propagation be negligible.

The predictions of transmission coefficient vs. altitude obtained using the inviscid, nonequilibrium-flow solutions and the viscous, nonequilibrium-flow solutions are both included on Figs. 12 and 13. In Section 3.3 the altitude range over which each of these flow-field prediction techniques should be valid is described. In the intermediate altitude range, it is necessary to interpolate between the upper limit of the inviscid-flow and the lower limit of the viscous-flow predictions.

#### 4. DOWN-STREAM VISCOUS SHOCK-LAYER SOLUTIONS AND ABLATION-PRODUCT IONIZATION

##### 4.1 Downstream Viscous Shock-Layer Solutions

Throughout this appendix it has been emphasized that to date we have studied the stagnation-region plasma. The downstream flow field is also important since the radar altimeter is located on the forebody away from the stagnation region and because we are interested in the number density and collision frequency in the afterbody region.

The existing analysis<sup>8</sup> was applied for the Viking vehicle in the spherical portion and the results are shown in Fig. 14 in terms of the electron-density profiles in the viscous shock layer. It may be seen that the peak electron-number density is greatest in the stagnation region and gradually decreases in the downstream region due to expansion of the flow. For a very blunt body such as the Viking vehicle, the spherical portion ends at  $\theta = 20$  degrees from the stagnation line ( $\theta = 0$ ) and the results show a decrease in the maximum electron density level from the stagnation value by a factor of about two for the given Martian atmosphere (5% N<sub>2</sub>, 20% Ar, 75% CO<sub>2</sub>).

Beyond the nose region, the body shape changes from a spherical to a conical section and modification of the presently available program is required to account for the change in the body curvature. Although there seems to be no major conceptual difficulty in adapting the program, lack of sufficient time has precluded us from implementing this modification.

##### 4.2 Ablation-Product Ionization

In a hypersonic, viscous shock-layer flow, the ablation species

released into the flow are not confined to a thin layer near the body, but are diffused all the way to the shock wave. Of these "contaminant" species some will undergo ionization, generating new electrons in addition to those electrons already in the flow field. At high altitudes, conditions of chemical nonequilibrium will prevail so that an analysis of nonequilibrium ionization of the contaminant species should be performed. This had been previously done by Kang<sup>9</sup> and applied to the Apollo vehicle. The analysis, however, has not been applied for the Viking case due to lack of sufficient time required to modify the analysis. Hence, the results performed for an air flow over the Apollo vehicle will be presented here, in order to demonstrate qualitatively the importance of the ablation effects.

The results are shown in Fig. 15 in terms of the distributions of electron-number densities across the viscous shock layer for an Apollo vehicle in the Earth atmosphere for the ablation case. The term  $N$  is defined to be the ratio of the ablation mass flux ( $\rho_b V_b$ ) to the free-stream mass flux ( $\rho_\infty U_\infty$ ), where  $\rho$  denotes mass density,  $V$  and  $U$  the velocities, and the subscripts  $b$  and  $\infty$  the body-surface condition and the ambient condition, respectively. Physically, the term  $N$  signifies the percent of ablated mass in the flow compared to the ambient mass flux. This figure illustrates the electron-density profiles for the case of  $N = 0.1$  containing 100 ppm of sodium, and the case of  $N = 0.1$  containing 1000 ppm of sodium. For comparison, the case of pure air (no ablation) is also included in the figure. It may be seen that ablation results in the thickening of the viscous shock layer<sup>7</sup> and in the increase in the number of electrons in the flow due to the nonequilibrium sodium ionization. It may be seen further that, for 1000 ppm of sodium species ablated, the peak electron number density increased by more than an order of magnitude for air. Although it is not possible to assess quantitatively or extrapolate the increase in the number of electrons due to ablation in the Martian atmosphere based on the results obtained for air, it nevertheless seems clear that the effects of ablation and the nonequilibrium ionization of the alkali metals such as sodium on the viscous flow field will be sizable in terms of the shock-layer thickness and the electron-number densities around the Viking vehicle during entry into the Martian atmosphere.

## 5. RECOMMENDATIONS

Before estimates of the blackout boundaries for the Viking Mars-entry trajectories can be obtained from the material presented herein, there are several remaining problem areas that must be investigated. These problems are as follows:

- (1) To improve our knowledge of reaction rate coefficients for the  $\text{CO}_2$  atmosphere. Section 3.1 contains a discussion of the current rate-coefficient information. It is important to recall that the nonequilibrium-flow electron-density predictions are only as accurate as the reaction rate coefficients.

(2) Extend the existing nose-region viscous-flow solution with non-equilibrium chemistry to the downstream region as discussed in Section 4.1.

(3) Investigate the influence of ablation products on the downstream viscous-flow electron-density levels. As discussed in Section 4.2 this task is a natural extension of Item (2) above.

(4) Investigation of a technique for predicting the near-wake non-equilibrium flow field for the Viking body.

#### REFERENCES

1. Viking '75 Project, "Viking Aerophysics Data Book," Martin-Marietta Corp. Rept. TR-3720003, Revision A, page VI-3 to VI-5, Dec. 1970.
2. Marrone, P.V., "Inviscid, Nonequilibrium Flow Behind Bow and Normal Shock Waves, Part I. General Analysis and Numerical Examples," Cornell Aeronautical Laboratory Report No. QM-1626-A-12 (I), May 1963.
3. Gibson, W.E. and Marrone, P.V., "A Correspondence Between Normal Shock and Blunt-Body Flows," Cornell Aeronautical Laboratory Report No. QM-1626-A-7, June 1962.
4. Fay, J.A. and Riddell, F.R., "Theory of Stagnation Point Heat Transfer in Dissociated Air," *J. Aeron. Sci.*, 25, pp. 73-85 (Feb. 1958).
5. Scala, S.M. and Bauknight, C.W., "Transport and Thermodynamic Properties in a Hypersonic Laminar Boundary Layer - Part 2. Applications," *ARS J.*, 30, pp. 329-336 (April 1960).
6. Hayes, W.D. and Probstein, R.F., Hypersonic Flow Theory, Academic Press, New York (1959) p. 162.
7. Kang, S.W., "Hypersonic, Low Reynolds Number Flow over a Blunt Body with Mass Injection," *AIAA J.* 7, pp. 1546-1552 (Aug. 1969).
8. Kang, S.W., "Nonequilibrium, Ionized Hypersonic Flow over a Blunt Body at Low Reynolds Number," *AIAA J.* 8, pp. 1263-1270 (July 1970).
9. Kang, S.W., "Nonequilibrium, Viscous Shock Layer with Ablation," (to be published).
10. Sulzman, K.G.P., Myers, B.F., and Bartle, E.R., "CO Oxidation I. Induction Period Preceding CO<sub>2</sub> Formation in Shock Heated

CO - O<sub>2</sub> - Ar Mixtures," Journal of Chemical Physics, Vol. 42, No. 11, June 1965, pp. 3969-3979; "Oxidation of CO II. Influence of H<sub>2</sub> on the Induction Period Preceding Rapid CO<sub>2</sub> Formation in Shock-Heated CO - O<sub>2</sub> - Ar Mixtures," Journal of Chemical Physics, Vol. 43, No. 4, Aug. 1965, pp. 1220-1228.

11. Fishburne, E.S., Bilwakesh, K.R., and Edse, R., "Chemical Kinetics of Entry into the Martian Atmosphere," Aerospace Research Laboratories Rept. 67-0113, May 1967.
12. Drummond, L.J., Aust. J. Chem., Vol. 21, 1968, pg. 2631.
13. Dean, A.M. and Kistiakowsky, G.B., "The Oxidation of Carbon Monoxide by Oxygen in Shock Waves," Harvard Univ., Office of Naval Research Contract No. Nonr-1866(36), Sept. 1969.
14. Brokaw, R.S., "Ignition Kinetics of the Carbon Monoxide-Oxygen Reaction," 11th Sym. on Combustion, Berkeley, 1966, pp. 1063-1073.
15. Wray, K.L., Feldman, E.V., and Lewis, P.F., "Shock Tube Study of the Effect of Vibrational Energy of N<sub>2</sub> on the Kinetics of the O + N<sub>2</sub> → NO + N Reaction," Journal of Chemical Physics, Vol. 53, No. 11, Dec. 1970, pp. 4131-4136.
16. Hake, R.D. and Phelps, A.V., "Momentum-Transfer and Inelastic-Collision Cross Sections for Electrons in O<sub>2</sub>, CO, and CO<sub>2</sub>," The Physical Rev. Vol. 158, June 1967, pp. 70-84.
17. Bein, G.P., "Plane Wave Propagation at Arbitrary Angles of Incidence in Inhomogeneous, Lossy Plasmas and Prediction of Antenna Radiation Patterns," Cornell Aeronautical Laboratory Rept. No. ER/RIS-8, Jan. 1966.

Table 1A  
CHEMICAL KINETICS MODEL USED IN CALCULATIONS (Cont.)

NO.	REACTION	THIRD BODY, M	RATE COEFFICIENT IN DIRECTION SHOWN IN cm <sup>3</sup> /mole sec OR cm <sup>6</sup> /mole <sup>2</sup> sec
16.	$O + C^+ \xrightarrow{k_f} C + O^+$		$6.66 \times 10^{12} T_e^{0.5} \exp(-5.416 \times 10^4 / R_o T)$
17.	$CO + O^+ \xrightarrow{k_f} O + CO^+$		$1.09 \times 10^{12} T_e^{0.5} \exp(-9.222 \times 10^3 / R_o T)$
18.	$O + CO^+ \xrightarrow{k_f} O_2 + C^+$		$5.47 \times 10^{12} T_e^{0.5} \exp(-7.470 \times 10^4 / R_o T)$
19.	$CO^+ + e^- \xrightarrow{k_r} C + O$		$1.5 \times 10^{22} T_e^{-1.5}$
20.	$C^+ + e^- + e^- \xrightarrow{k_r} C + e^-$		$2.2 \times 10^{40} T_e^{-4.5}$
21.	$O^+ + e^- + e^- \xrightarrow{k_r} O + e^-$		$2.2 \times 10^{40} T_e^{-4.5}$
22.	$O_2^+ + e^- \xrightarrow{k_r} O + O$		$8.0 \times 10^{21} T_e^{-1.5}$
23.	$N_2^+ + e^- \xrightarrow{k_r} N + N$		$1.5 \times 10^{22} T_e^{-1.5}$
24.	$NO^+ + e^- \xrightarrow{k_r} N + O$		$6.7 \times 10^{21} T_e^{-1.5}$
25.	$CO + NO^+ \xrightarrow{k_r} CO^+ + NO$		$4.59 \times 10^{12} T_e^{0.5} \exp(-1.096 \times 10^5 / R_o T)$
26.	$O_2 + NO^+ \xrightarrow{k_f} O_2^+ + NO$		$4.45 \times 10^{12} T_e^{0.5} \exp(-6.521 \times 10^4 / R_o T)$
27.	$CO + O_2^+ \xrightarrow{k_f} CO^+ + O_2$		$4.53 \times 10^{12} T_e^{0.5} \exp(-4.449 \times 10^4 / R_o T)$
28.	$O + NO^+ \xrightarrow{k_f} O_2^+ + N$		$5.41 \times 10^{12} T_e^{0.5} \exp(-9.678 \times 10^4 / R_o T)$
29.	$C + NO^+ \xrightarrow{k_f} CO^+ + N$		$5.96 \times 10^{12} T_e^{0.5} \exp(-3.227 \times 10^3 / R_o T)$
30.	$Ar^+ + e^- + e^- \xrightarrow{k_r} Ar + e^-$		$2.2 \times 10^{40} T_e^{-4.5}$

Table 1A  
CHEMICAL KINETICS MODEL USED IN CALCULATIONS

NO.	REACTION	THIRD BODY, M	RATE COEFFICIENT IN DIRECTION SHOWN IN cm <sup>3</sup> /mole sec OR cm <sup>6</sup> /mole <sup>2</sup> sec
1.	$O_2 + M \xrightarrow{k_f} 2O + M$	O	$2.1 \times 10^{18} T^{-0.5} \exp(-1.1796 \times 10^5 / R_o T)$
2.	$O_2 + M \xrightarrow{k_f} 2O + M$	Ar, C, CO, CO <sub>2</sub> , N <sub>2</sub> , N	$1.2 \times 10^{21} T^{-1.5} \exp(-1.1796 \times 10^5 / R_o T)$
3.	$CO + M \xrightarrow{k_f} C + O + M$	N <sub>2</sub> , N, Ar, C, O, O <sub>2</sub> , CO, CO <sub>2</sub>	$4.48 \times 10^{19} T^{-1.0} \exp(-2.56 \times 10^5 / R_o T)$
4.	$CO_2 + M \xrightarrow{k_f} O + CO + M$	N <sub>2</sub> , N, Ar, C, O, O <sub>2</sub> , CO, CO <sub>2</sub>	$8.81 \times 10^{22} T^{-2.0} \exp(-1.256 \times 10^5 / R_o T)$
5.	$CO + CO \xrightarrow{k_f} C + CO_2$		$2.33 \times 10^9 T^{0.5} \exp(4.305 \times 10^5 / R_o T)$
6.	$O + CO \xrightarrow{k_f} C + O_2$		$2.73 \times 10^{11} T^{0.5} \exp(-1.381 \times 10^5 / R_o T)$
7.	$N_2 + M \xrightarrow{k_f} 2N + M$	N <sub>2</sub> , N, C, O, O <sub>2</sub> , CO, Ar, CO <sub>2</sub>	$4.06 \times 10^{19} T^{-1} \exp(-2.25 \times 10^5 / R_o T)$
8.	$NO + M \xrightarrow{k_f} N + O + M$	N <sub>2</sub> , N, C, O, O <sub>2</sub> , Ar, CO <sub>2</sub> , CO	$4.1 \times 10^{18} T^{-1} \exp(-1.496 \times 10^5 / R_o T)$
9.	$CO + N \xrightarrow{k_f} NO + C$		$2.86 \times 10^{11} T^{0.5} \exp(-1.065 \times 10^5 / R_o T)$
10.	$N_2 + O \xrightarrow{k_f} NO + N$		$7.35 \times 10^{11} T^{0.5} \exp(-7.535 \times 10^4 / R_o T)$
11.	$NO + CO \xrightarrow{k_f} CO_2 + N$		$4.59 \times 10^8 T^{0.5} \exp(-2.397 \times 10^4 / R_o T)$
12.	$NO + O \xrightarrow{k_f} O_2 + N$		$2.98 \times 10^{11} T^{0.5} \exp(-3.865 \times 10^4 / R_o T)$
13.	$CO_2 + O \xrightarrow{k_f} O_2 + CO$		$2.55 \times 10^9 T^{0.5} \exp(-7.606 \times 10^3 / R_o T)$
14.	$CO + CO^+ \xrightarrow{k_f} CO_2 + C^+$		$1.07 \times 10^{12} T^{0.5} \exp(-6.705 \times 10^4 / R_o T)$
15.	$CO + C^+ \xrightarrow{k_f} C + CO^+$		$6.03 \times 10^{11} T^{0.5} \exp(6.336 \times 10^4 / R_o T)$

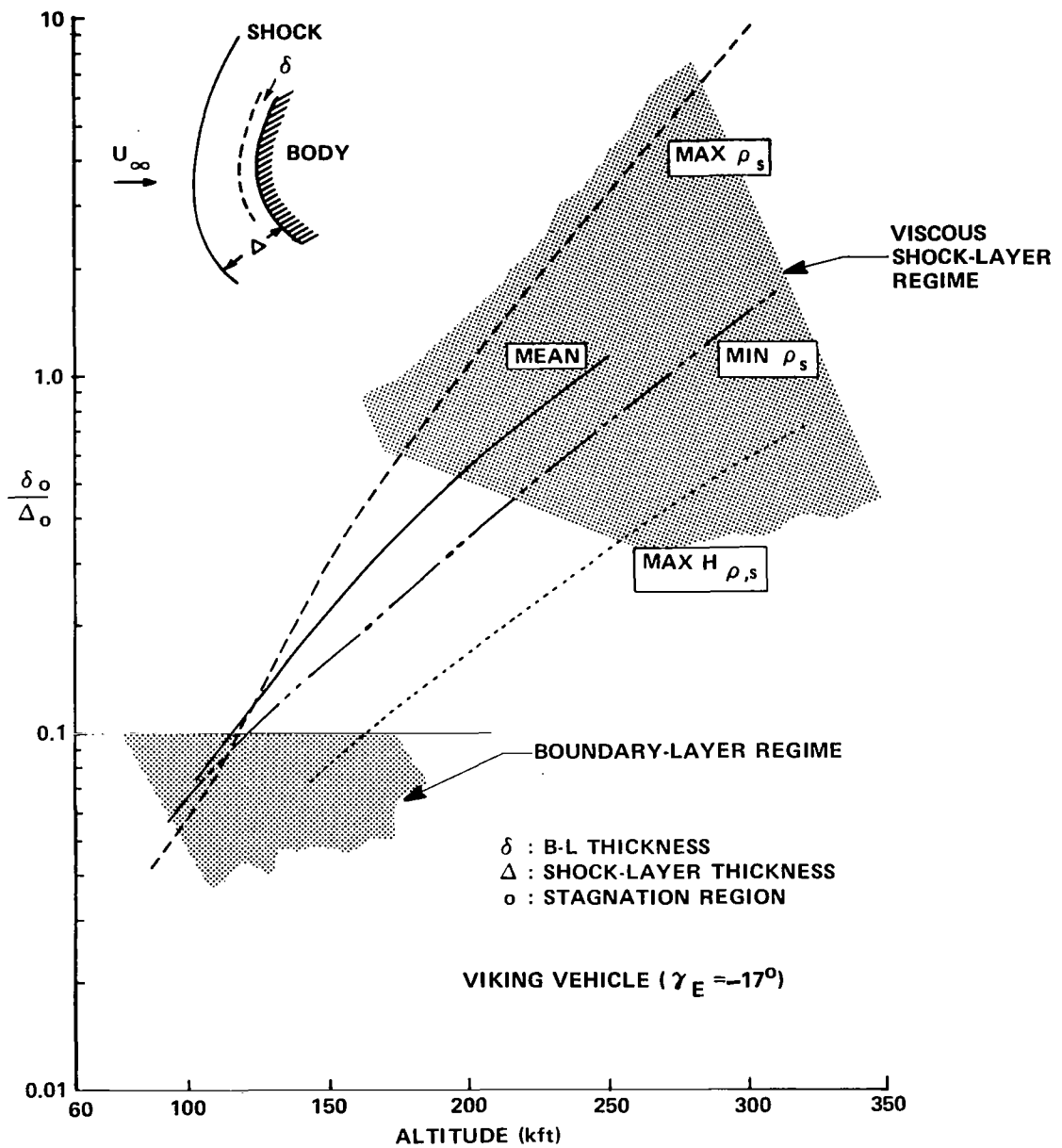


Figure 1 RATIO OF THE BOUNDARY-LAYER THICKNESS TO THE SHOCK-LAYER THICKNESS FOR VARIOUS MARS ATMOSPHERE MODELS

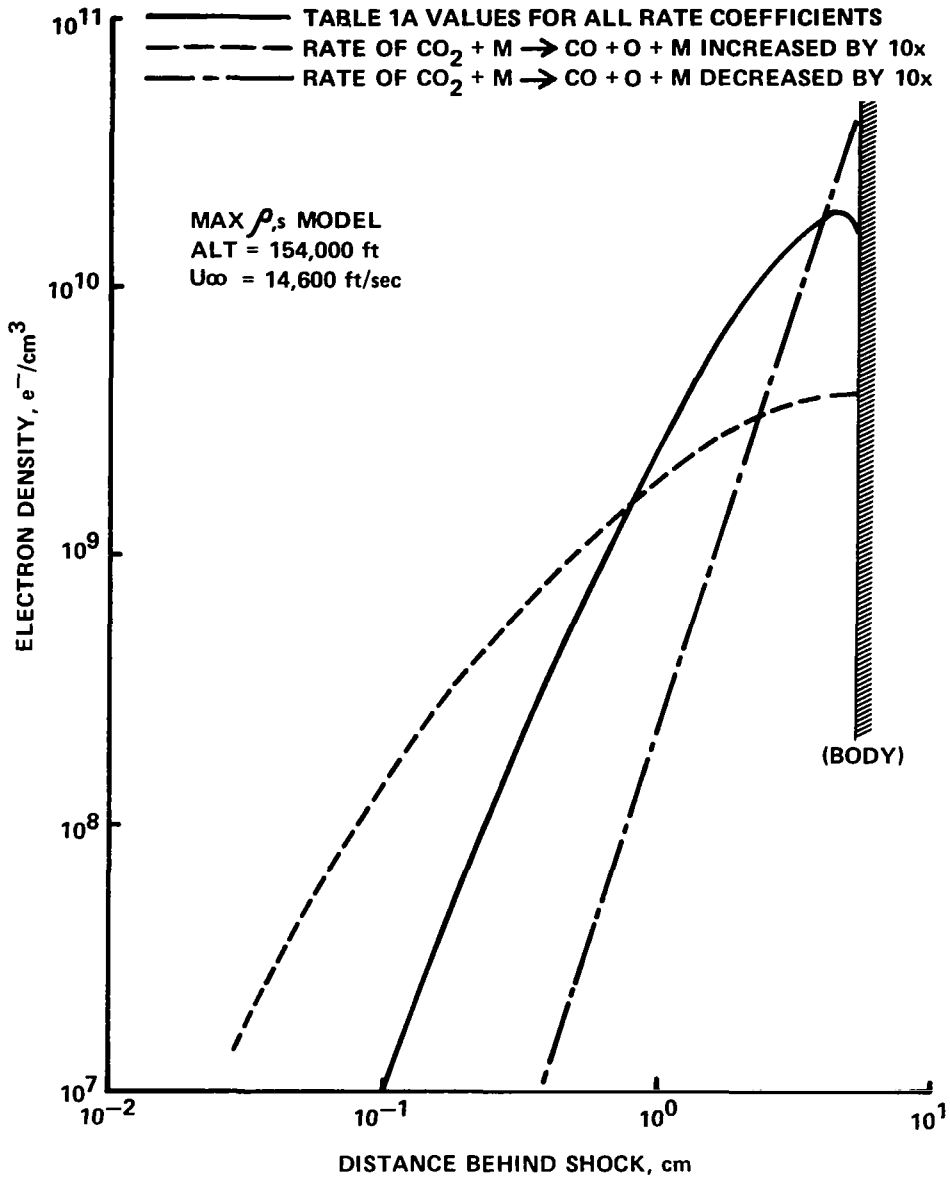


Figure 2 INFLUENCE OF RATE COEFFICIENT ON NUMBER DENSITY PROFILE

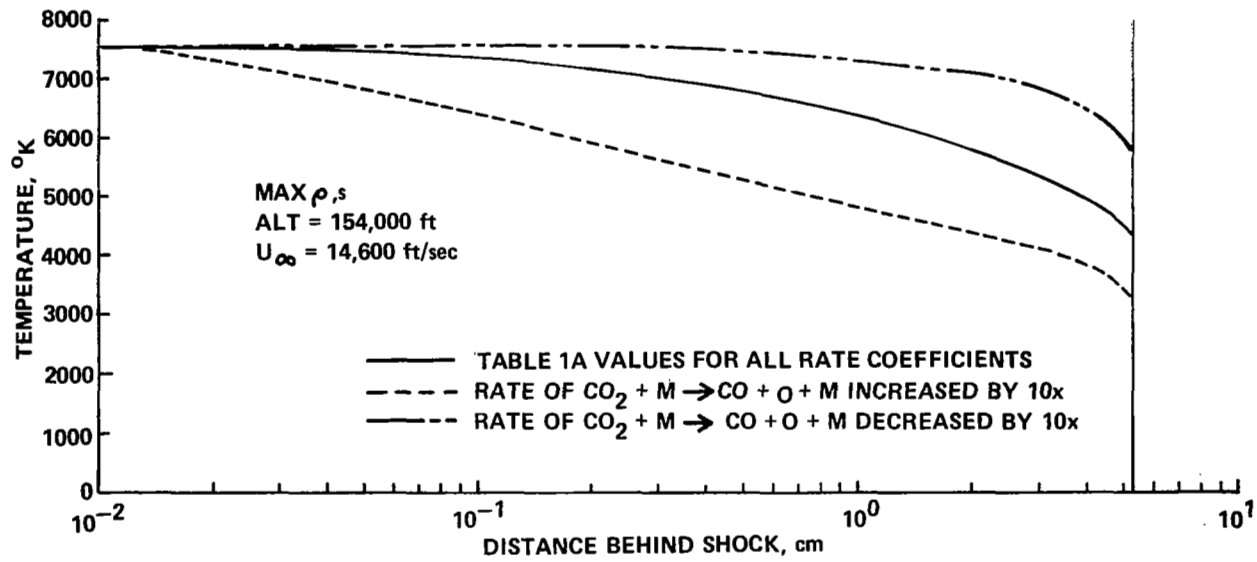


Figure 3 INFLUENCE OF RATE COEFFICIENT ON TEMPERATURE PROFILE

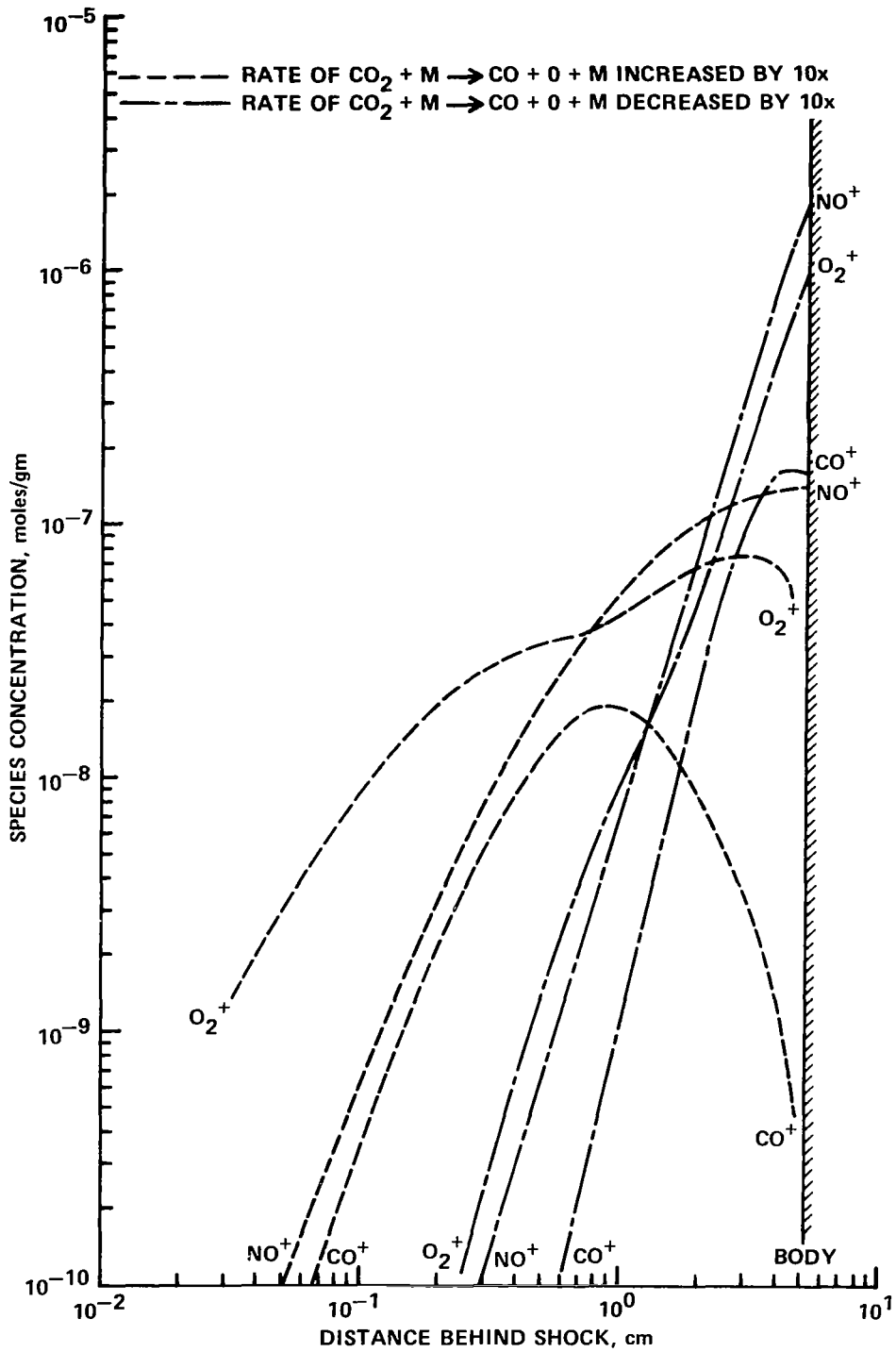


Figure 3(a) INFLUENCE OF RATE COEFFICIENT ON SPECIES PROFILES

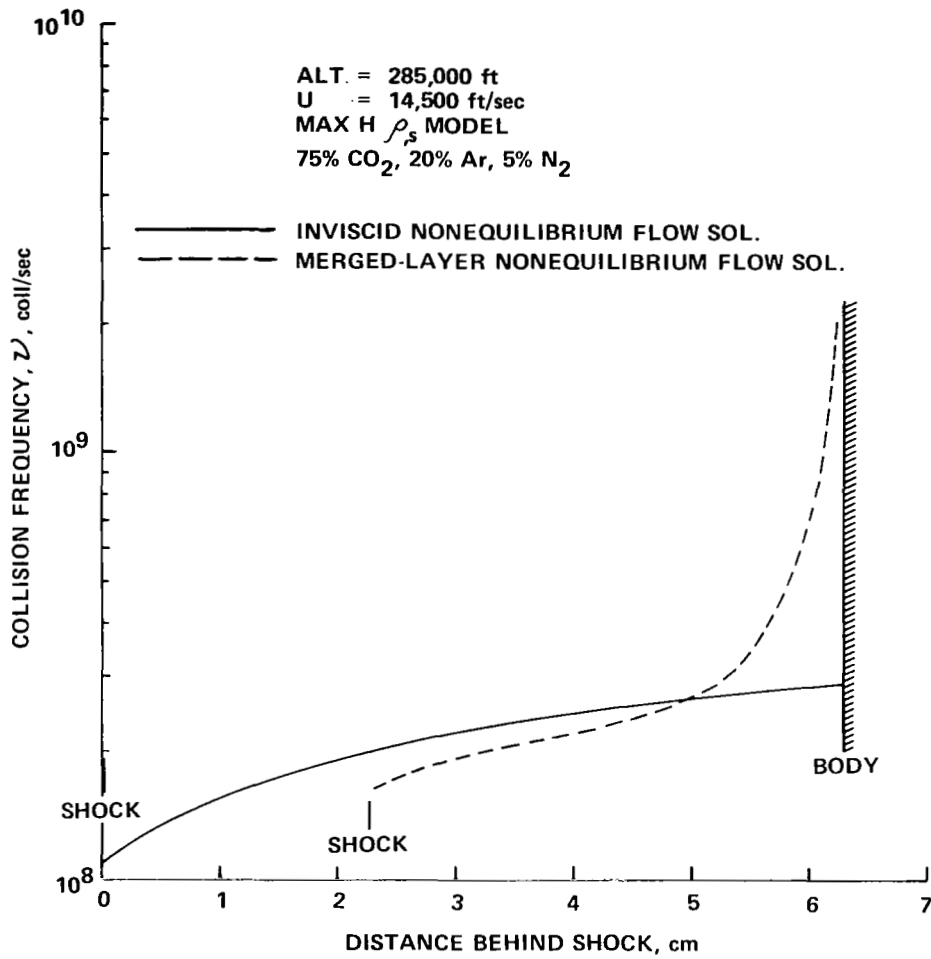


Figure 4 COLLISION FREQUENCY IN STAGNATION REGION PLASMA

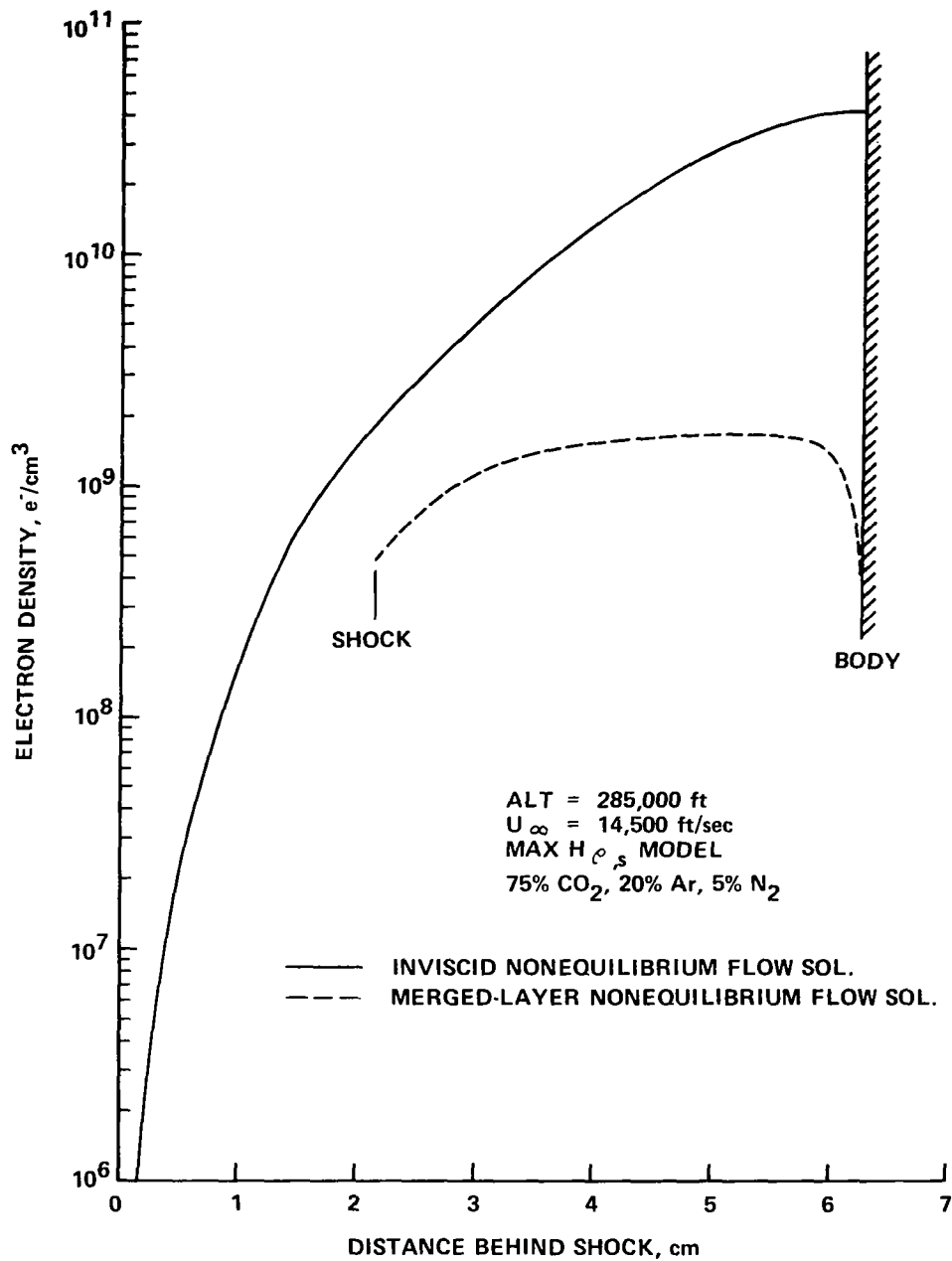


Figure 5 ELECTRON DENSITY IN STAGNATION REGION PLASMA

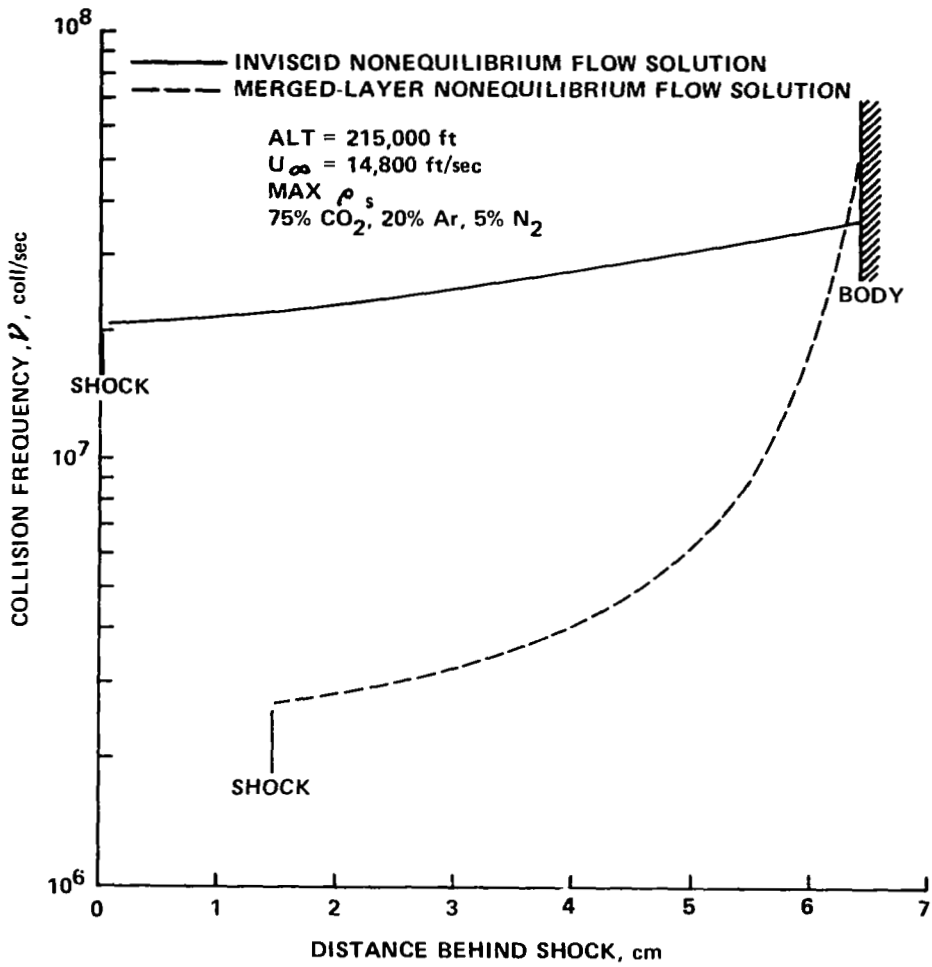


Figure 6 COLLISION FREQUENCY IN STAGNATION REGION PLASMA

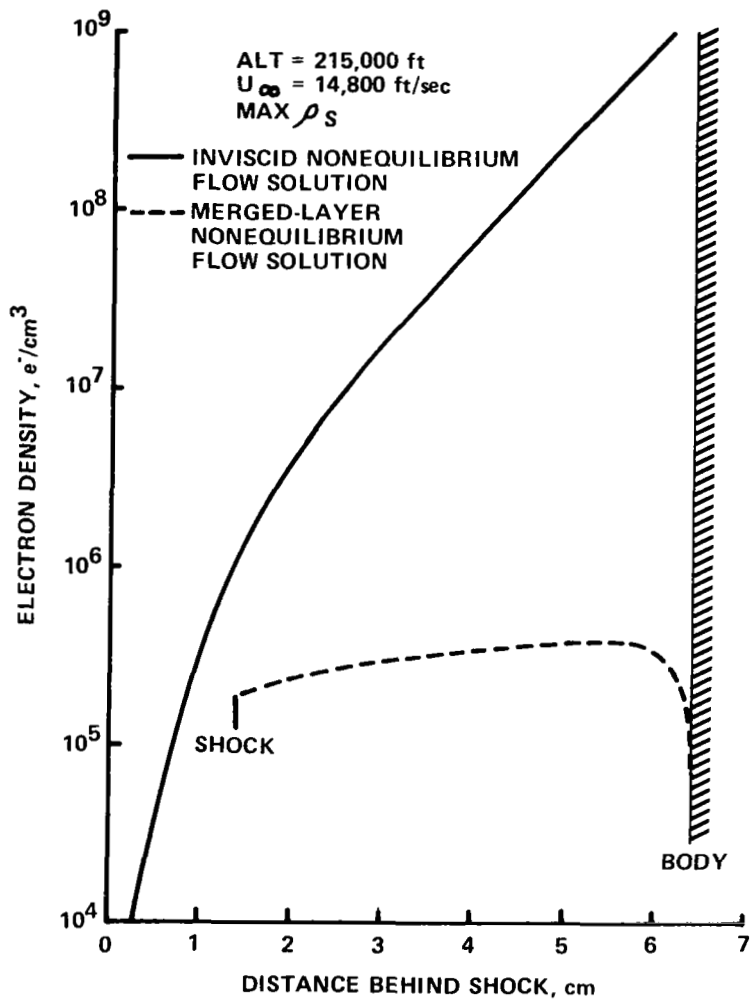


Figure 7 ELECTRON DENSITY IN STAGNATION REGION PLASMA

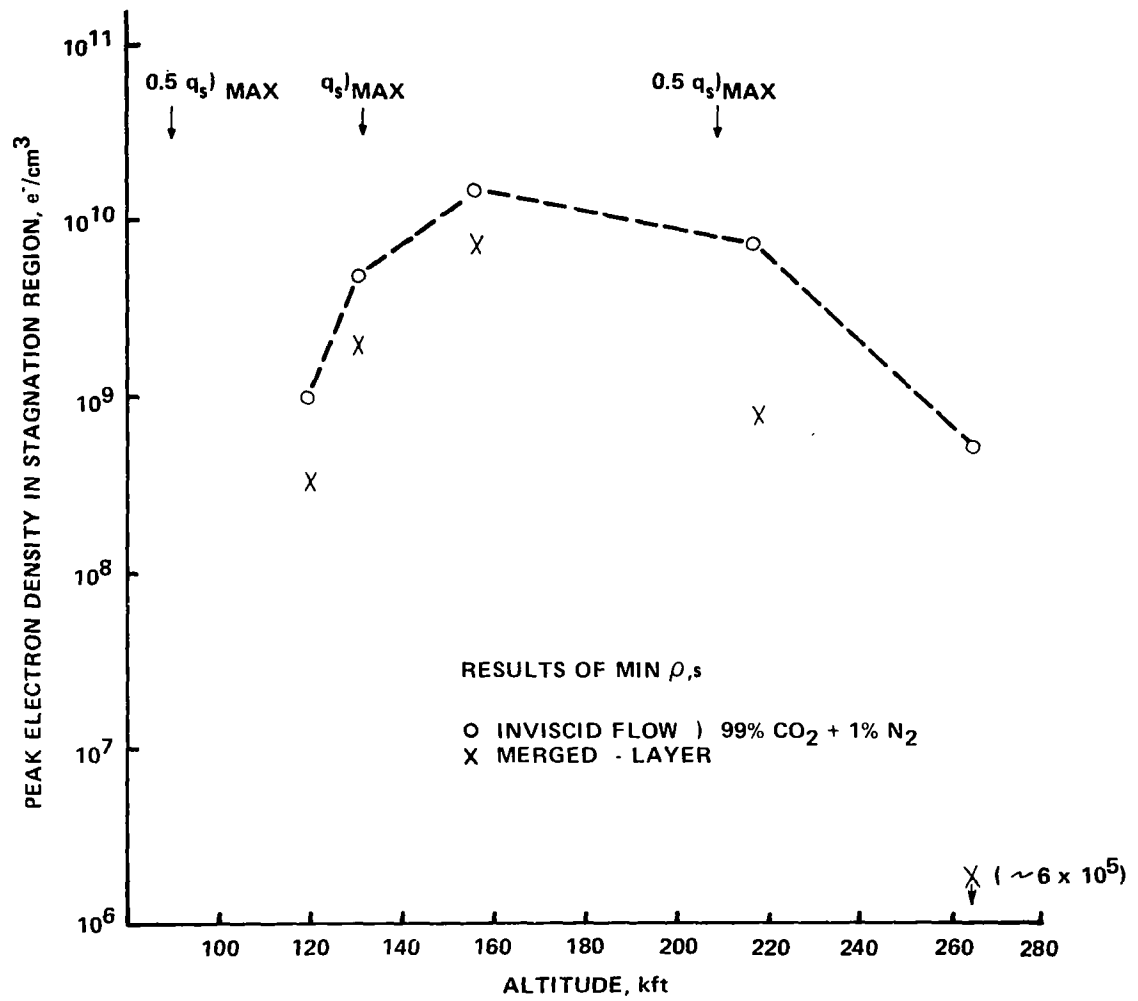


Figure 8 CALCULATED ELECTRON DENSITIES IN STAGNATION REGION PLASMA

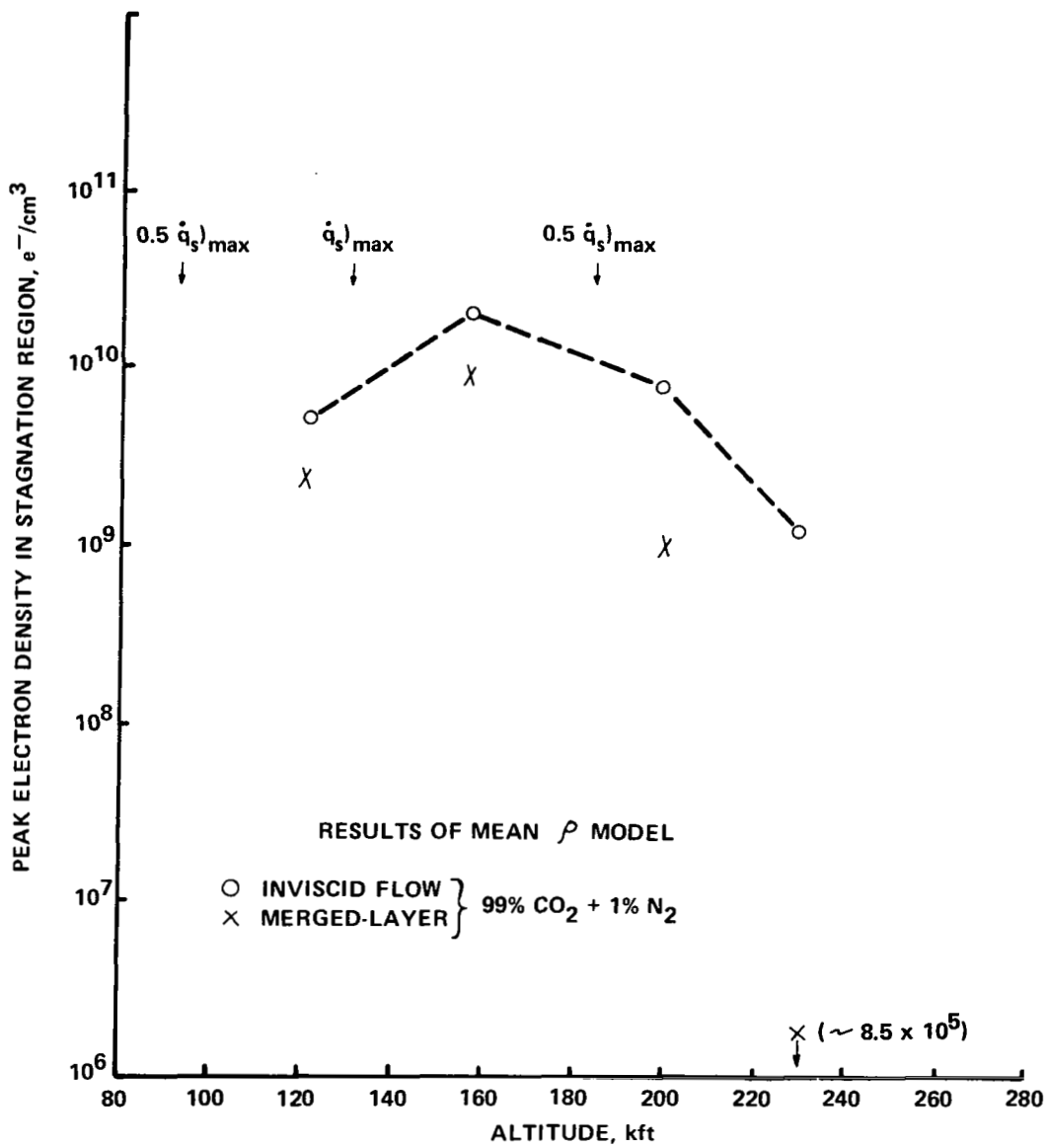


Figure 9 CALCULATED ELECTRON DENSITIES IN STAGNATION REGION PLASMA

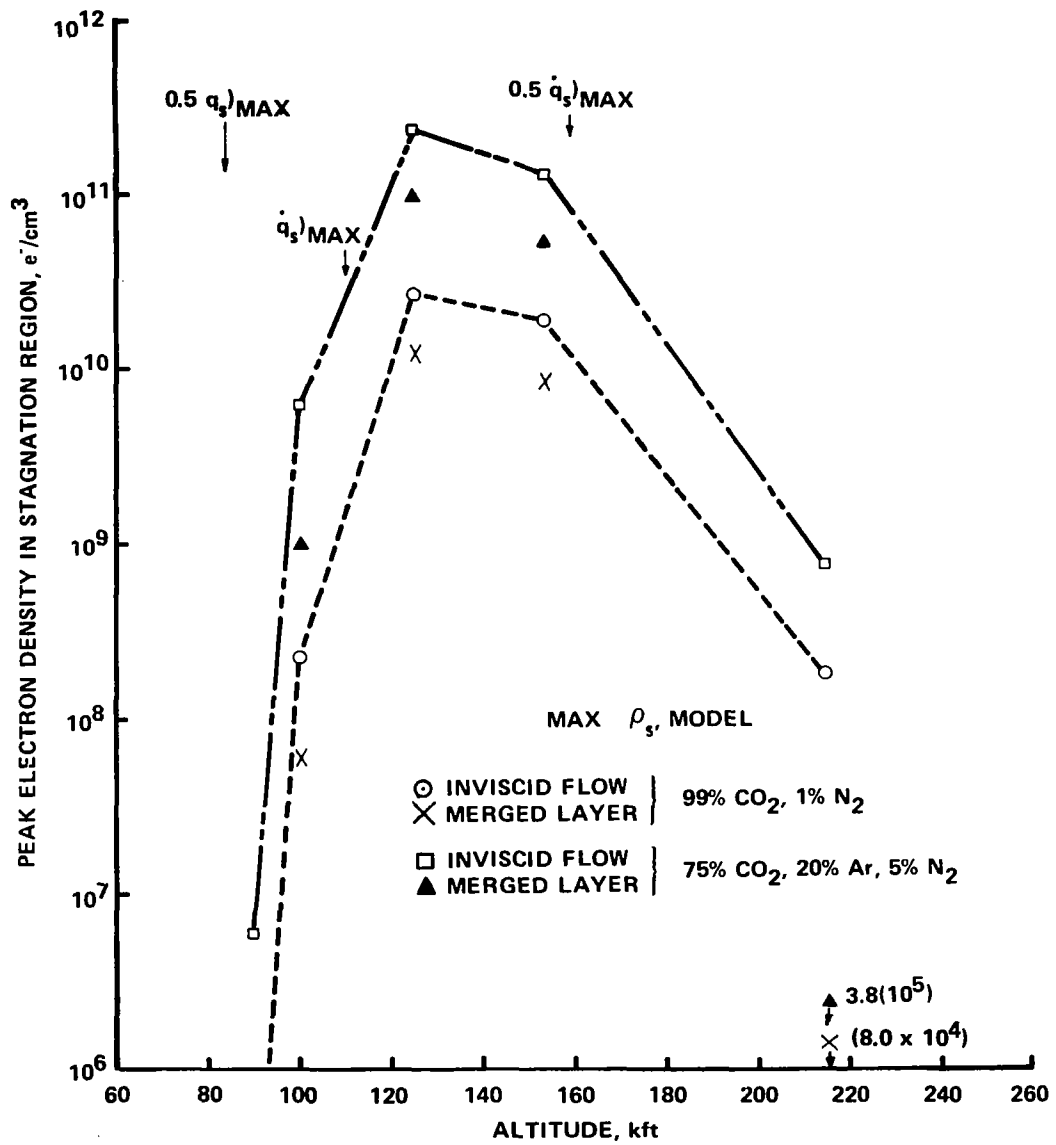


Figure 10 CALCULATED ELECTRON DENSITIES IN STAGNATION REGION PLASMA

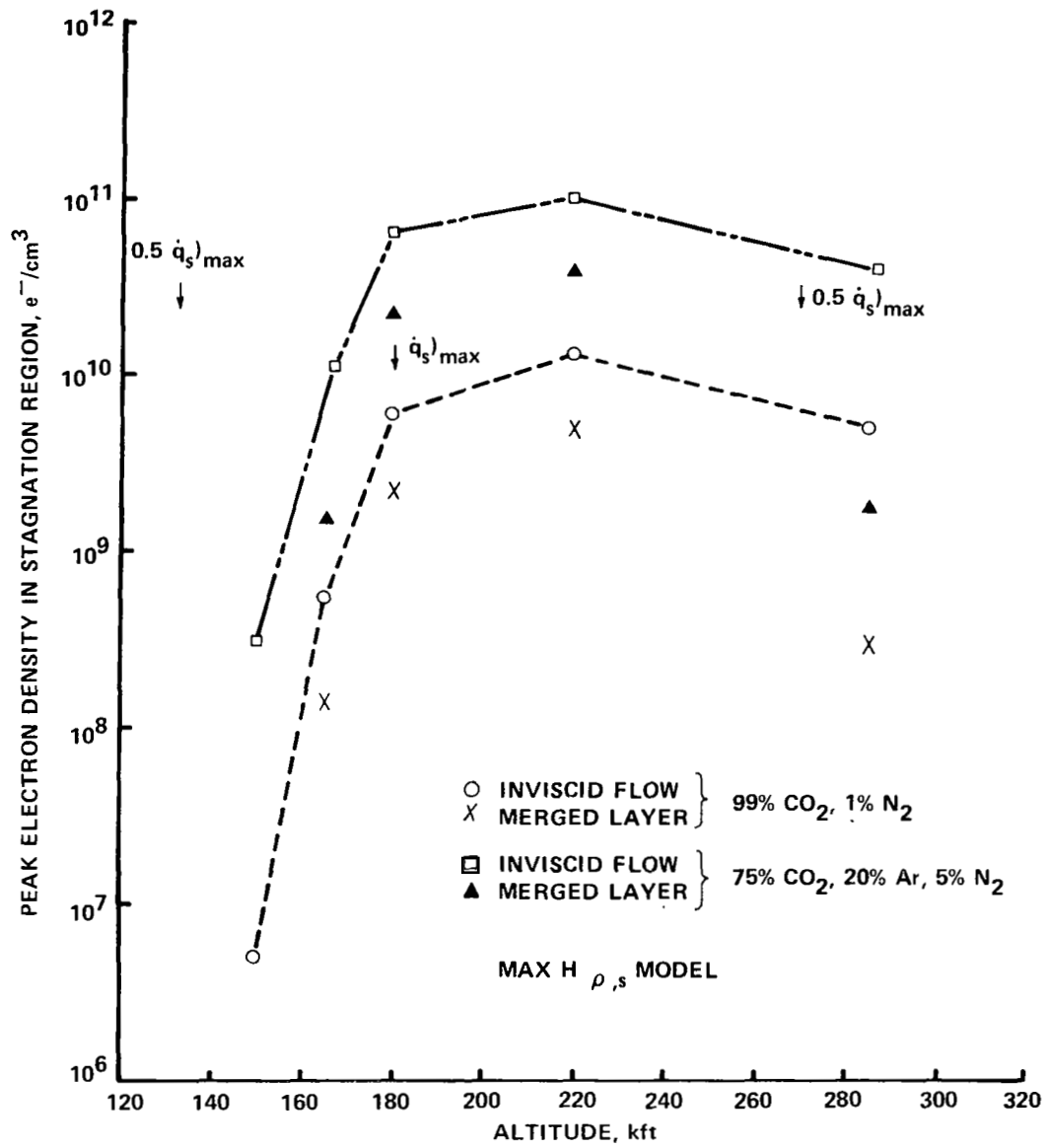


Figure 11 CALCULATED ELECTRON DENSITIES IN STAGNATION REGION PLASMA

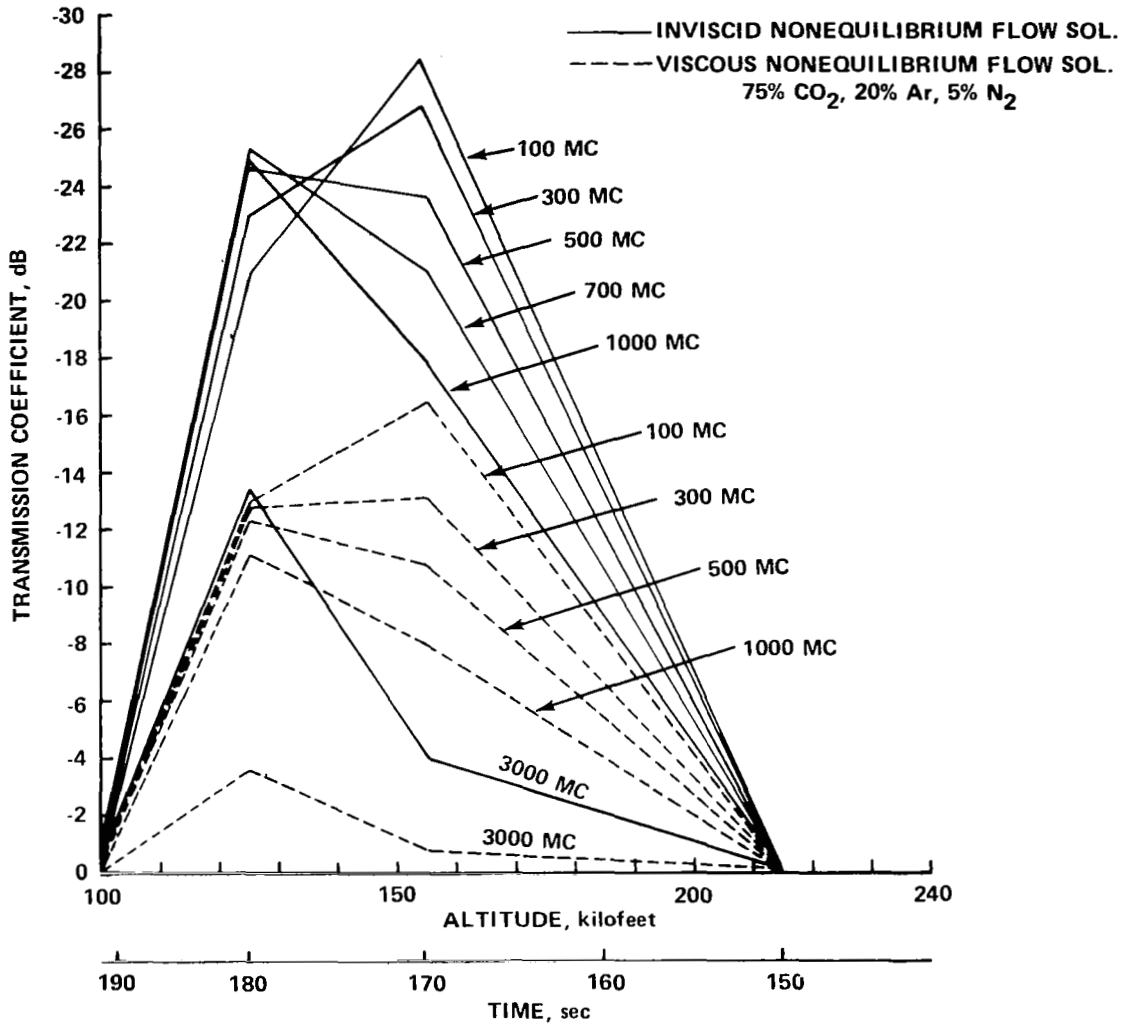


Figure 12 PLANE-WAVE TRANSMISSION COEFFICIENT VS. ALTITUDE FOR MAX  $\rho$ , S, -17°

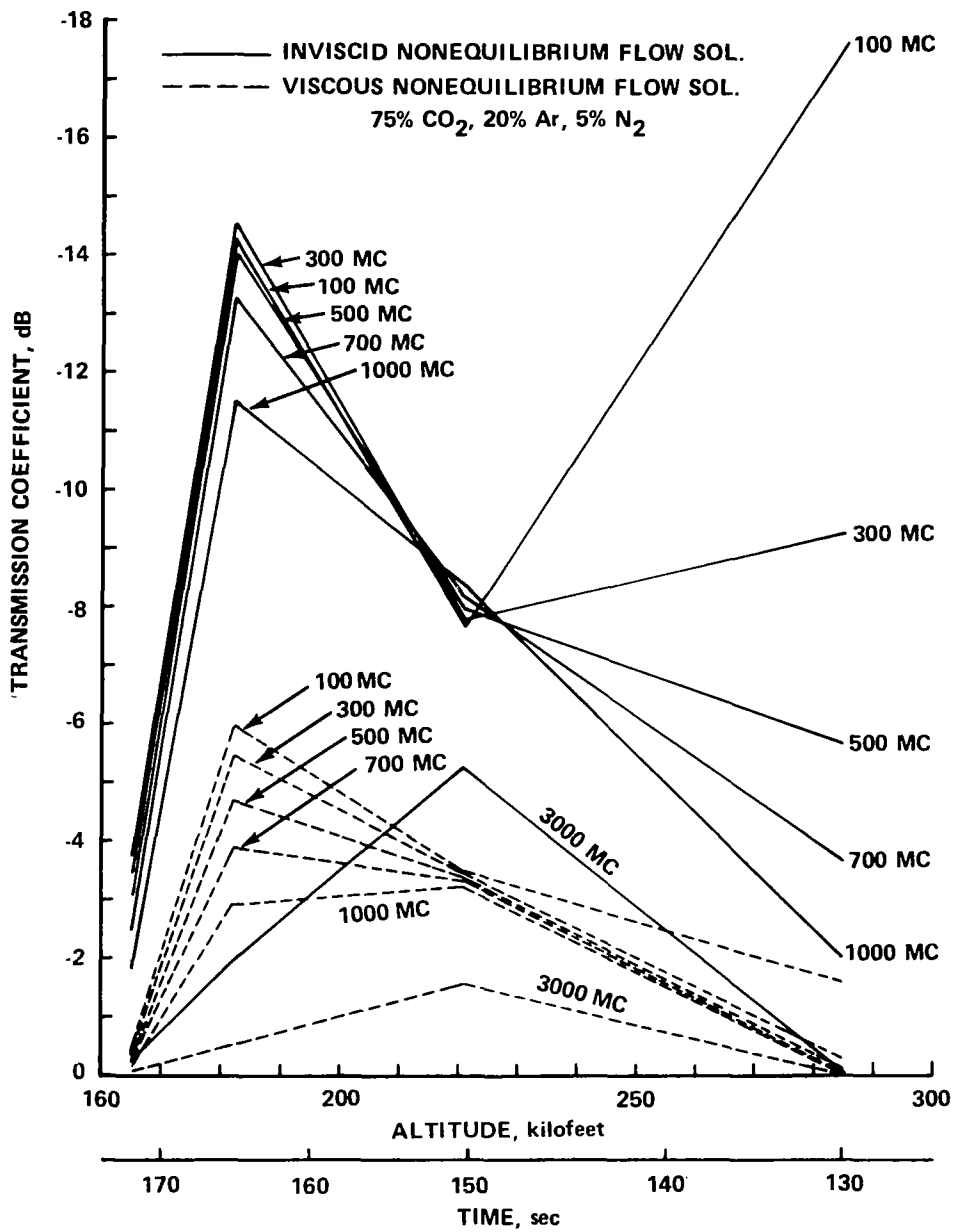


Figure 13 PLANE-WAVE TRANSMISSION COEFFICIENT VS. ALTITUDE FOR MAX  $H_p$ ,  $S_r = 17^\circ$

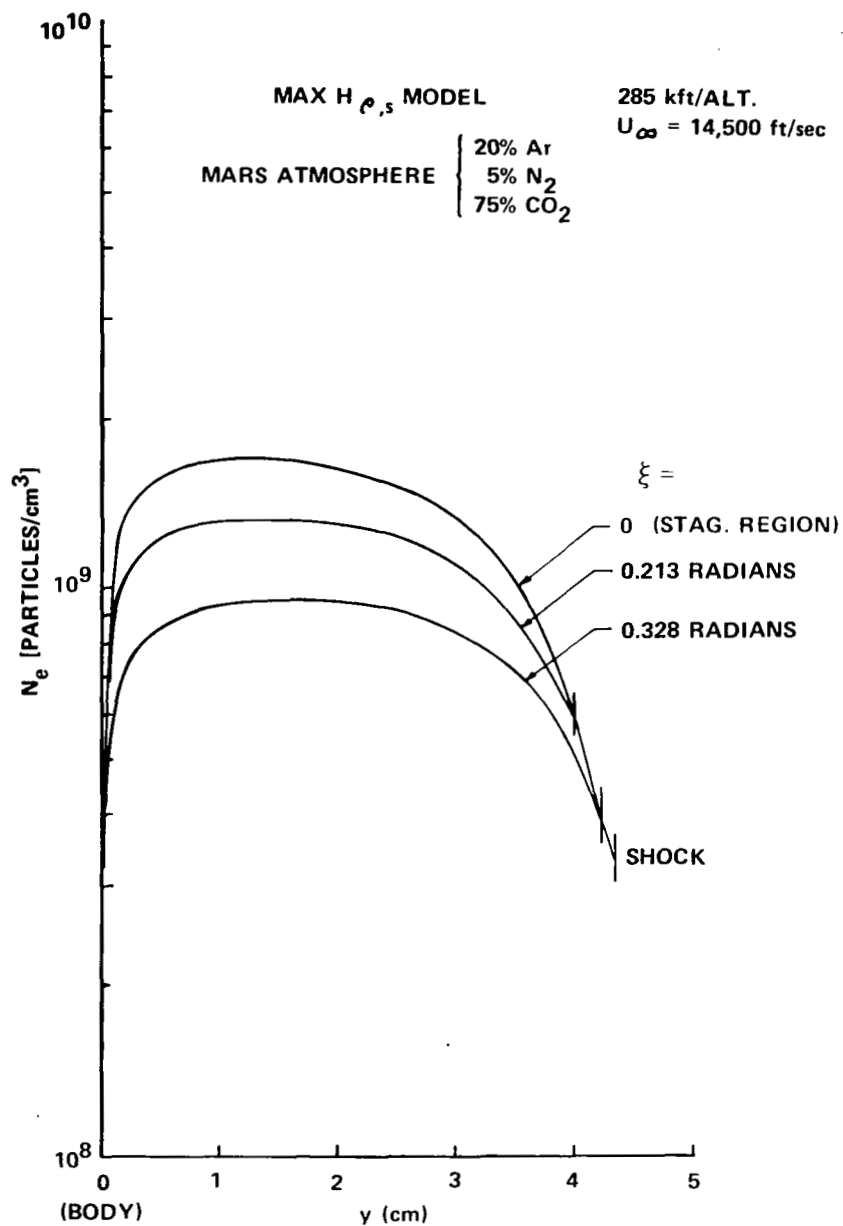


Figure 14 DISTRIBUTIONS OF ELECTRON-NUMBER DENSITY PROFILES  
 IN THE DOWNSTREAM REGION

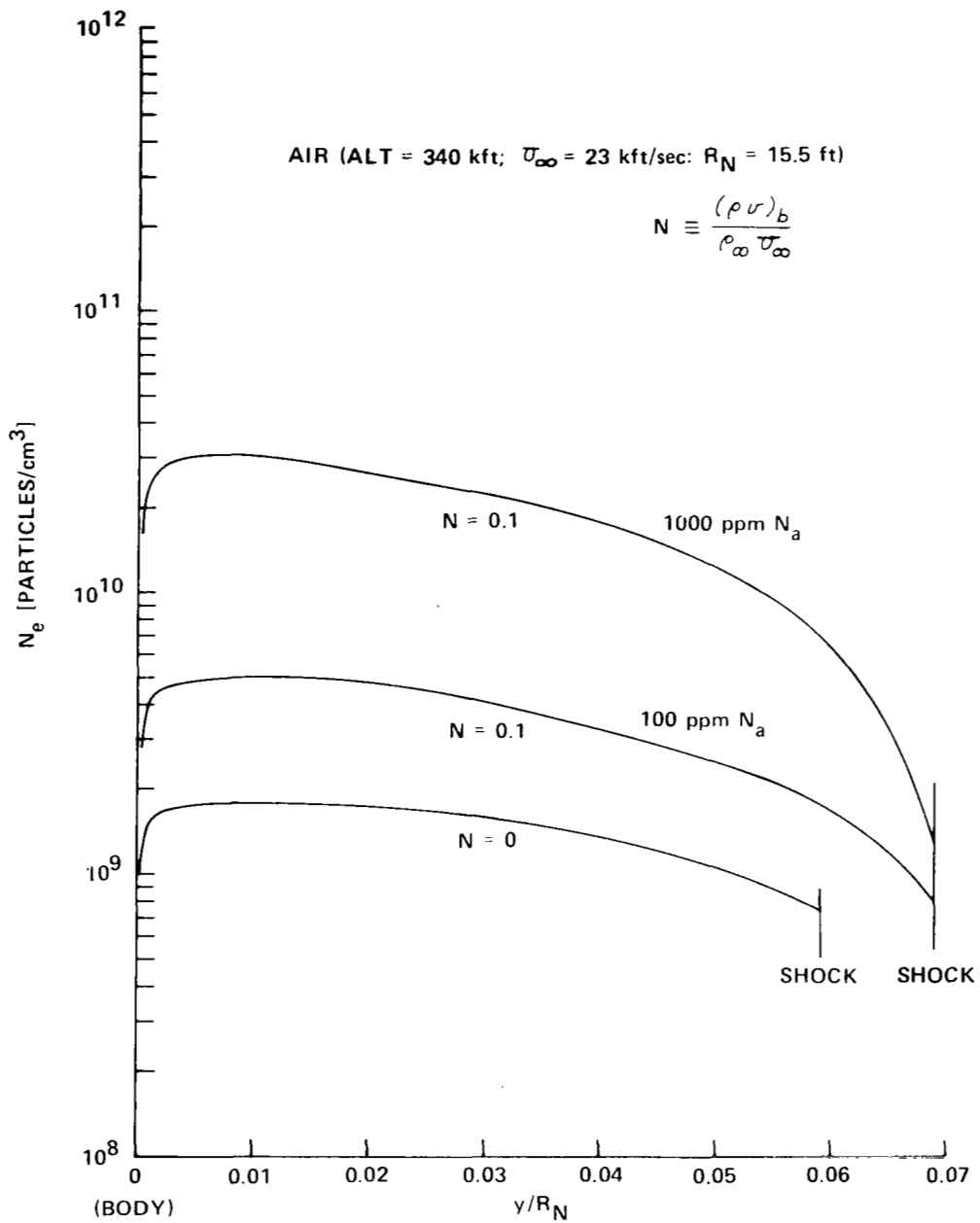


Figure 15 EFFECT OF NONEQUILIBRIUM SODIUM IONIZATION IN THE STAGNATION MERGED-LAYER REGION OF A BLUNT BODY (AIR)